

Decoding Ligand Recognition at GPR55 Using *in Silico* Predictions and Functional Assays

Thesis submitted to the University of Nottingham for the degree of Master of Research
September 2025

Cleopatra Zanele Vunganai
20135580

Supervisors: Prof Dmitry Veprintsev, Dr David Sykes, Dr Eline Koers

School of Life Sciences
University of Nottingham

Table of Contents

Abstract **4**

Acknowledgements **5**

Chapter One: Introduction **6**

GPCR signalling and function. 7
GPR55, the promising therapeutic target 8

Computational tools for predicting GPCR structure, dynamics, and ligand interactions. *9*

Experimental approaches for identifying ligands for GPR55. ..... *11*

Problem statement *14*

Aims and Objectives of this investigation. *14*

Chapter Two: Materials and Method **16**

***In silico* methods** **17**

Dataset preparation 17
Preparation of Receptor Structures 17
Molecular Docking 17
Calculating the interaction fingerprints 17
ML data preparation and feature engineering 18
Unsupervised clustering for binding mode analysis 18
CatBoost and SVM analysis for ligand activity prediction 19
Classification accuracy and performance matrices 19

***In vitro* Materials and Methods** **20**

Materials *20*
Molecular biology materials 20
Mammalian cell culture reagents 20
mG protein purification reagents 20
G-CASE plasmids 21
Compounds 21
Instruments and software 21
Construct design 21

Molecular biology methods *22*
Polymerase chain reactions (PCR) 22
Agarose Gel Analyses of PCR Products 23
DNA purification 23
Gibson Assembly 23
Transformation in E coli 23
Plasmid Preparation 23

Suspension Cell Culture *24*
Thawing cells 24
Cell subculturing 24
Transfection 24
Cell Cryopreservation 24

Adherent Cell Culture *24*
Thawing cells 24
Cell Subculturing 25

Transfection and generation of stable cell lines 25
Cell Cryopreservation 25
Membrane preparation *26*
Recombinant protein expression and purification of mG proteins *26*
Membrane-based mG protein recruitment assay (MeGaBRET) *27*
Whole cell-based β-arrestin and G-CASE assays. *27*
Functional assay data collection and analysis 28

Chapter Three: Results **29**

***In silico* findings** **29**

Ensemble semi-flexible molecular docking reveals key binding poses. 30
Calculating AIFs from key docking poses 30
Machine learning identification of key binding residues 31
Model performance and classification accuracy 37
Individual docking analysis shows atomic differences of ligand binding. 39

***In vitro* assay findings** **41**

The cell-based BRET β-arrestin recruitment assay *41*
Linker length does not influence β-Arrestin recruitment in GPR55-sLuc constructs. 42
BRET-Based β-arrestin assay reveals reduced potency of GPR55 ligands 42
The cell-based BRET G-CASE biosensor. *45*
Challenges in measuring GPR55 activity using G-CASE stable cells 45
G-CASE assays shows limited ligand-dependent responses in GPR55. 47
The membrane-based mG protein recruitment assay (MeGaBRET) *49*
Optimising the Na+ concentration in the assay buffer 50
Optimising the BSA concentration in the assay buffer 51
Ligand potency across constructs C01, C02 and C03 53
MeGaBRET successfully quantifies ligand induced GPR55 activation 54
Exploration of G-protein coupling specificity 56

Chapter Four: Discussion **58**

Analysis of computational work. *59*
Transitioning from 'which' to 'how' ligands bind to GPR55. 59
Our predicted GPR55 ligand binding pocket 59
Key ligand interactions and binding patterns 60
Comparison with resolved GPR55 cryo-EM structures 60
Limitations of ensemble docking and SVM classification accuracy 60
Analysis of experimental work. *61*
Analysis of the β-Arrestin Recruitment Assay 61
Limitations of the β-Arrestin Recruitment Assay 62
Unsuccessful implementation of the G-CASE biosensor for GPR55. 62
Advantages of MeGaBET over conventional cell-based assays. 63
Limitations of MeGaBRET. 63
Conclusions and future directions *64*

References **65**

Abstract

GPR55 is a non-canonical cannabinoid receptor that has emerged as a promising therapeutic target for cancer, inflammation, and metabolic disorders. Despite its therapeutic potential, the pharmacology of GPR55 remains poorly defined due to a limited understanding of the structural mechanisms underlying receptor function, inconsistent ligand activity across cellular assays, a lack of potent ligands, and the absence of standardised screening methods. To address these challenges, this study combines computational and experimental approaches to elucidate the molecular basis of GPR55 ligand recognition and develop a sensitive, robust assay for ligand screening.

Computationally, we applied molecular docking, interatomic fingerprinting, and machine learning analysis to a curated dataset of 563 GPR55 ligands across five receptor structures. CatBoost classifiers and SHAP analysis were also used to identify recurring interactions and visualise the data in a way that distinguishes agonists from antagonists. Experimentally, we replicated the established cell-based β-arrestin recruitment and G-GASE biosensor assays in stable HEK293TR cell lines. To overcome the limitations of cell-based assay, we developed a BRET membrane-based mG protein recruitment assay (MeGaBRET) to provide a more direct and controllable readout of GPR55 activation.

The computational analysis of ~5600 ligand binding poses identified the eleven residues $W177^{ECL2}$, $P155^{4.59x60}$, $M167^{ECL2}$, $Q271^{7.36x35}$, $F102^{3.33x33}$, $V149^{4.53x53}$, $M274^{7.39x38}$, $F246^{6.55x55}$, $M172^{ECL2}$, $L270^{7.35x34}$, and $I156^{4.60x61}$ as key determinants of ligand pharmacology at GPR55. The CatBoost prediction model showed moderate performance, with positive MCC values between 0.25 and 0.39, demonstrating that our model was able to capture meaningful trends in agonist and antagonist classification. Experimentally, the β-arrestin recruitment assay reproduced literature trends but with ~2-fold lower potency than the reported data. THC showed no β-arrestin recruitment despite literature reports of GPR55 agonism. Unfortunately, multiple attempts to set up the G-CASE biosensor assays failed due to poor signal-to-noise ratios and overlapping concentration-response curves. In contrast, the optimised MeGaBRET assay produced response windows ~3 times larger than β-arrestin assays and successfully revealed the G protein bias of THC and the endogenous ligand LPI. MeGaBRET also detected mGi protein coupling for the potent ligands ML184 and compound 26, with EC_{50} values of 243 nM and 65 nM, respectively. Further optimisation is still required to measure mG_{12} and mG_q coupling using MeGaBRET.

This study demonstrates that combining computational modelling with advanced functional assays provides a more comprehensive understanding of GPR55 pharmacology. Key receptor residues influencing ligand activity were identified, and the MeGaBRET assay was successfully developed for GPR55 ligand screening. This novel, robust assay expands the toolkit for ligand screening and provides a more controlled and sensitive approach to characterising ligand activity, helping to address the inconsistencies observed in conventional GPR55 assays. Together, these approaches offer a validated framework for rational drug design and orphan GPCR characterisation that can be applied beyond GPR55.

Acknowledgements

I would like to express my sincere gratitude to my supervisors, Professor Dmitry Veprintsev, Dr David Sykes, and Dr Eline Koers, for their guidance, encouragement, and support throughout this project. I am also especially thankful to Armin Nikpour Khoshgrundi for his supervision and for personally teaching me how to set up and run most of the assays that formed the foundation of this work. I would also like to acknowledge the past and present members of the Veprintsev lab, everyone in Compare and the Z7 Biotech team for their advice, and support. My sincere thanks also go to our GPR55 collaboration group, this project would not have been possible without the shared knowledge and access to novel GPR55 ligands. On a personal note, I am deeply grateful to my mum, my sisters, and my friends, whose love and support sustained me throughout this journey. Finally, I thank the Lord Almighty for giving me the strength and perseverance to complete this work.

Chapter One: Introduction

GPCR signalling and function.

G protein-coupled receptors (GPCRs) are the largest and most versatile family of cell-surface receptors, with over 800 members encoded in the human genome (Bjarnadóttir *et al.*, 2006). They share a conserved structural architecture of seven transmembrane helices, connected by extracellular and intracellular loops, with an extracellular N-terminus and intracellular C-terminus. Based on sequence homology and functional similarities, GPCRs are divided into Class A, rhodopsin-like GPCRs; Class B, secretin-like GPCRs; Class C, glutamate-like GPCRs; Class D, fungal pheromone GPCRs; Class E, cyclic adenosine monophosphate (cAMP)-like GPCRs; and Class F, frizzled GPCRs (Fredriksson *et al.*, 2003). This diversity enables GPCRs to mediate responses to a wide range of stimuli, like photons, ions, lipids, hormones, peptides and odorants (Hu, Mai and Chen, 2017).

The defining feature of GPCRs is their ability to couple with heterotrimeric guanine-nucleotide binding proteins (G proteins), which are composed of an alpha (Gα), beta (Gβ), and gamma (Gγ) subunit (Kamato *et al.*, 2015). The Gαβγ heterotrimers are primarily localised in their resting state on the inner leaflet of the cellular plasma membrane, with the Gα subunit bound to guanine diphosphate (GDP) and associated with Gβγ subunits. Upon agonist binding, GPCRs undergo a conformational change that induces the exchange of the GDP bound on the Gα subunit with guanine triphosphate (GTP). This leads to the dissociation of the Gα subunit from the Gβγ dimer, resulting in two functional subunits (Gα and Gβγ) that both interact with various downstream effectors to regulate a range of intracellular pathways (Bondar and Lazar, 2020). Four major Gα subunit subfamilies mediate downstream signalling, namely $G\alpha_s$, which stimulates adenylyl cyclase and elevates intracellular cyclic AMP (cAMP) (Tesmer *et al.*, 1997); $G\alpha_{i/o}$, which inhibits adenylyl cyclase and lowers cAMP levels (Dessauer, Chen-Goodspeed and Chen, 2002); $G\alpha_{q/11}$, which activates phospholipase C and controls the activity of calcium ($Ca^{2+)}$ channels (Aragay, Katz and Simon, 1992); and $G\alpha_{12/13}$, which activate Rho GTPases to regulate cell migration and proliferation (Hilger, Masureel and Kobilka, 2018). Further, the Gβγ subunit dimers can also propagate downstream signalling by directly interacting with effector proteins. These interactions can include modulation of potassium channels, phospholipase Cβ (Zhang *et al.*, 1996), specific adenylyl cyclase isoforms (Taussig *et al.*, 1994), and voltage-gated calcium channels (Zamponi *et al.*, 1997).

GPCR signalling is tightly controlled, and they become desensitised after prolonged exposure to their ligands via β-arrestin-mediated internalisation. β-arrestins were first characterised as proteins that desensitise GPCRs by binding to GPCRs that have been phosphorylated by G protein-coupled receptor kinases (GRKs) at serine and threonine residues on the intracellular loops or C-terminus of the receptor. This binding sterically prevents further coupling of heterotrimeric G proteins, thereby terminating G protein signalling (Benovic *et al.*, 1989; Gurevich *et al.*, 2012). β-arrestins serve as adaptor proteins that recruit components of the endocytic machinery, such as clathrin and AP-2, leading to receptor internalisation and either recycling back to the membrane or targeting to lysosomes for degradation (L. Mohan *et al.*, 2012). Now, β-arrestins are recognised as also capable of initiating signalling pathways, such as the MAPK/ERK cascade (Eichel, Jullié and von Zastrow, 2016). This dual signalling of GPCRs has introduced the concept of biased signalling, whereby ligands preferentially stabilise receptor conformations that favour either G protein or β-arrestin-mediated downstream signalling (Costa-Neto, Parreiras-e-Silva and Bouvier, 2016). This complexity is

valuable when designing selective drugs, but it also makes the development of sensitive, reproducible, and high-throughput assays for ligand screening challenging.

GPR55, the promising therapeutic target

Adding on to this challenge, a significant proportion of GPCRs remain classified as "orphan" receptors, meaning their endogenous ligands and physiological roles are unknown (Libert *et al.*, 1991). Deorphanising these receptors is a major challenge in pharmacology, but also an important opportunity, as uncovering their ligands can reveal novel signalling pathways and therapeutic targets. Among the 87 class A orphan GPCRs currently listed (Alexander *et al.*, 2023), orphan GPR55 was first identified and cloned in 1999 as a novel human intron-less GPCR gene, encoding a protein of 319 amino acids mapped to chromosome 2q37 (Sawzdargo *et al.*, 1999). GPR55 has since attracted significant attention due to its ability to respond to endocannabinoid lipids (Baker *et al.*, 2006).

At first, GPR55 was proposed as a novel cannabinoid receptor, potentially accounting for cannabinoid effects not mediated by established cannabinoid receptors, CB1 and CB2, such as vasodilation (Ryberg *et al.*, 2009; Yang *et al.*, 2020). However, this classification remains controversial, as GPR55's pharmacology often shows inconsistencies and limited reproducibility across experimental systems (Henstridge *et al.*, 2010; Ross, 2009; Sharir and Abood, 2010). In parallel, the identity of its endogenous ligand was also widely debated until Oka *et al.* (2007) demonstrated that lysophosphatidylinositol (LPI) elicits ERK phosphorylation and Ca^{2+} release via GPR55, supporting the view that LPI acts as the endogenous ligand and that GPR55 functions as an intrinsic LPI receptor. Now, LPI as the endogenous ligand has been supported by many other experimental outcomes and is now the widely accepted endogenous ligand for GPR55 (Henstridge *et al.*, 2009; Okuno and Yokomizo, 2011; Oka *et al.*, 2007; Claff *et al.*, 2025).

Accumulating evidence has also shown that GPR55 possesses distinct signalling properties to CB1 and CB2 (Wang *et al.*, 2020; Biringer, 2021; Henstridge *et al.*, 2010). It couples primarily to $G\alpha_{13}$ proteins (Ryberg *et al.*, 2009), which activate the Rho kinase pathway, regulating cytoskeletal remodelling, inflammation, and cell migration (Henstridge *et al.*, 2010; Balenga *et al.*, 2011). In addition, GPR55 can also couple to $G\alpha_{12}$, which converges on Rho family GTPases and overlaps with $G\alpha_{13}$-driven responses. There is also evidence of coupling to $G\alpha_q$, leading to the activation of phospholipase C (PLC), mobilisation of intracellular Ca^{2+}, and downstream activation of kinases such as ERK1/2 and NFAT (Ross, 2009; Lauckner *et al.*, 2008). Further, the widespread expression of GPR55 in tissues such as the adrenal glands, brain, gastrointestinal tract, liver, and immune cells (Ryberg *et al.*, 2009; Moreno-Navarrete *et al.*, 2012; Guillamat-Prats *et al.*, 2022) aligns with its reported involvement in multiple physiological and pathological processes, including Parkinson's disease (Celorrio *et al.*, 2017), cancer (Ross, 2011), metabolic disorders (Liu *et al.*, 2015), inflammation (Yang, Zhou and Lehmann, 2016), and pain (Gangadharan *et al.*, 2013).

More specifically, in relation to disease, $G\alpha_{12/13}$ protein downstream activity has been directly implicated in cancer progression (Rasheed *et al.*, 2021). Elevated GPR55 expression has been reported in colorectal cancer, where it promotes cell adhesion, migration, and metastasis (Kargl *et al.*, 2015; Hasenoehrl *et al.*, 2017). In pancreatic cancers, mouse models have shown that GPR55 inhibition reduces tumour growth and enhances the efficacy of chemotherapy drugs (Ferro *et al.*, 2018). In triple-negative breast cancer, activation of GPR55

with endogenous ligand LPI was shown to switch on signalling via $G\alpha_{q/11}$ and ERK pathways, which in turn drove metastatic behaviour of the cancer cells (Andradas *et al.*, 2016). Similar pro-malignancy roles for GPR55 have been described in skin, prostate, and ovarian cancers (Pérez-Gómez *et al.*, 2013). So, multiple studies have also shown that the genetic deletion or pharmacological inhibition of GPR55 suppresses tumour growth and improves survival outcomes, thereby highlighting GPR55 as a promising therapeutic target.

Computational tools for predicting GPCR structure, dynamics, and ligand interactions.

Despite its therapeutic potential, progress in understanding GPR55 pharmacology has been hindered by the lack of potent and selective ligands. Additionally, like many GPCRs, GPR55 did not have a resolved cryo-EM structure. It was not until late 2024 that the cryo-EM structure of GPR55, with both active and inactive conformations, was determined (Chang *et al.*, 2024; Xia *et al.*, 2024; Claff *et al.*, 2025). Receptor structures are crucial for drug discovery as they enable researchers to visualise how ligands bind to the receptor's active site and assist in designing more effective and selective drugs. Without structural knowledge, predicting how the receptor will interact with ligands is difficult, which may be causing conflicting experimental results across systems and complicating efforts to study GPR55's signalling pathways and identify new therapeutic compounds.

The challenges posed by limited structural information are not unique to GPR55 but apply broadly across the GPCR superfamily. GPCRs represent the largest family of druggable targets in the human genome, with roughly one-third of all FDA-approved drugs acting on GPCRs (Hauser *et al.*, 2017). Due to this central role in pharmacology, computational methods have become increasingly integrated into their drug discovery pipeline. These approaches have evolved from simple screening tools to sophisticated platforms for rational drug design (Sliwoski *et al.*, 2013). In recent years, structure-based drug design (SBDD) has expanded drastically, enabled by breakthroughs in cryo-EM, improved modelling tools, and AI-assisted prediction (Zhang *et al.*, 2024; Chen *et al.*, 2024; Cebi *et al.*, 2024).

Before many resolved receptor structures were available, homology modelling (Costanzi, 2011) was the primary approach for predicting the three-dimensional structure of GPCRs. This method uses known structures of related receptors as templates to infer the arrangement of amino acids and secondary structural elements of the target receptor. While these homology models made by software like Rosetta™ (Simons *et al.*, 1999; Song *et al.*, 2013) provided useful frameworks for identifying potential binders and studying receptor signalling, their accuracy was limited by the lack of high-resolution templates. Thereby providing very little additional information compared to their template structures unless they were subjected to further refinement (Bhattacharya *et al.*, 2013). Some of the more successful methods of refinement involved using molecular dynamics (MD) simulations (Fan and Mark, 2004), which permit the exploration of how atoms in a protein move over time, using physics rules to predict their interactions. Also, such simulations can predict how proteins will respond, at an atomic level, to phosphorylation, protonation, mutations or the addition or removal of a ligand.

More recently, AI-based structure prediction methods such as RoseTTAFold (Baek *et al.*, 2021) and AlphaFold (Jumper *et al.*, 2021), have enabled highly accurate prediction of GPCR structures even in the absence of homologous templates. Also, work is ongoing to assess how

well AlphaFold, and successors can capture the conformational states of GPCRs (Heo and Feig, 2022; He *et al.*, 2023). In parallel, advances in geometric deep learning generative modelling have enabled integration of structural information into ligand design, docking pose prediction, and de novo ligand generation (Isert, Atz and Schneider, 2023; Drotár *et al.*, 2021).

While these developments have advanced the structural toolkit available for GPCR research, translating structural data into functional and pharmacological insight remains challenging. In structure-based drug design, a key question is not only where the ligand binds but also which receptor-ligand interactions determine whether a compound acts as an agonist or antagonist.

To address this, the present study combines molecular docking with machine learning to investigate which ligand-receptor interactions mediate agonism or antagonism. Specifically, molecular docking is used to provide predicted ligand poses within the receptor binding site (***Figure 1A***), while interatomic fingerprinting methods are used to describe the resulting receptor- ligand contacts (***Figure 1B***). These structured interaction patterns form the basis of machine learning analysis, where algorithms such as CatBoost and support vector machines (SVM) are applied to distinguish agonists from antagonists. Model performance is evaluated using balanced classification metrics that account for both correct and incorrect predictions, ensuring reliability within the imbalanced dataset. To interpret the models, we use SHapley Additive exPlanations (SHAP)**,** an explainable AI framework based on cooperative game theory that assigns a contribution value to each feature for a given prediction. By applying SHAP, we can quantify which receptor-ligand interactions most strongly influence the model's classification of agonists and antagonists, linking computational predictions directly to biochemical mechanisms (***Figure 3*** **A-E**).

Although computational approaches such as these are invaluable in the drug discovery pipeline, as they significantly reduce the time and cost of identifying new drug targets, they are still predictive models that require validation using experimental methods.

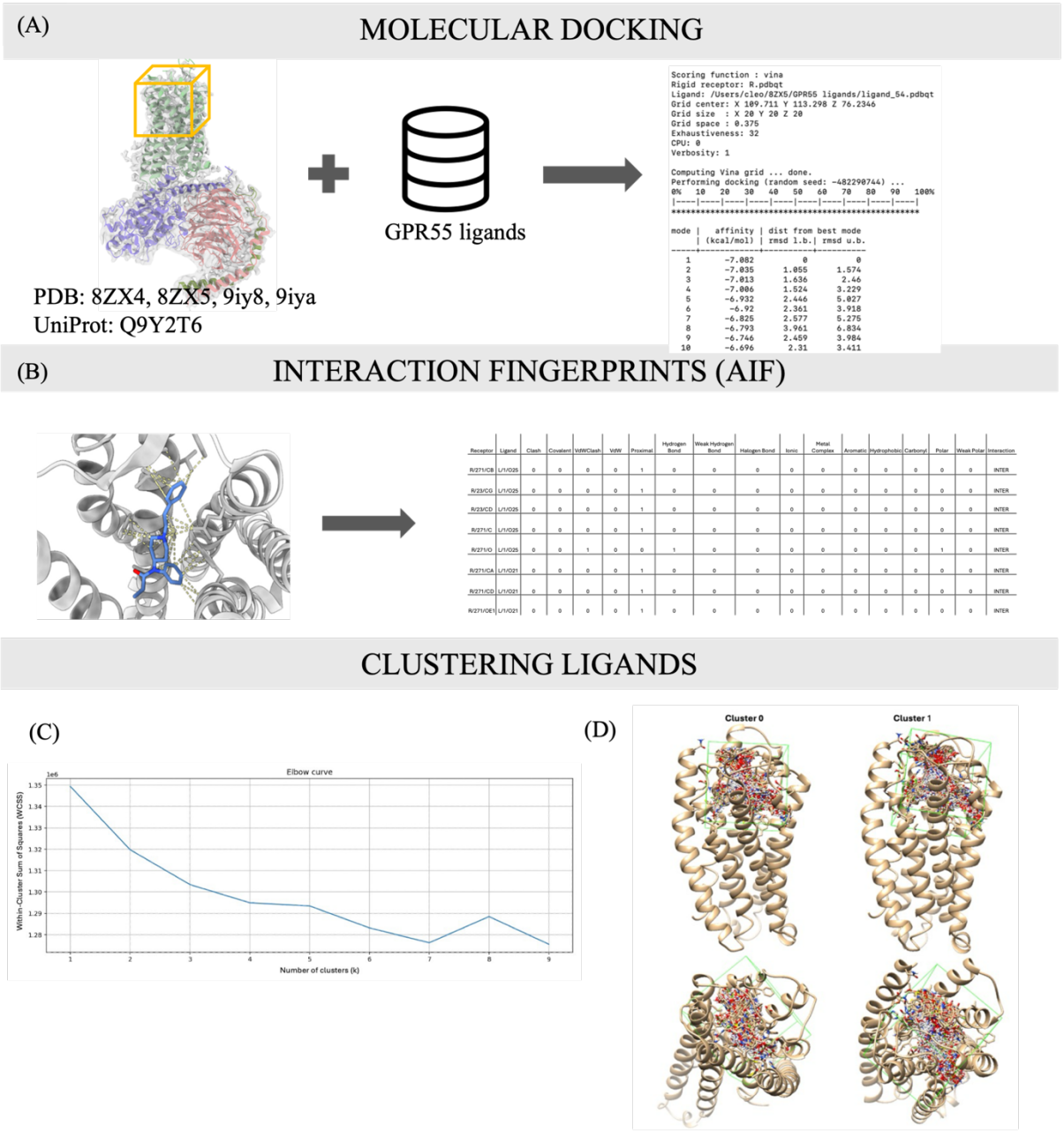


Figure 1 **Molecular docking and interaction fingerprint calculation workflow.**
(A) Molecular docking of GPR55 ligands from open-access repositories to predicted, active and inactive GPR55 structures was performed and docking scores were calculated using Autodock Vina. **(B)** Interatomic interaction fingerprint (AIF) calculations were made using Arpeggio. **(C)** Ligands were grouped based on their interaction fingerprints. The elbow method was used to determine the optimal number of clusters, and representative ligand binding poses for each cluster are shown in **(D)**.

Experimental approaches for identifying ligands for GPR55.

GPR55 pharmacology has been particularly challenging to define, in part because a wide range of experimental assays have produced conflicting results, probably due to the lack of potent, selective ligands and a positive control.

The activity of G proteins, which relay signals from activated GPCRs to downstream effectors, can be directly measured using one of the earliest approaches, the [^{35}S] GTPγS binding assay. This technique works by replacing GTP on the Gα subunit with a radioactive [^{35}S]-labelled guanosine 5′-O-(3-thio) triphosphate ([^{35}S] GTPγS). Since the label is resistant to GTPase hydrolysis, it remains bound, allowing prolonged measurement of receptor activation. In this membrane-based assay, receptor activation is quantified by tracking the incorporation of [^{35}S] GTPγS into G proteins following ligand stimulation (Onaivi, 2008). Using this assay, GPR55 was reported to respond to nanomolar concentrations of several endocannabinoids, including Abn-CBD, THC, and O-1602 (Johns *et al.*, 2007). Although this method is highly sensitive for detecting receptor-G protein coupling, it does not directly reveal which specific G protein is being activated. Additionally, this assay may have a low signal-to-background ratio, making it challenging to detect weak or partial agonists. The reliance on radiolabelled components also presents practical challenges, requiring specialised equipment, high operating costs, and strict safety and waste disposal protocols.
Other groups have used whole-cell-based calcium mobilisation assays, which measure increases in intracellular calcium concentration in response to ligand activation. Using this method, Lauckner *et al.* (2008) reported that cannabinoids such as THC and JWH015 induce intracellular Ca^{2+} increases in both HEK293 cells expressing GPR55 and in dorsal root ganglion neurons. While this assay is convenient and high-throughput, calcium signalling can be a promiscuous readout, as many receptors and ion channels converge on this pathway, making attribution to GPR55 difficult and results hard to reproduce across systems.

Other groups have used extracellular-signal-regulated kinase (ERK) phosphorylation as a marker of receptor activity. This assay measures the activation of the ERK protein, a key component of the mitogen-activated protein kinase (MAP kinase pathway), and is performed using Western blotting, high-throughput immunoassays, or ELISA-based methods. Oka *et al.* (2007), for instance, demonstrated that lysophosphatidylinositol (LPI) elicited ERK phosphorylation and Ca^{2+} release via GPR55, which supported the proposal of LPI as the GPR55's endogenous ligand. However, ERK activation is also a highly convergent signalling outcome influenced by multiple receptors, raising challenges for specificity and reproducibility.

More recently, several groups, including Kapur *et al.* (2009), Kotsikorou *et al.* (2011), and Hewer *et al.* (2023), have adopted whole-cell β-arrestin recruitment assays to assess ligand activity at GPR55. β-arrestins are intracellular adaptor proteins that bind to activated GPCRs, forming stable receptor-arrestin complexes. This interaction can lead to receptor desensitisation but may also trigger distinct downstream signalling pathways (Jean-Charles, Kaur and Shenoy, 2017). Since β-arrestin redistribution to the activated membrane-bound receptor occurs upstream and close to the receptor, this assay is highly sensitive and often less prone to false positive results. However, a key complication in interpreting the results of this assay is the phenomenon of biased signalling. This occurs because different ligands stabilise distinct conformations of the same GPCR, leading to selective activation of one intracellular pathway over another. Biased signalling can also be brought on by the abundance of intracellular G proteins or β-arrestins (systems bias) or the receptor's localisation at the plasma membrane or intracellular compartments (location bias) (Kenakin and Christopoulos, 2013; Sengmany *et al.*, 2019; Mohammad Nezhady, Rivera and Chemtob, 2020). Therefore, reliance on this method alone risks overlooking ligands that preferentially signal through G proteins rather than through β-arrestin pathways. For example, the contradicting results of THC as an agonist shown in this work and by Kapur *et al.* (2009) and Lauckner *et al.* (2008) (***Table 1***).

Another assay of interest is the bioluminescence resonance energy transfer (BRET)-based dissociation assay known as the G protein sensor (G-CASE) biosensor, first developed by Galés et al. (2005) to monitor the real-time interaction between Gα and Gβγ subunits. This assay involves tagging the Gα subunit with a Nano luciferase donor at its N-terminus and tagging the Gβγ subunit with a Venus fluorescent acceptor at the C-terminus of the Gβ subunit. Upon G protein activation, the dissociation of the Gα and Gβγ subunits leads to a decrease in the BRET signal due to increased spatial proximity, which reduces the resonance energy transferred (Schihada, Shekhani and Schulte, 2021). Recently, this assay has been applied to determine $G\alpha_{13}$ and $G\alpha_{q}$ dissociation upon GPR55 activation as a method to determine ligand activity (Xia *et al.*, 2024; Claff *et al.*, 2025).

While cell-based assays provide a powerful means of studying ligand pharmacology in a physiologically relevant context, as they allow receptor activity to be assessed in the presence of the full cellular signalling machinery, they also come with some important limitations. Differences in cell type, receptor expression levels, cellular background effects, and off-target signalling can all influence the results, making these assays difficult to optimise and standardise across laboratories. This highlights the need for more robust and reproducible approaches to study GPR55 pharmacology.

One promising strategy is the membrane-based mG protein recruitment assay (MeGaBRET). This method uses a minimal G (mG) protein which is a mutated version of the Gα subunit's GTPase domain, engineered to be locked in its active state (Carpenter *et al.*, 2016; Carpenter and Tate, 2016). The assay combines isolated luciferase enzyme tagged receptor membranes (BRET donor) and purified Venus tagged mG proteins (BRET acceptor). Upon ligand stimulation, the activated receptor recruits the vmG protein bringing the donor and acceptor into close proximity (***Figure 2***). In the presence of the luciferase substrate furimazine, this proximity produces a measurable BRET signal. The magnitude of the BRET signal is directly proportional to the amount of vmG protein recruited and thus, the level of receptor activation (Harwood *et al.*, 2025).

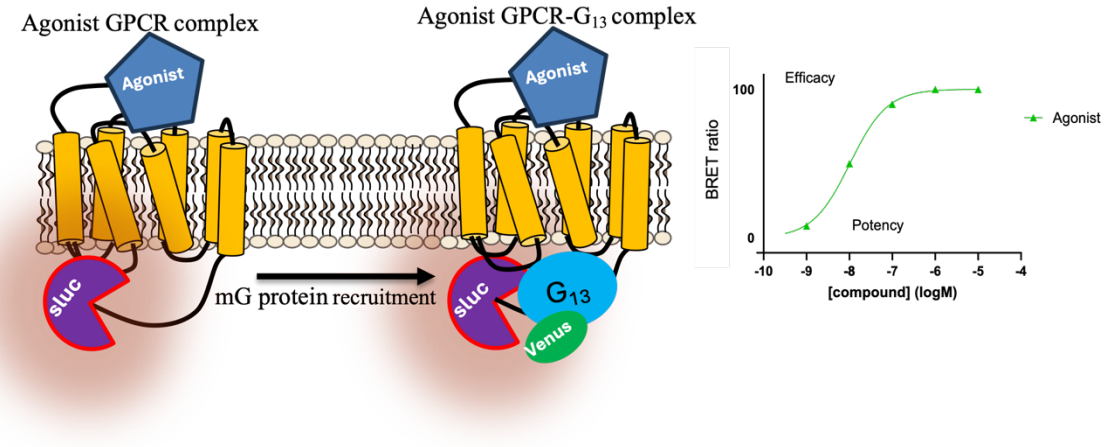


Figure 2. **The membrane-based mG protein recruitment assay (MeGaBRET)**
This assay monitors the recruitment of Venus-tagged mG proteins to GPCRs. The thermostable luciferase (sLuc) enzyme is fused to the C-terminal tail of the receptor. Upon receptor activation, the GPCR recruits the vmG protein, bringing Venus into close proximity with sLuc.

This proximity allows bioluminescence resonance energy transfer (BRET) to occur. Receptor activation is measured as an increase in BRET ratio.

Although isolating the receptor from its cellular environment reduces physiological relevance, the MeGaBRET has minimal background noise, no interference from cellular processes like receptor internalisation and it allows for control over the concentrations of both the receptor and the mG protein, which is critical for obtaining consistent and reproducible data.

Problem statement

GPR55 has emerged as a promising therapeutic target in diseases like cancer, inflammation, and metabolic disorders. However, progress in its pharmacological characterisation has been limited by the lack of potent and selective ligands, as well as the absence of standardised and reproducible assays for determining ligand activity. The overarching aim of this work is therefore to develop improved assays for GPR55 ligand screening.

Aims and Objectives of this investigation.

To achieve this, our first objective is to use computational methods to map key residues within the GPR55 binding site that are important for agonist and antagonist binding. Following the approach of Jiménez-Rosés *et al.* (2022), we hypothesise that by docking a large dataset of ligands into GPR55, calculating their interaction fingerprints, and applying these data to a machine learning model, we can reveal overrepresented receptor residue-ligand interactions. These interactions, in turn, would be key to determining whether a ligand acts as an agonist or antagonist.

Our next objective is to experimentally validate ligand binding using established assays. We will attempt to reproduce β-arrestin recruitment data, which have been used to determine the pharmacological activity of the high-potency GPR55 ligands ML184 and compound 26, within our own experimental systems. To complement this, we will also attempt to replicate the G-CASE assay, another widely used cell-based approach that measures GPR55 activation by monitoring the dissociation of Gα and Gβγ subunits. Comparing the results from these two systems will allow us to evaluate the consistency of pharmacological readouts across cell-based assays.

In addition to these established methods, we introduce a membrane- based mG protein recruitment assay (MeGaBRET) as an alternative approach foe assessing GPR55 ligand activity. By isolating GPR55 in its membrane environment, this approach removes cellular background variability while still capturing direct receptor-G protein interactions, offering a more controllable and sensitive assay for assessing ligand pharmacology.
Taken together, this work is expected to identify key receptor residues involved in ligand binding, provide standardised and reproducible assays for screening GPR55 ligands, establish a novel membrane-based assay to complement current methods, and deliver new insights into the pharmacological properties of benchmark ligands such as ML184. Collectively, these advances will hopefully accelerate the discovery of selective GPR55 ligands and provide new tools for exploring its therapeutic potential.

Table 1. **Comparison of ligand potencies at GPR55 across different assay formats.**
Our experimentally determined EC_{50} values are shown for BRET β-arrestin2 recruitment and the membrane-based Venus-mG13 protein recruitment assay (MeGaBRET). Reported EC_{50} values were extracted from the literature for β-arrestin recruitment, [^{35}S] GTPγS binding, Ca^{2+} mobilisation, and ERK phosphorylation assays. The source for the reported data is indicated in parenthesis under each value. All values are presented in nM as originally reported. "-" indicates no data available in the literature. "no response" represents ligands that displayed no measurable activity in that assay.

Ligand	EC_{50}s (nM)		Reported EC_{50}s (nM)			
	BRET β-arr2	MeGa-BRET vmG_{13}	β-arrestin recruitment	[^{35}S]GTPγS assay	Ca^{2+} assays	ERK activation
Compound 26	9.12	40.7	6.2 [1]	-	low activity [1]	-
Compound 28	9770	2340	660 [1]	-	470 [1]	-
Compound 29	n.d.	10000	2320 [1]	-	515 [1]	-
ML184	550	1100	250 [5]	-	no EC_{50} data [3]	active at 1 μM [5]
LPI	2040	5.6	1200 [4]	1000 [7]	3000 [6]	200 [7]
AM251	27480	2090	9600 [4]	39 [8]	2000 [2]	no effect [4]
THC	no response	245000	no response [4]	8 [8]	5000 [6]	no effect [6]
O-1602	no response	no response	no response [4]	13 [8]	no effect [7]	-
CBD	no response	no response	no response [4]	IC_{50}=350nM [8]	no effect [6]	-
RO7684969	12020	7590	-	-	-	-

[1] (Hewer *et al.*, 2023)
[2] (Henstridge *et al.*, 2010)
[3] (Hill *et al.*, 2018)
[4] (Kapur *et al.*, 2009)
[5] (Kotsikorou *et al.*, 2011)
[6] (Lauckner *et al.*, 2008)
[7] (Oka *et al.*, 2007)
[8] (Ryberg *et al.*, 2007)

Chapter Two: Materials and Method

In silico methods

Dataset preparation

A dataset was compiled using primary open-access repositories: GPCRdb (Pándy-Szekeres *et al.*, 2017), ChEMBL(Mendez *et al.*, 2018), ZINC (Irwin and Shoichet, 2005), and the Guide to Pharmacology (Armstrong *et al.*, 2019). The GPR55 ligand table from GPCRdb was downloaded into a Microsoft Excel spreadsheet and curated using the international chemical identifier (InChI) key (Heller *et al.*, 2013) to remove duplicates and supplement missing simplified molecular input line entry system (SMILES) strings from the other databases. The final dataset comprised 563 reported GPR55 binders, each identified by its corresponding GPCRdb ID number. Then, an additional column was added to assign a ligand pharmacological action label as reported in the literature: agonists were scored as +1, inverse agonists and antagonists as 0, unknown binders as -1, and allosteric modulators as -2. Finally, all ligands were protonated and converted from SMILES strings to PDBQT format using Open Babel v3.1.0 (O'Boyle *et al.*, 2011).

Preparation of Receptor Structures

When computational analysis began, only the AlphaFold model of GPR55 was available. Initial docking experiments used the predicted active-state structure (UniProt: Q9Y2T6) (Jumper *et al.*, 2021). Once experimental structures were released, additional docking was carried out using the LPI-bound GPR55-G_{13} complex (PDB: 8ZX4), the AM251-bound GPR55-G_{13} complex (PDB: 8ZX5) (Xia *et al.*, 2024), the ligand-free apo-GPR55-G_{13} complex (PDB: 9IY8) and the antagonist-bound GPR55-Fab-Nb-ONO-9710531 complex (PDB: 9IYA) (Chang *et al.*, 2024). To validate the machine learning results, further small-scale molecular docking was performed using the ML184-bound GPR55-G_{13} complex (PDB: 9GE2) (Claff *et al.*, 2025), as this structure provides clearer insight into potential allosteric binding sites. Structures were protonated using Reduce from the Richardson lab and converted to PDBQT format using the prepare_receptor4.py tool, both of which are available in ADFRsuite (Ravindranath *et al.*, 2015).

Molecular Docking

Semi-flexible molecular docking was performed against the five GPR55 structures using AutoDock Vina (Trott and Olson, 2010; Eberhardt *et al.*, 2021) generating up to ten ligand binding poses per compound. The docking grid box, centred on the orthosteric site, was consistently defined as 20 × 20 × 20 Å using UCSF Chimera (Pettersen *et al.*, 2004). An exhaustiveness parameter of 32 was used to ensure a thorough search of the ligand conformational space.

Calculating the interaction fingerprints

After docking, the output files were split so that each ligand pose could be processed separately. The receptor and ligand structures were converted back to PDB format and cleaned, removing extra and unwanted atoms. Each receptor structure and each ligand pose were appended into a single complex file. Then, the Arpeggio software (Jubb *et al.*, 2017) executed in the Docker environment (Merkel, 2014) was used to calculate interatomic interaction fingerprints (AIFs) within each docked complex. Arpeggio determined whether specific types of atomic interactions occur between the ligand and receptor, based on distance and angle criteria. Each

possible interaction was then recorded as either present (1) or absent (0) and saved as tables in CSV format.
The Arpregio interaction data, stored as individual CSV files for each ligand-receptor pose, were then processed into a machine learning-ready format using a custom Python script. The CSV files were processed into an MxN binary matrix, where M represented ligand poses (ligand GPCRdb ID_docking pose number) and *N* represented unique atomic interactions (receptor residue number/interacting atom-ligand interacting atom and interaction type), for example, ligand 54_04 and 401/O-N Polar, respectively. A value of 1 indicated the presence of a specific interaction in a given pose, while 0 indicated its absence; undefined (NaN) values in the original AIF files were imputed as 0 to ensure complete binary matrices.

ML data preparation and feature engineering

To assess the influence of feature granularity on model performance and interpretability, we created four distinct matrices for model training. These matrices were designed to represent ligand-receptor interactions at different levels of detail, from broad to highly specific. The broadest granularity matrix included features representing interactions between the entire ligand and an entire amino acid residue of the receptor, characterised by the type of interaction (e.g., 177- L/1/ Aromatic). This provided a general overview of which residues were most important for binding. We then created two matrices of intermediate granularity. The first described features based on interactions between an entire amino acid residue and a specific atom on the ligand (e.g., 177 - L/1/C37 Hydrophobic). The second version was based on interactions between a specific atom on the amino acid with the entire ligand (e.g., 177/CH2 - L/1/ Hydrophobic). The matrix with the highest level of granularity defined the specific interaction between individual atoms on the receptor and individual atoms on the ligand (e.g., 177/CZ2 - L/1/C36 Hydrophobic). This procedure was applied to all receptor-ligand pose pairs and resulting processed matrices were saved in Apache Parquet format for model training.

Unsupervised clustering for binding mode analysis

Then, another custom Python script, was used to merge the processed docking pose interaction tables with the pharmacological action labels (“agonist”, “antagonist,” or “binder” if unknown). Each docking pose was represented as a binary interaction vector, where a value of 1 indicated the presence of a given receptor-ligand atomic interaction and 0 indicated its absence; undefined values were imputed as 0. For clustering, only interaction features were retained, while ligand identifiers and activity data were removed to prevent bias.
To investigate whether docked poses could be grouped according to distinct binding modes, K-means clustering was applied to the binary interaction matrices for each receptor. The optimal number of clusters was estimated using an elbow plot based on the Within-Cluster Sum of Squares (WCSS), calculated as:

$$WCSS = \sum_{k=1}^{K} \sum_{x_i \epsilon C_k} \| x_i - \mu_k \|^2$$

where K is the number of clusters, x_i are data points in cluster C_k, and μ_k is the centroid of cluster *k*. The optimal number of clusters corresponds to the point where increasing K further results in diminishing returns in reducing WCSS (“the elbow”).

The resulting clusters were then manually inspected in PyMOL (The PyMOL Molecular Graphics System, Version 3.10, Schrödinger, LLC) to ensure all ligand clusters remained in the predefined orthosteric binding grid.

CatBoost and SVM analysis for ligand activity prediction

Another custom Python workflow was used to train a CatBoost classifier (Liudmila Ostroumova *et al.*, 2017) to predict ligand pharmacological activity from protein-ligand contact data. CatBoost is a gradient-boosting machine learning model well suited for handling tabular datasets, which identified the most overrepresented contacts and highlighted them as the crucial interactions likely to drive binding and pharmacological outcomes.

First, missing interaction values were replaced with zero to represent absent contacts, interaction feature names were cleaned for consistency, and uninformative or redundant features, such as those describing proximal clashes, were removed to reduce noise. The dataset was then split into feature (X) and target (Y) matrices with ActivityData as the target. The CatBoost model was trained over 1000 iterations, using an 80:20 train-test split, to classify ligands as agonists or antagonists based on the contact data. Model performance and feature relevance were assessed using: PredictionValuesChange- measuring how much predictions shift when a feature changes, LossFunctionChange- estimating how much a feature contributes to reducing the model's error, and Interaction scores- highlighting strong pairwise feature effects.

To further enhance model interpretability, the Shapley Additive explanations (SHAP) method (Lundberg and Lee, 2017) was used to quantify both local and global feature contributions. SHAP is derived from cooperative game theory and provides a way to fairly distribute the output of a machine learning model among its features. It estimates how much each receptor-ligand interaction contributes to the final prediction by testing how the prediction changes when that interaction is included or removed.
A SHAP summary plot was generated to highlight the top 20 most influential features across the dataset. SHAP plots from each receptor structure were combined and manually scored based on the impact of each interaction on the model to identify the residues most important for ligand binding.

Classification accuracy and performance matrices

To independently validate the classification accuracy, a support vector machine (SVM) classifier was also trained on the identical 80:20 train-test split of the contact data. Performance was primarily evaluated using a confusion matrix, which provided a visual and quantitative breakdown of the classification outcomes. From the confusion matrix true positive (TP), true negative (TN), false positive (FP), and false negative (FN) values, the Matthews correlation coefficient (MCC) was calculated as a single measure of binary classification quality. MCC calculations are valuable for assessing the performance on potentially imbalanced datasets (Matthews, 1975). The MCC is defined as:

$$MCC = \frac{TP \times TN - FP \times FN}{\sqrt{(TP + FP)(TP + FN)(TN + FP)(TN + FN)}}$$

MCC values range from -1 to +1. A value of -1 indicates total disagreement between the prediction and observation. An MCC of 0 indicates no correlation meaning the prediction was no better than random guessing. A value of +1 indicates a perfect correlation where all the positives correctly predicted positives and all the negatives correctly predicted negatives.

In vitro Materials and Methods

Materials

Molecular biology materials

Q5® High Fidelity 2× Master Mix (New England BioLabs, MO492L), Phusion® High-Fidelity PCR Master Mix with GC Buffer (ThermoFisher Scientific, F523S), PrimeSTAR® HS DNA Polymerase (Takara, R040A), SYBR™ Safe DNA gel stain (Invitrogen, S33102), agarose powder (Sigma-Aldrich, A9539-250G), GeneRuler™ 1 kb DNA Ladder (ThermoFisher Scientific, SM0311), carbenicillin (Fisher Scientific, BP2648-5), DpnI 10 U/µL (Promega, R6231), and One Shot® TOP10 Chemically Competent E. coli stored at -80 °C, and pre-treated with manganese chloride (ThermoFisher Scientific, MA, USA).

Mammalian cell culture reagents

All mammalian cell culture centrifugation was performed using a Thermo Scientific™ Heraeus™ Megafuge™ 8 bench-top centrifuge, while cells were counted using a Countess™ II FL Automated Cell Counter (Invitrogen™). Suspension cells Expi293F™ Inducible GnTI$^-$ (catalogue no. A39242) and Expi293™ Expression Medium (catalogue no. A14351-01), Gibco purchased from ThermoFisher Scientific. Suspension culture flasks are Nalgene™ Single-Use PETG Erlenmeyer Flasks, sterile, plain bottom (catalogue no. 4115-0125) (Thermo Scientific). HEKT-Rex™-293 cells (Invitrogen, CA, USA). T75 and T175 cell culture flasks (Fisher Scientific, Loughborough, UK). From Sigma-Aldrich (St. Louis, MO, USA): foetal calf serum (FCS), Dulbecco's Modified Eagle Medium, high glucose (catalogue no. D6429), Dulbecco's DPBS, Hank's Buffered Saline Solution (HBSS)(H8264), HEPES (4-(2-hydroxyethyl)-1-piperazineethanesulfonic acid) (catalogue no. RDD035-100G), bovine serum albumin (BSA) heat shock fraction, protease-free, fatty acid-free, essentially globulin-free (A7030), trypsin/EDTA solution (catalogue no. R001100). From Gibco™ (MA, USA): Opti-MEM™ Reduced Serum Medium (catalog no. 31985062), Blasticidin™ (catalog no. 12172530), Zeocin™ (catalog no. R25005), Geneticin™ (G-418 Sulfate) 50mg/mL (catalog no. 10131035), Trypan Blue (catalogue no. 15250061). Sheared salmon sperm DNA (Invitrogen, catalogue no. AM9680). Cellstripper™ (catalogue no. 25-056-Cl) from Corning® (Corning, NY, USA). LabMed buffer and HTRF Taglite SNAP-Lumi4-Tb labelling reagent (5X) (100mL LABMED) from Cisbio (Codolet, France). The transfection reagent Polyethylenimine (PEI) (25 kDa) was obtained from Polysciences (catalogue no. 23966-1). (Polysciences Inc., PA, USA). 96-well Cellstar® tissue culture plates (Greiner Bio-One, Austria).

mG protein purification reagents

HisTrap FF crude 5-mL columns were obtained from GE Healthcare (IL, United States). Vivaspin protein concentrators were obtained from Sartorius (Gottingen, Germany). NuPAGE LDS Sample Buffer, NuPAGE 4%-12% Bis-Tris 15 × 1.0 mm well gels, NuPAGE MOPS SDS

Running Buffer, PageRuler Prestained Protein Ladder, were all obtained from Thermo Fisher (MA, United States).

G-CASE plasmids

G-CASE plasmids were obtained from Addgene (Teddington, UK) and included G_i-CASE (cat. No. 168120), G_{13}-CASE (cat. No. 168127), and G_q-CASE (cat. No. 168125) as described by Schihada, Shekhani and Schulte (2021), as well as G_{12}-CASE (cat. No. 190714) from Schihada *et al.* (2022). Human codon-optimised fragments encoding mini-G sequences, as described by Nehmé *et al.* (2017) were subcloned into pJ411 plasmids and expressed in *E. coli* BL21(DE3) LOBSTR cells (cat. No. NC1789768, Fisher Scientific).
OptiPlate-384 (white opaque 384-well microplate) was purchased from PerkinElmer (Beaconsfield, United Kingdom). The furimazine solution was obtained from Promega, Mannheim, Germany (final assay dilution: 1:5000).

Compounds

ML184 cat. No. SML2884, AM251 cat. No. A6226, L-α-lysophosphatidylinositol sodium salt (LPI) cat. No. 440153 and Δ9-Tetrahydrocannabinol solution (THC) cat. No. T2386 were purchased from Sigma-Aldrich. 5-Methyl-4-[(1R,6R)-3-methyl-6-(1-methylethenyl)-2-cyclohexen-1-yl]-1,3-benzenediol (O-1602) cat. No 2797 was from Tocris Bioscience. Cannabidiol (CBD) was a gift from ETH Zurich. RO7684969, Compound 29 (RO7834928), Compound 28 (RO7836051), and Compound 26 (RO7837547) (Hewer *et al.*, 2023) were from F. Hoffmann-La Roche Ltd. All ligands were dissolved in 100% DMSO and stored as aliquots at -20°C until required. Dimethyl sulfoxide (DMSO, 276855) was purchased from Sigma-Aldrich.

Instruments and software

Primers were designed using the Aascan PCR cloning software (Sun *et al.*, 2013). Signalling assays were performed in the BMG PHERAstar FSX plate reader (BMG Labtech, Offenburg, Germany), fitted with BRET1 plus optic module (ex. 475/30 nm, em. 535/30 nm) and MARS software purchased from BMG Labtech (Offenburg, Germany). GraphPad Prism 10 was purchased from GraphPad Software (San Diego, United States). Microsoft Excel™ XP was purchased from Microsoft (Washington, United States).

Construct design

All constructs containing GPR55 were generated using the pcDNA4TO-TwinStrep (pcDNA4TO-TS) vector backbone, with sequence design and assembly visualised using ApE (Davis and Jorgensen, 2022) and Benchling software (Benchling, 2024). Backbones were derived from previously constructed plasmids, and the GPR55 coding sequence was originally sourced from the PRESTO-Tango plasmid library.
Constructs had the thermostable luciferase enzyme (sLuc). C-terminal constructs (C01, C02, and C03) placed the sLuc enzyme after the receptor, again using either a GSGS linker (C01), or the last 20 amino acids from the C-terminus of CB2 (C02) or β_2-adrenergic receptor (C03) as linkers. SNAP-tagged constructs were also generated by inserting the SNAP tag at the N-terminus of GPR55, linked by 10 amino acids derived from the CB2 receptor N-terminus (SNAP_CB2(1-10) _GPR55). A wild-type (WT) GPR55 construct was also generated by

inserting a stop codon (TAA) immediately after the GPR55 coding sequence to prevent the addition of any C-terminal tags (***Figure 3*** A-E).

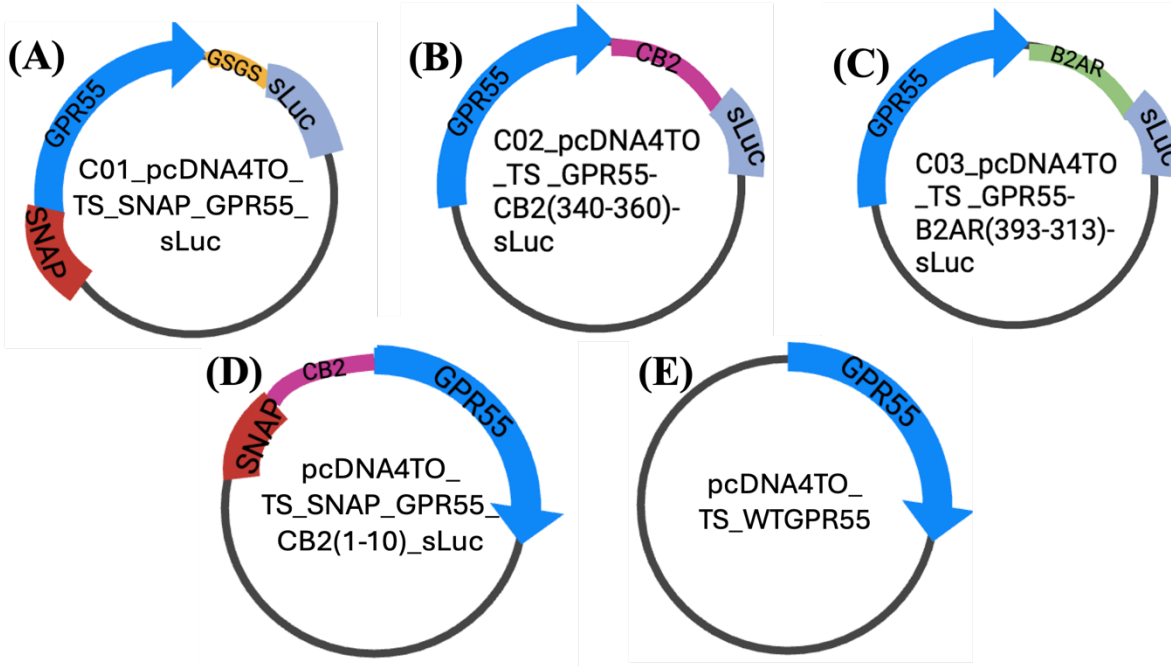


Figure 3. **Plasmid maps of GPR55 constructs.**
Schematic representations of the pcDNA4TO mammalian expression plasmids encoding various GPR55 constructs. (A) C01 encodes GPR55 fused at its C-terminus to sLuc through a flexible GSGS linker. (B) C02 encodes GPR55 fused to sLuc via a CB2-derived linker (residues 340-360). (C) C03 encodes GPR55 fused to sLuc via a β_2AR-derived linker (residues 393-313). (D) This construct has an N-terminal SNAP-tag on GPR55, and an N-terminal fragment of the CB2 receptor (residues 1-10, pink) as the linker between the SNAP-tag and GPR55. (E) This plasmid expresses the wild-type GPR55 receptor without any N-terminal tags or C-terminal fusions.

Molecular biology methods

Primers for GPR55 in pcDNA4TO-TwinStrep constructs were designed using Aascan software (Sun *et al.*, 2013). All primers were ordered from Sigma-Aldrich as desalted oligonucleotides and used without further purification.

Polymerase chain reactions (PCR)

PCR amplification of insert and backbone fragments was performed using either Q5/Phusion HF or PrimeSTAR HS polymerases. Insert reactions (10 µL) contained 0.5 µL template DNA (0.1 ng/µL), 0.2 µL each of forward and reverse primers (10 µM), 4.1 µL Milli-Q water, and 5 µL of either 2× Q5 polymerase or Phusion polymerase master mix. Backbone reactions (25 µL) contained 1.25 µL template, 1 µL each of primers, 10.25 µL water, and 12.5 µL 2× PrimeSTAR HS. Touchdown PCR was carried out on a PCR MAX Alpha Cycler 2 using polymerase-specific conditions. For PrimeSTAR HS: initial denaturation at 98 °C for 1 min, followed by 20 cycles of annealing from 68 °C to 58 °C (-0.5 °C per cycle), then 10 cycles at

62.5 °C, with elongation at 72 °C for 1 min/kb. For Q5 and Phusion HF: 20 cycles of annealing from 65 °C to 55 °C, followed by 10 cycles at 62.5 °C, with 30 s/kb elongations. All reactions ended with a 5-minute final elongation at 72 °C and a 10 °C hold.

Agarose Gel Analyses of PCR Products

PCR products were analysed by agarose gel electrophoresis. A 1% agarose gel was prepared by dissolving 0.5 g agarose in 50 mL 1× TAE buffer, followed by the addition of 2.5 µL SYBR Safe once the mixture had cooled to ~50 °C. Samples were prepared by mixing 2 µL PCR product with 2 µL Milli-Q water and 1 µL 5× loading dye. Gels were run in a Fisherbrand™ Sub-Gel Midi unit submerged in 1× TAE buffer, using 2 µL GeneRuler™ 1 kb DNA ladder as a size marker. Electrophoresis was performed at 90 V for 40 minutes using a Fischer Scientific nanoPAC-300P Power Supply (300 V, 400 mA, 60 W), and bands were visualised with a Clare DR-45M Dark Reader Transilluminator. PCR conditions were optimised as needed by adjusting Cycle 1 annealing temperatures ±3 °C to resolve band clarity.

DNA purification

Template DNA clean-up was performed by adding 0.2 µL of DpnI restriction enzyme to each PCR product. Reactions were incubated at 37 °C for 3 hours, followed by 16 °C for 11 hours, and held at 4 °C using a PCR MAX Alpha Cycler 2. PCR products were then purified using the MinElute Reaction Cleanup Kit (Qiagen) according to the manufacturer's instructions and eluted in 10 µL Milli-Q water. DNA concentrations were measured using a DeNovix DS-11 FX spectrophotometer.

Gibson Assembly

Purified PCR products were assembled using Gibson Assembly®. A typical reaction included a 3:1 molar ratio of insert to backbone, with a total of 50 ng DNA. Reactions were incubated at 50 °C for 15 minutes, followed by 45 °C for 1 hour using a PCR MAX Alpha Cycler 2.

Transformation in E coli

Agar plates were prepared by autoclaving 12.5 mL of liquified Luria broth (LB) agar, allowing them to cool to ~50 °C, then adding 100 µg/mL of carbenicillin before pouring and allowing to set for at least 20 minutes. All transformation procedures were carried out using aseptic technique next to a Bunsen burner to maintain sterility. 15-60 µL of chemically competent *Escherichia coli* Top10 cells (thawed on ice) were mixed with 4 µL of assembled plasmid DNA. The mixture was incubated on ice for 25 minutes, heat-shocked at 42 °C for 30 seconds, then returned to ice for 2 minutes before spreading onto an agar plate and incubating overnight at 37 °C.

Plasmid Preparation

The following day, three individual colonies were picked for each construct and inoculated into 14 mL culture tubes containing 5 mL Luria Broth supplemented with 100 µg/mL carbenicillin. Cultures were incubated for up to 20 hours at 37 °C and 220 rpm in a Stuart SI600 shaking incubator to selectively enrich successfully transformed bacteria. Following incubation, cultures were centrifuged for 10 minutes at 4122 × g (max speed) using a ThermoFisher Multifuge X3 F3. Plasmid DNA was then isolated using the QIAprep Spin Miniprep Kit

(Qiagen, Hilden, Germany) following the manufacturer's instructions and eluted in 50 µL Milli-Q water. DNA concentrations were measured using a DeNovix DS-11 FX spectrophotometer. Samples are then sent to Sorce BioScience for Sanger sequencing, and the results are analysed using Benchling.

Suspension Cell Culture

Thawing cells

Cryopreserved cells were rapidly thawed in a 37 °C water bath and transferred into a sterile 125 mL PETG plain-bottom flask with a vented cap containing 30 mL of pre-warmed Expi293™ Expression Medium. Cultures were incubated at 37 °C with 8% CO_2 and shaken at 120 rpm.

Cell subculturing

Suspension Expi293F™ cells were passaged upon reaching a density of 3–5 × 10^6 cells/mL. Cells were counted using a Countess™ II FL Automated Cell Counter (Invitrogen™) after mixing 20 µL of cell suspension with 20 µL trypan blue (Gibco™) and loading 10 µL into each chamber of a glass haemocytometer slide, then diluted to make 30 mL of 3 × 10^5 cells/mL in pre-warmed Expression Medium and incubated at 37 °C with 8% CO_2, shaking at 120 rpm.

Transfection

Transfections were performed using a 3:1 PEI: DNA (1 µg) mass ratio. For each 1 mL of culture, 100 µL of PEI in Opti-MEM™ and 100 µL of DNA in Opti-MEM™ were prepared separately, vortexed, and incubated at room temperature for 5 minutes. The solutions were then combined, vortexed, and incubated for 20 minutes to allow complex formation.
Expi293F™ cells (>95% viability) were centrifuged at 300 × g for 3 minutes, washed with DPBS, and resuspended in pre-warmed expression medium at 3 × 10^6 cells/mL. The DNA-PEI complex was added dropwise to the cell suspension and mixed by swirling. Cultures were incubated at 37 °C, 8% CO_2, 120 rpm, monitored for growth every 24 hours, induced with 1µg/mL tetracycline after 48 hours and harvested 48 hours post-induction.

Cell Cryopreservation

Expi293F™ cells were frozen at a density of 3-5 × 10^6 viable cells/mL. Cells were harvested by centrifugation at 300 × g for 5 minutes, the supernatant discarded, and the pellet resuspended in ice-cold Expi293™ Expression Medium with 10% DMSO. The cell suspension was adjusted to a final density of 1 × 10^7 cells/mL in a total volume of 1 mL cryovials, gradually frozen at -80 °C and transferred to liquid nitrogen for long-term storage.

Adherent Cell Culture

Thawing cells

Cryopreserved cells were rapidly thawed in a 37 °C water bath and transferred into 10 mL of pre-warmed Dulbecco's Modified Eagle's Medium (DMEM; Sigma-Aldrich) supplemented with 10% foetal calf serum (FCS) under sterile conditions in a laminar flow hood. The cell suspension was centrifuged at 1000 rpm for 5 minutes, the supernatant was discarded, and the pellet was resuspended in 1 mL of DMEM. Cells were then transferred into a T75 flask (ThermoFisher Scientific) containing 19 mL of DMEM and incubated at 37 °C with 5% CO_2.

Cell Subculturing

HEK cells were passaged at ~80% confluency. The spent DMEM was aspirated, and cells were washed with 5 mL Dulbecco's Phosphate-Buffered Saline (DPBS; Sigma-Aldrich), which was then aspirated. Cells were detached by adding 1 mL of trypsin and incubating for up to 5 minutes. Trypsinisation was neutralised with 9 mL of DMEM, the suspension was transferred to a universal flask and centrifuged at 1000 rpm for 3 minutes. The supernatant was discarded, and the cell pellet was resuspended in 10 mL of fresh DMEM. 1 mL of the cell suspension (corresponding to a typical 1:20 dilution) was added to a T75 flask containing 19 mL of DMEM and incubated at 37 °C with 5% CO_2.

Transfection and generation of stable cell lines

Suspension transfection of HEK293TR cells

Suspension transfections were carried out in HEK293T cells cultured in poly-D-lysine-coated 96-well plates. Cells were harvested by trypsinisation, centrifuged, and resuspended in complete DMEM supplemented with 10% FBS and 1% penicillin-streptomycin. The suspension was adjusted to a density of 2.5×10^5 cells/mL, and 1.2 mL was prepared. DNA: PEI complexes were generated by diluting 1 µg of plasmid DNA in 100 µL of Opti-MEM and, in a separate tube, diluting 3 µL of a 1 µg/µL PEI stock in 100 µL of Opti-MEM. Both solutions were vortexed, combined, and incubated for 20 min at room temperature. The resulting 200 µL complex mixture was added to the 1.2 mL cell suspension, which was gently inverted to mix, and 100 µL of this preparation was seeded into each well of a 96-well plate. Cells were incubated at 37 °C in 5% CO_2, and experiments were performed 48 h post-transfection, when cultures had reached approximately 60% confluency.

Adherent transfection of HEK293TR cells

Cells were passaged to achieve 70-90% confluency the following day. The spent culture media was aspirated and replaced with 5 mL of fresh culture medium with 1 µg/mL penicillin-streptomycin. To prepare the DNA: PEI complex, 5 µg of plasmid DNA was added to 250 µL of Opti-MEM in one microcentrifuge tube, and 1 µg/µL PEI was mixed with 250 µL of Opti-MEM in a second tube. Both tubes were vortexed thoroughly and incubated for 5 minutes. The PEI mixture was then added to the DNA solution, vortexed, and incubated at room temperature for 20 minutes to allow complex formation. The DNA: PEI complex was added to the T75 flask containing the prepared cells, gently mixed by swirling, and incubated at 37 °C with 5% CO_2. Then, ~24 hours post-transfection, 10 mL of fresh culture medium was added to the flask.

For transient transfections, cells were harvested around 48 hours after transfection. For stable cell line generation, cells were transferred at this time point into a T175 flask containing 35 mL of fresh culture media and selection antibiotic. Final concentrations used were: Zeocin™ (20 µg/mL; Invitrogen™), (5 µg/mL; Invitrogen™), or Geneticin® (G-418 sulphate, 400 µg/mL), depending on the resistance cassette of the plasmid. The culture medium was replaced every 3-5 days, and cells were passaged upon reaching full confluency, with selection agents maintained throughout. Once stable colonies were formed, cells were either seeded to a T75 flask for further growth and assays or cryopreserved.

Cell Cryopreservation

HEK293 cells were frozen at ~90% confluency. Following the same steps as cell passaging, cells were detached using trypsin, neutralised with DMEM, and counted using an automated cell counter. Cells were centrifuged at 1000 rpm for 5 minutes, the supernatant was aspirated,

and the pellet was resuspended in freezing medium (FCS + 10% DMSO) to a final concentration of 1-5 × 10^6 cells/mL. Aliquots of 0.5 mL were transferred to cryovials and gradually frozen at -80 °C using a CoolCell™ LX container (Corning), then transferred to liquid nitrogen for long-term storage.

Membrane preparation

All GPR55 membranes were prepared from suspension Expi293F™ cell cultures. All membrane preparation steps were conducted at 4 °C and on ice to avoid tissue degradation. Cells were harvested by centrifuging the culture at 1000 × g for 5 minutes, after which the pellet was resuspended in 20 mL of ice-cold assay buffer containing 10 mM HEPES (pH 7.4) and 10 mM EDTA (pH 8.0). The suspension was homogenised using a Polytron homogeniser (Ultra-Turrax, setting 6) with six 1-second pulses. The homogenate was centrifuged at 1200 × g for 5 minutes at 4 °C (ThermoScientific Multifuge XT), and the resulting supernatant was collected and ultracentrifuged at 48000 × g for 30 minutes at 4 °C using a Beckman Avanti J-25I ultracentrifuge with a JA-25.50 rotor. The resulting membrane pellet was resuspended in 20 mL of fresh ice-cold assay buffer (10 mM HEPES, pH 7.4, 10 mM EDTA, pH 8.0), homogenised again using the same Polytron settings, and centrifuged under the same conditions as above. The final membrane pellet was resuspended in 500 µL of buffer (10 mM HEPES, 0.1 mM EDTA), and an additional 500 µL of the same buffer was used to rinse the tube, yielding a total of 1 mL of membrane suspension. The sample was homogenised by passing it 10 times through a 23G needle. Membrane protein concentrations were determined using the Bicinchoninic Acid (BCA) Protein Assay Kit (Thermo Fisher Scientific) with BSA as a standard, after which membranes were aliquoted, snap-frozen in liquid nitrogen, and stored at -80 °C.

Recombinant protein expression and purification of mG proteins

His-TEV-Venus-mini-G and His-TEV-mini-G were expressed in *E. coli* BL21(DE3) LOBSTR cells. Cells were transformed and plated on LB-agar containing 50 µg/mL kanamycin for selection. Colonies were used to inoculate 800 mL cultures of Terrific Broth (Gibco) with glycerol and 50 µg/mL kanamycin. Cultures were grown at 37 °C with shaking at 200 rpm until reaching an optical density (OD_{600}) of 0.6, at which point protein expression was induced by the addition of 1 mM isopropyl β-D-1-thiogalactopyranoside (IPTG). Induced cultures were incubated overnight at 25 °C, 200 rpm. Cell pellets were harvested from the overnight cultures by centrifuging at 4200rpm for 10 minutes at 4°C (ThermoScientific Multifuge XT).

Cell pellets from overnight cultures were resuspended on ice in 50 mL of lysis buffer (40 mM HEPES (pH 7.5), 100 mM NaCl, 10 mM imidazole, 10% (v/v) glycerol, 5 mM $MgCl_2$, 5 µM guanosine diphosphate (GDP), 5 mM dithiothreitol (DTT), 1 mM phenylmethylsulfonyl fluoride (PMSF), and a complete protease inhibitor cocktail tablet (Roche). Resuspension was performed using a Dounce homogeniser. Then, cells were lysed on ice by sonication using a VibraCell probe sonicator with five 60-second pulses. The lysate was centrifuged at 14000 rpm for 45 minutes at 4 °C using a Multifuge X3 with a Fiberlite F15-6x100y rotor. The resulting supernatant was filtered through a 0.45 µm cellulose acetate filter and loaded onto a 5 mL HisTrap FF crude column using an ÄKTA™ Start protein purification system at a flow rate of 5 mL/min. The column and system were pre-equilibrated with 10 column volumes (CV) of buffer A (40 mM HEPES, pH 7.5, 100 mM NaCl, 10 mM imidazole, 10% glycerol, 5 mM $MgCl_2$, 5 µM GDP, and 5 mM DTT). Unbound proteins were removed with 10 CV of buffer

A. Bound His-tagged proteins were eluted over an 8 CV gradient from 0% to 100% buffer B (40 mM HEPES, 100mM NaCl, 5000 mM Imidazole, 10% glycerol, 5mM MgCl, 5 µM GDP, 4 mM DDT).

The purity and presence of His-TEV-Venus-mini-G or His-TEV-mini-G were identified by SDS-PAGE followed by staining with InstantBlue® Coomassie protein stain (Abcam). The fractions containing mG protein were pooled and concentrated using Vivaspin protein concentrators with either 10,000 or 30,000 molecular weight cut-offs (MWCO), by centrifugation at 3,000 × g and 10 °C in 15-minute intervals for 2-3 hours.

Concentrated proteins were buffer exchanged into assay buffer (40 mM HEPES, 100 mM NaCl, 5 mM $MgCl_2$, 10% glycerol, 5 µM GDP, 5 mM DTT) via overnight dialysis at 4 °C with gentle stirring. Or by buffer exchange using PD-10 desalting columns with Sephadex™ G-25 resin (Cytiva). The final purified mG proteins were snap-frozen in liquid nitrogen and stored at -80 °C until needed.

Membrane-based mG protein recruitment assay (MeGaBRET)

mG recruitment assays were performed in 50 µL reaction volumes using white 384-well OptiPlates (Revvity). The final assay buffer consisted of 10 mM HEPES (pH 7.5), 1 mM $MgCl_2$, 1 mM $CaCl_2$, 5 mM KCl, 0.1% BSA, and 0.01% pluronic F-127 (pH 7.4) prepared in Milli-Q water. GPR55 membranes added per well were adjusted to achieve a baseline of at least 100,000 counts. Varying concentrations of vmG (15-300 nM) and 10 µM furimazine were added to the wells. The plate was immediately read at 30 °C using a PHERAstar FSX plate reader for 5 minutes to establish a baseline luminescence signal. Following this, 0.5 µL of either DMSO (vehicle control) or 10x ligand solution was added to each well (***Figure 4***), and the plate was read continuously for up to 120 minutes.

Whole cell-based β-arrestin and G-CASE assays.

For G-CASE assays, stable HEK293 T-Rex™ cells expressing G_{13}, G_{12}, G_q, or G_i and either pcDNA4/TO-TS-WTGPR55, pcDNA4/TO-TS-SNAP-GPR55 or pcDNA4TO_TS_SNAP_ GPR55_CB2(1-10)-sLuc were seeded at a density of 50,000 cells per well in white 96-well plates, in a final volume of 100 µL/well. Cells were maintained at 37 °C and 5% CO_2 until 90% confluent, then induced with 1 µg/mL tetracycline for 24 hours. For β-arrestin recruitment assays, stable HEK293 T-Rex™ cells expressing β-arrestin and either C01_pcDNA4TO _TS_GPR55-sLuc, C02_pcDNA4TO_TS_GPR55-CB2(340-360)-sLuc, or C03_ pcDNA4TO _TS_GPR55-β_2AR (413–393)-sLuc constructs were plated under identical conditions, then induced for 48 hours before conducting the assay.

After induction, plates were washed once with 100 µL per well of assay buffer (HBSS, 10 mM HEPES (pH 7.5) and 0.1% BSA). After which, 99 µL/well of assay buffer containing 10 µM furimazine was added. The cells were incubated in this assay buffer at 37 °C with 5% CO_2 for 15 minutes. Then, a white back seal was applied to the underside of each plate, and baseline luminescence was recorded using a PHERAstar FSX plate reader at 37 °C with the BRET1 module for 5 minutes. The reader was then paused, and 1 µL of either DMSO or 10× ligand concentration was added to each well (***Figure 4***). Luminescence readings were resumed for 30 minutes at 1-minute intervals.

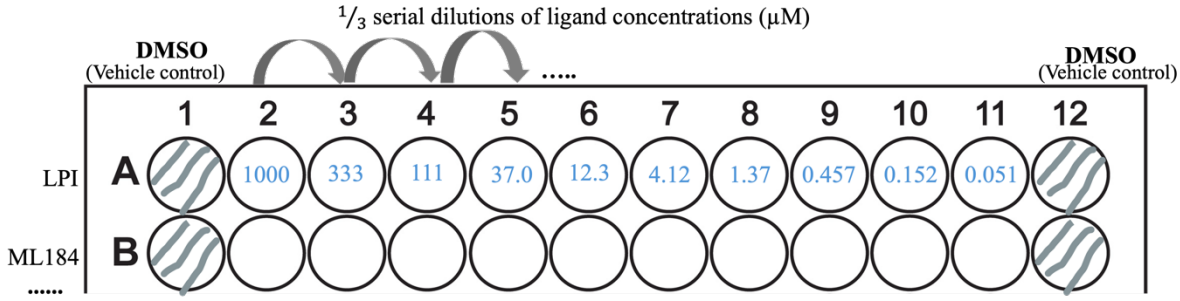


Figure 4. **Schematic of 10X ligand stock solutions preparation for functional assays.** The 10X ligand stock solutions were prepared in a 96-well dilution plate to ensure consistent ligand concentration across all functional assays. The concentration range was generated via a 10-point, threefold serial dilution, spanning from a maximum concentration of 1000μM (Column 2) to a minimum of 0.051μM (Column 11). All ligands were dissolved in DMSO (dimethyl sulfoxide). The plate included two sets of DMSO (vehicle) controls in Column 1 and Column 12. The peripheral placement of the DMSO control wells also served the purpose of minimising evaporation effects on the experimental wells.

Functional assay data collection and analysis

Raw experimental data were collected using MARS data analysis software (BMG Labtech, Offenburg, Germany) and processed in GraphPad Prism 10. The primary metric, the BRET ratio, was calculated to quantify ligand activity and was determined using the following equation:

$$BRET\ ratio = \frac{acceptor\ (Venus - mG\ or\ Venus - \beta arr2) at\ 535nm}{donor\ (Luciferase) at\ 475nm}$$

The results are fitted into a sigmoidal dose response curve using:

$$Y = Bottom + \frac{Top - Bottom}{1 + 10^{LogEC50 - X}}$$

Statistical comparisons across groups were performed using ordinary one-way ANOVA in GraphPad Prism 10. A p value of less that 0.05 ($p < 0.05$) was considered significantly different.

Chapter Three: Results

In silico findings

Ensemble semi-flexible molecular docking reveals key binding poses.

To construct a dataset of currently known GPR55 binders, we searched multiple open-access repositories, including GPCRdb, ChEMBL, DrugBank, the Guide to Pharmacology, and ZINC. The curated database of GPR55 ligands, with assigned pharmacological action where available, comprised a total of 563 compounds: 293 antagonists, 175 agonists, and 95 binders with unassigned activity.

To investigate which receptor residues are key to ligand binding and how they may contribute to agonism or antagonism, we performed molecular docking of all ligands in the curated dataset using the open-source AutoDock Vina software. For simplicity, Autodock Vina uses a semi-flexible docking approach, where the receptor is treated as rigid and the ligand as flexible. However, in nature, both the receptor and ligand are dynamic, while a rigid receptor model represents a single static conformation. To account for this, ensemble docking was performed using multiple GPR55 structures, the AlphaFold active-state model (UniProt: Q9Y2T6), the LPI-bound GPR55-G_{13} complex (PDB: 8ZX4), the AM251-bound GPR55-G_{13} complex (PDB: 8ZX5), the ligand-free apo GPR55-G_{13} complex (PDB: 9IY8), and the antagonist-bound GPR55-Fab-Nb-ONO-9710531 complex (PDB: 9IYA).

During molecular docking, AutoDock Vina predicts ligand-receptor binding by exhaustively sampling possible ligand conformations and orientations within a predefined docking grid. Each binding pose is ranked, with mode 1 representing the most favourable pose with the lowest (most negative) estimated free energy of binding, and mode 10 representing the least favourable. In addition to binding affinity, AutoDock Vina reports the root mean square deviation (RMSD) from both the upper and lower bounds, which accounts for symmetry when calculating the difference between each pose and the top-ranked pose (mode 1) (***Figure 1*A**). For each receptor-ligand pair, up to ten binding poses were generated, producing ~26 000 poses, ~5 000 poses for each receptor. We retained multiple poses for analysis because an energetically plausible interaction is not necessarily structurally realistic *in vitro*. We rationalised that if the dataset is sufficiently large, the most functionally relevant atomic interactions between each ligand and its receptor are expected to be overrepresented across poses, even in the presence of noise from irrelevant binding modes.

Calculating AIFs from key docking poses

Each ligand binding pose was used to generate an AIF using Arpeggio software. In total, ~26000 AIF files were obtained. These AIFs encode all atomic interactions between GPR55 and each ligand binding pose (***Figure 1*B**). To prepare the data for machine learning analysis, the AIF files were parsed and converted into binary interaction matrices, where rows correspond to individual ligand poses and columns correspond to specific receptor-ligand atomic interactions. A value of 1 indicated the presence of a given interaction in that pose, while 0 indicated its absence. To explore the effect of identifier granularity on the resulting data, four different levels of truncation were tested for ligand and receptor IDs. The matrices produced under all four schemes were comparable in size, resulting in a standardised representation of ligand-receptor contacts for K-means clustering and machine learning analysis. K-means clustering was applied to the binary interaction matrices to explore whether ligand poses would group according to similar binding modes. To determine the optimal number of clusters, the WCSS was calculated for all ligand poses, and an elbow plot was

generated (***Figure 1*C**). However, no clear elbow was observed, likely due to the high structural similarity among ligand poses within the same orthosteric binding site. To further investigate potential structural differences, clustering was also performed with k=2, forcing the dataset into two clusters where cluster 0 was the ligands classed as antagonists and cluster 1 those classed as agonists. The resulting clusters were subsequently inspected in PyMOL to confirm that all poses remained within the predefined docking grid and to assess any differences in the binding locations of each ligand pose (***Figure 1*D)**.

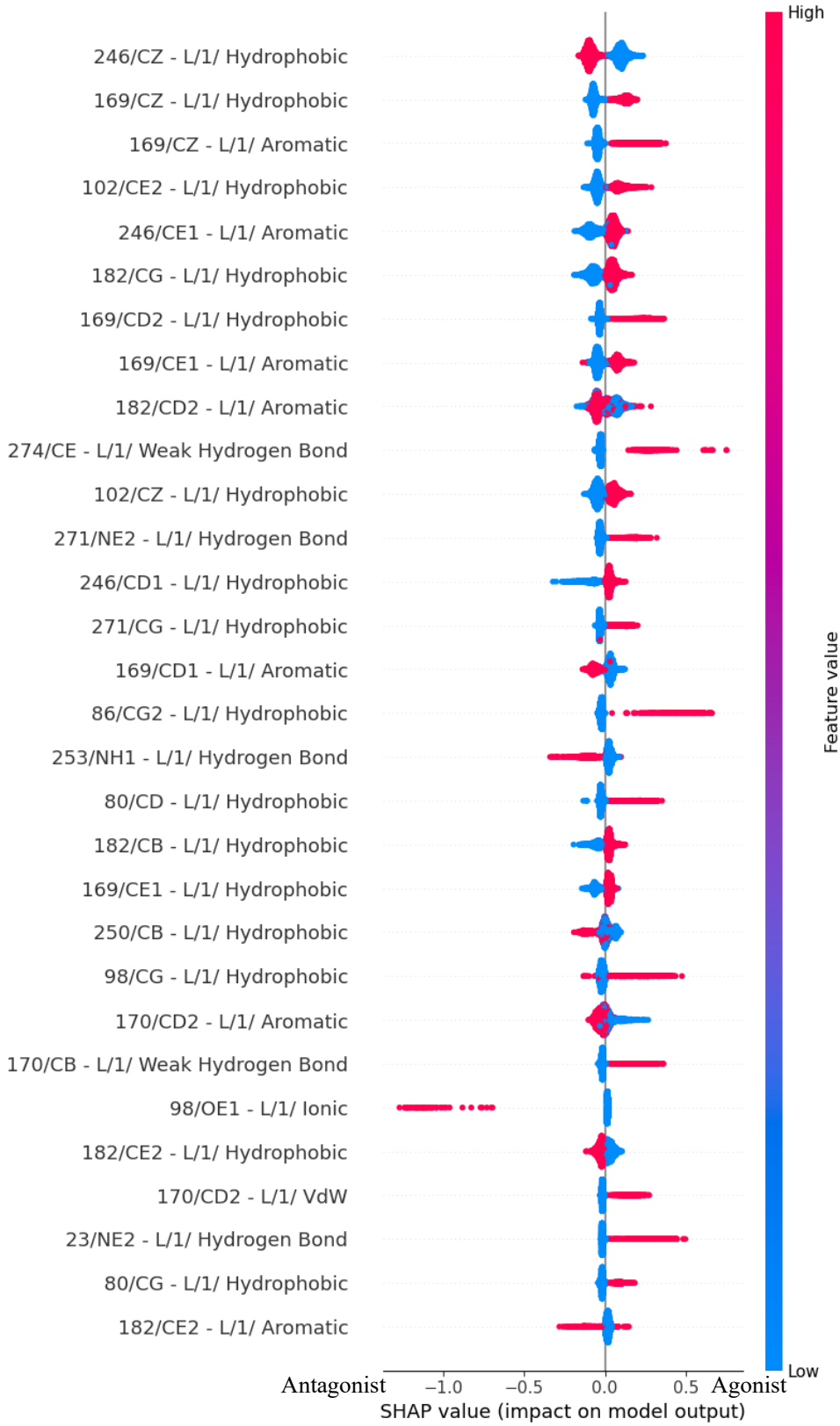
Machine learning identification of key binding residues

After confirming through visual inspection that all docked ligands were located within the predicted orthosteric binding pocket, we trained CatBoost classifiers to predict key receptor-ligand interactions associated with agonism or antagonism. To interpret the model's results, SHAP analysis was performed for each receptor structure at four levels of recptor-ligand interaction granularity, yielding a total of 20 beeswarm plots.

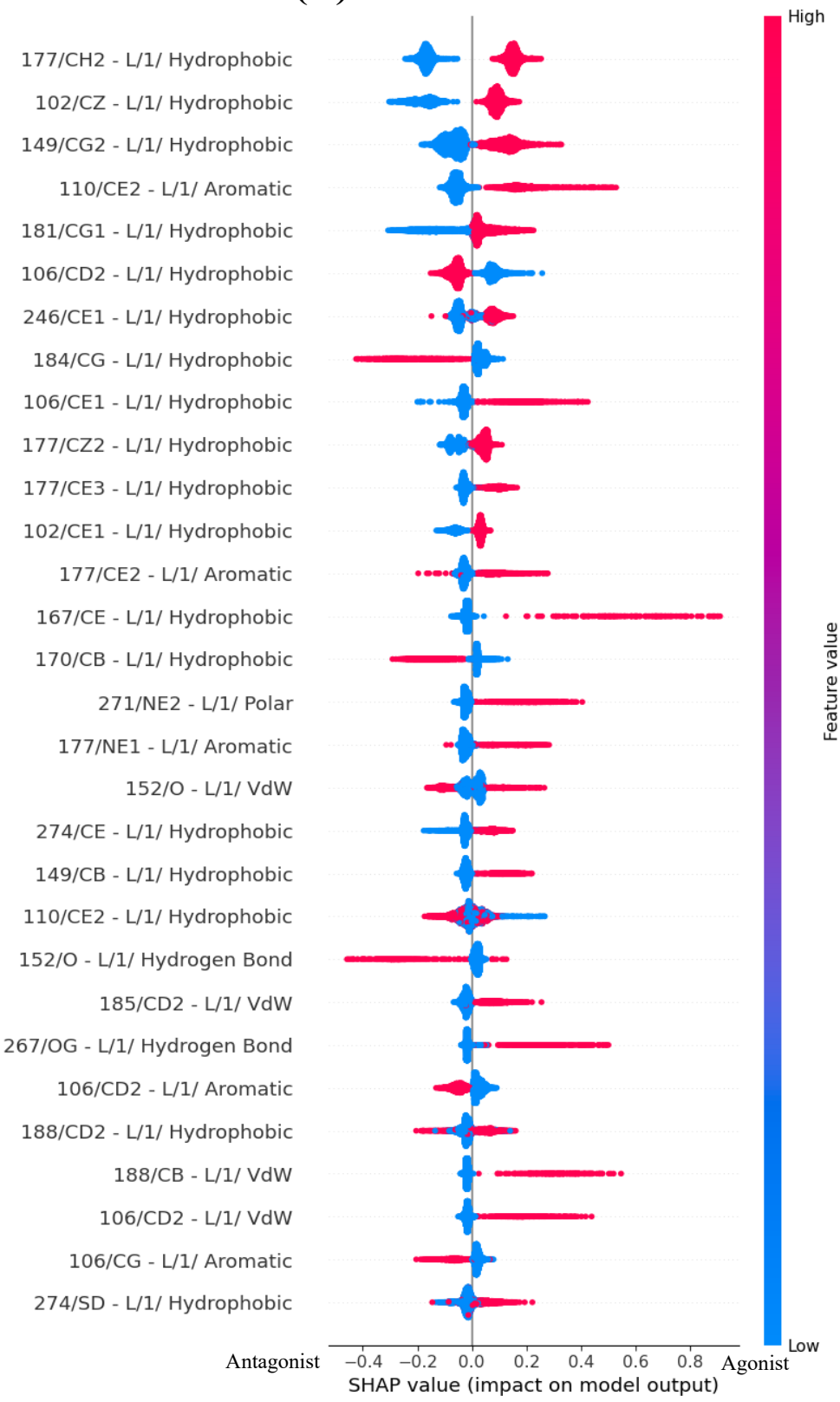
Beeswarm plots (***Figure 5***) visualise. The contribution of individual receptor- ligand pose interaction, with its position on the x-axis corresponding to SHAP value. Positive SHAP values indicate that the interaction contributes to predicting agonism, while negative values indicate a contribution to predicting antagonism. The colour of the points denotes whether the interaction is present (red) or absent (blue) in a given receptor-ligand pose pair. Importantly, features in the beeswarm plots are ordered from top to bottom according to their overall importance across the dataset, measured as the mean absolute SHAP value for each interaction. Thus, the top-ranked interactions are those that exerted the greatest influence on distinguishing agonists from antagonists, while features lower in the ranking had a weaker effect.

To further simplify interpretation, each SHAP plot was manually inspected, and interactions were scored according to the magnitude of their SHAP values: up to ±0.25 = ±1, up to ±0.5 = ±2, up to ±0.75 = ±3, and up to ±1.0 = ±4. For each receptor structure, the cumulative score of each residue was calculated by summing across all granularity levels. These residue scores were then combined across all receptor structures, and the highest-scoring residues ($W177^{ECL2}$, $P155^{4.59x60}$, $M167^{ECL2}$, $Q271^{7.36x35}$, $F102^{3.33x33}$, $V149^{4.53x53}$, $M274^{7.39x38}$, $F246^{6.55x55}$, $M172^{ECL2}$, $L270^{7.35x34}$, $I156^{4.60x61}$) were identified as potentially key contributors to GPR55 ligand binding (***Figure 6***).

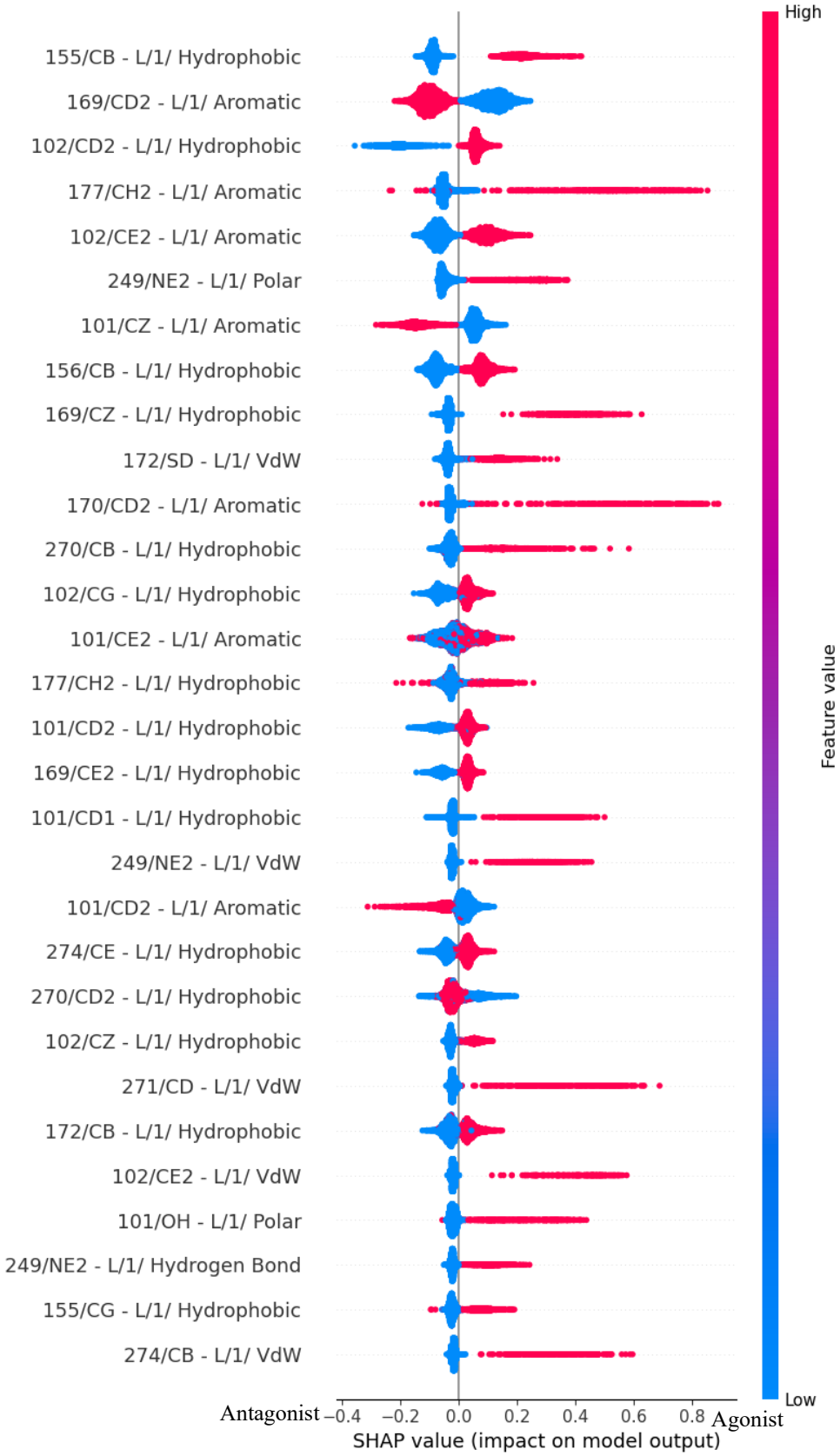
(A) UniProt: Q9Y2T6



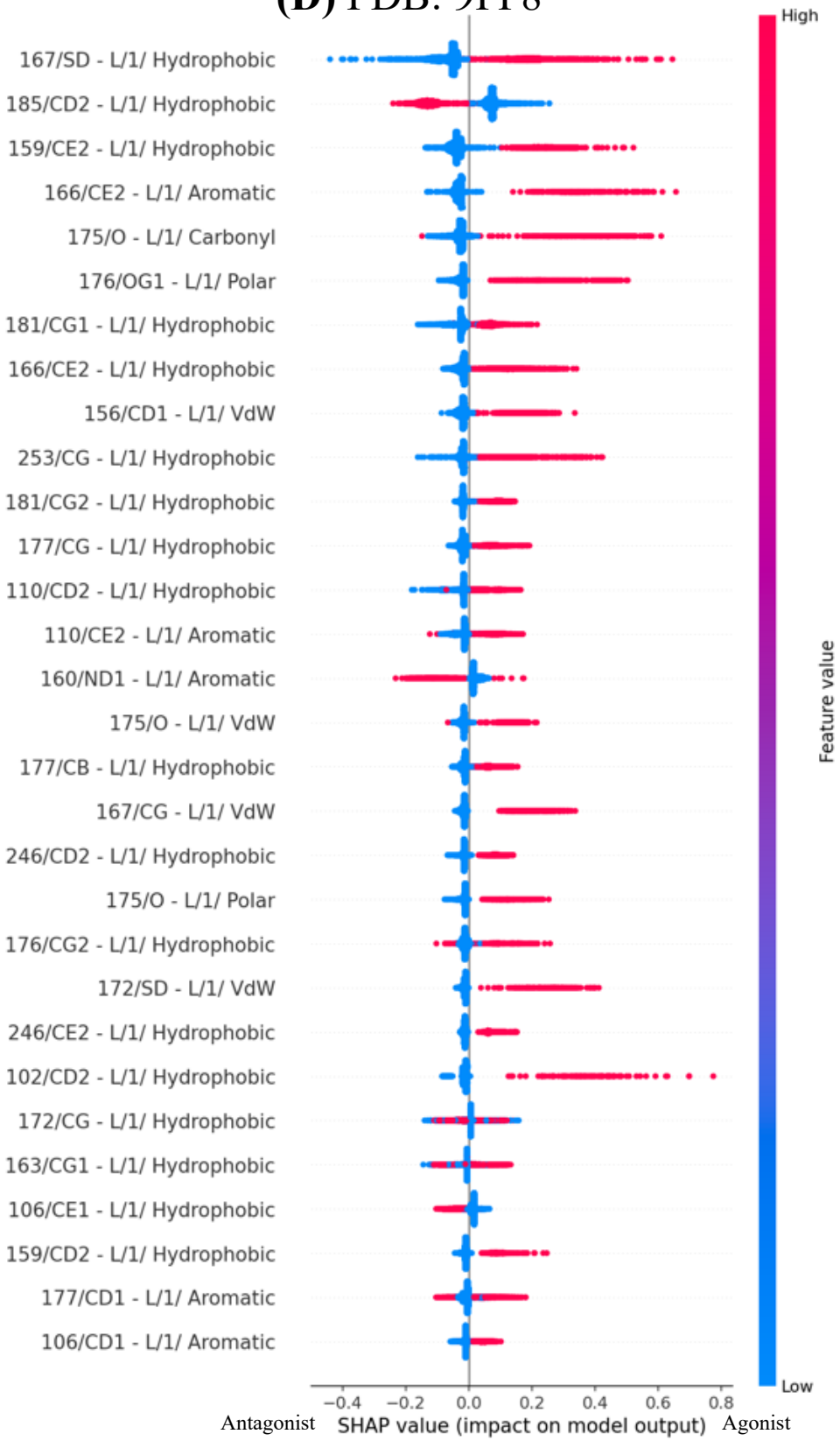
(B) PDB: 8ZX4


177/CH2 - L/1/ Hydrophobic
102/CZ - L/1/ Hydrophobic
149/CG2 - L/1/ Hydrophobic
110/CE2 - L/1/ Aromatic
181/CG1 - L/1/ Hydrophobic
106/CD2 - L/1/ Hydrophobic
246/CE1 - L/1/ Hydrophobic
184/CG - L/1/ Hydrophobic
106/CE1 - L/1/ Hydrophobic
177/CZ2 - L/1/ Hydrophobic
177/CE3 - L/1/ Hydrophobic
102/CE1 - L/1/ Hydrophobic
177/CE2 - L/1/ Aromatic
167/CE - L/1/ Hydrophobic
170/CB - L/1/ Hydrophobic
271/NE2 - L/1/ Polar
177/NE1 - L/1/ Aromatic
152/O - L/1/ VdW
274/CE - L/1/ Hydrophobic
149/CB - L/1/ Hydrophobic
110/CE2 - L/1/ Hydrophobic
152/O - L/1/ Hydrogen Bond
185/CD2 - L/1/ VdW
267/OG - L/1/ Hydrogen Bond
106/CD2 - L/1/ Aromatic
188/CD2 - L/1/ Hydrophobic
188/CB - L/1/ VdW
106/CD2 - L/1/ VdW
106/CG - L/1/ Aromatic
274/SD - L/1/ Hydrophobic
High
Feature value
Low
Antagonist
−0.4
−0.2
0.0
0.2
0.4
0.6
0.8
Agonist
SHAP value (impact on model output)

(C) PDB: 8ZX5


155/CB - L/1/ Hydrophobic
169/CD2 - L/1/ Aromatic
102/CD2 - L/1/ Hydrophobic
177/CH2 - L/1/ Aromatic
102/CE2 - L/1/ Aromatic
249/NE2 - L/1/ Polar
101/CZ - L/1/ Aromatic
156/CB - L/1/ Hydrophobic
169/CZ - L/1/ Hydrophobic
172/SD - L/1/ VdW
170/CD2 - L/1/ Aromatic
270/CB - L/1/ Hydrophobic
102/CG - L/1/ Hydrophobic
101/CE2 - L/1/ Aromatic
177/CH2 - L/1/ Hydrophobic
101/CD2 - L/1/ Hydrophobic
169/CE2 - L/1/ Hydrophobic
101/CD1 - L/1/ Hydrophobic
249/NE2 - L/1/ VdW
101/CD2 - L/1/ Aromatic
274/CE - L/1/ Hydrophobic
270/CD2 - L/1/ Hydrophobic
102/CZ - L/1/ Hydrophobic
271/CD - L/1/ VdW
172/CB - L/1/ Hydrophobic
102/CE2 - L/1/ VdW
101/OH - L/1/ Polar
249/NE2 - L/1/ Hydrogen Bond
155/CG - L/1/ Hydrophobic
274/CB - L/1/ VdW
High
Feature value
Low
Antagonist
−0.4
−0.2
0.0
0.2
0.4
0.6
0.8
Agonist
SHAP value (impact on model output)

(D) PDB: 9IY8


167/SD - L/1/ Hydrophobic
185/CD2 - L/1/ Hydrophobic
159/CE2 - L/1/ Hydrophobic
166/CE2 - L/1/ Aromatic
175/O - L/1/ Carbonyl
176/OG1 - L/1/ Polar
181/CG1 - L/1/ Hydrophobic
166/CE2 - L/1/ Hydrophobic
156/CD1 - L/1/ VdW
253/CG - L/1/ Hydrophobic
181/CG2 - L/1/ Hydrophobic
177/CG - L/1/ Hydrophobic
110/CD2 - L/1/ Hydrophobic
110/CE2 - L/1/ Aromatic
160/ND1 - L/1/ Aromatic
175/O - L/1/ VdW
177/CB - L/1/ Hydrophobic
167/CG - L/1/ VdW
246/CD2 - L/1/ Hydrophobic
175/O - L/1/ Polar
176/CG2 - L/1/ Hydrophobic
172/SD - L/1/ VdW
246/CE2 - L/1/ Hydrophobic
102/CD2 - L/1/ Hydrophobic
172/CG - L/1/ Hydrophobic
163/CG1 - L/1/ Hydrophobic
106/CE1 - L/1/ Hydrophobic
159/CD2 - L/1/ Hydrophobic
177/CD1 - L/1/ Aromatic
106/CD1 - L/1/ Aromatic
−0.4
−0.2
0.0
0.2
0.4
0.6
0.8
Antagonist
SHAP value (impact on model output)
Agonist
High
Feature value
Low

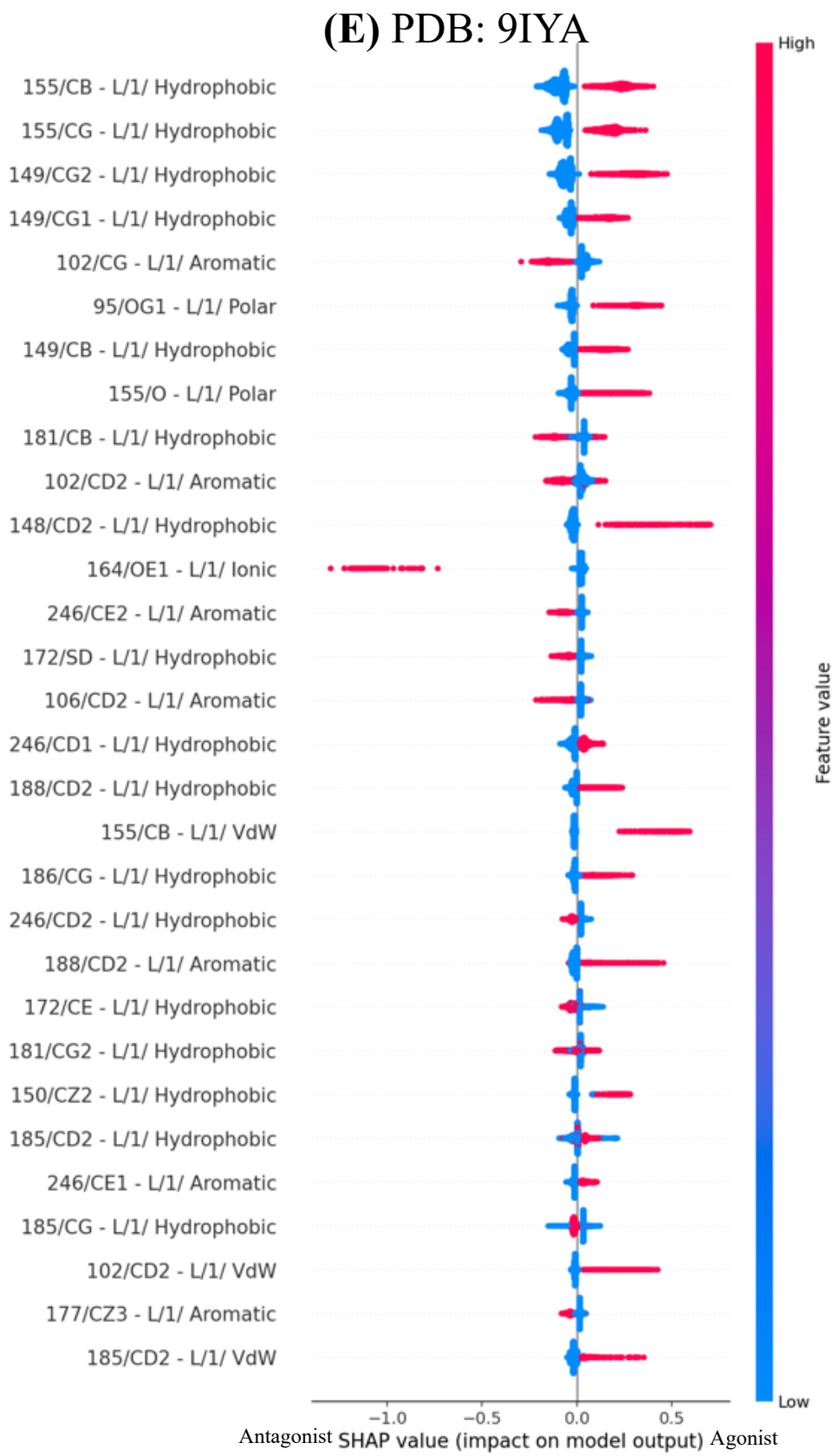


Figure 5. SHAP analysis of receptor-ligand interactions across GPR55 structural states. Beeswarm plots of SHAP (Shapley Additive exPlanations) values are shown for five GPR55 structures: (**A**) the AlphaFold active-state model (UniProt: Q9Y2T6), (**B**) the LPI-bound

GPR55-G_{13} complex (PDB: 8ZX4), (**C**) the AM251-bound GPR55-G_{13} complex (PDB: 8ZX5), (D) the apo GPR55-G_{13} complex (PDB: 9IY8), and (**E**) the antagonist-bound GPR55-Fab-Nb-ONO-9710531 complex (PDB: 9IYA). SHAP values were calculated using the CatBoost machine learning method. Each dot represents a receptor-ligand pose interaction, and the position along the x-axis reflects the impact of that feature on classification, where positive SHAP values increase the likelihood of agonist assignment, while negative SHAP values increase the likelihood of antagonist assignment. Colour indicates the presence (red) or absence (blue) of the specific atomic interaction. The plots highlight the 20 features with the highest impact on interatomic interactions for each structure.

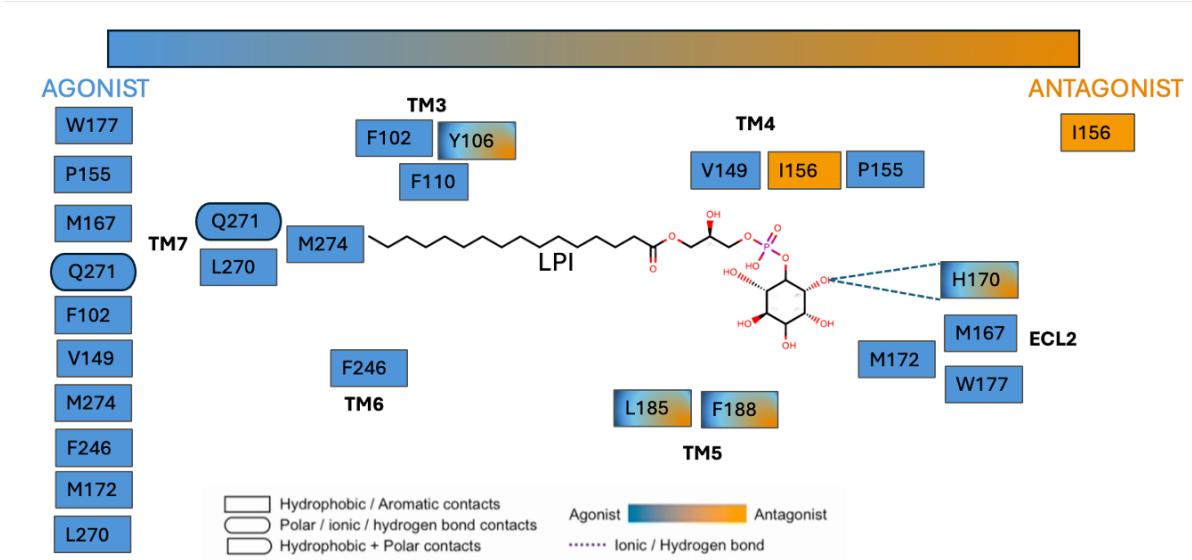


Figure 6. **2D schematic of the predicted GPR55 ligand-binding pocket.**
Schematic representation of the top 16 recurring residues predicted to contribute to GPR55 ligand binding, based on SHAP value analysis from a CatBoost machine learning model. Residues are labelled by single-letter amino acid code and protein position, with their corresponding transmembrane helix or extracellular loop indicated. Interaction types are shown as rectangles for hydrophobic and aromatic contacts, ovals for polar, ionic, and hydrogen-bond interactions, and combined shapes for residues predicted to participate in multiple interaction types. Blue indicates residues predicted to interact with agonists, and orange residues predicted to interact with antagonists. Blue dotted lines highlight a predicted interaction between the hydrophilic head of the endogenous ligand lysophosphatidylinositol (LPI) and a histidine residue in the binding pocket.

Model performance and classification accuracy

To evaluate the predictive power of the contact data for ligand classification, a support vector machine (SVM) classifier was also trained on the same 80:20 train-test split. The classification performance of for each receptor model was quantified using confusion matrices (***Figure 7*** **A-E**) and summarised by the Matthews Correlation Coefficient (MCC) values shown in ***Table 2.*** The MCC values are all positive values between 0.25 and 0.39 meaning the classifier performs better than random. The MCC values decrease from the experimentally resolved cryo-EM structures to the AlphaFold model. The AlphaFold model also has high false negative counts suggesting the classifier struggles to identify positives in this case. The type of bound ligand or absence thereof also seems to affect predictive

performance, suggesting that ligand-induced conformational changes influence classification accuracy.

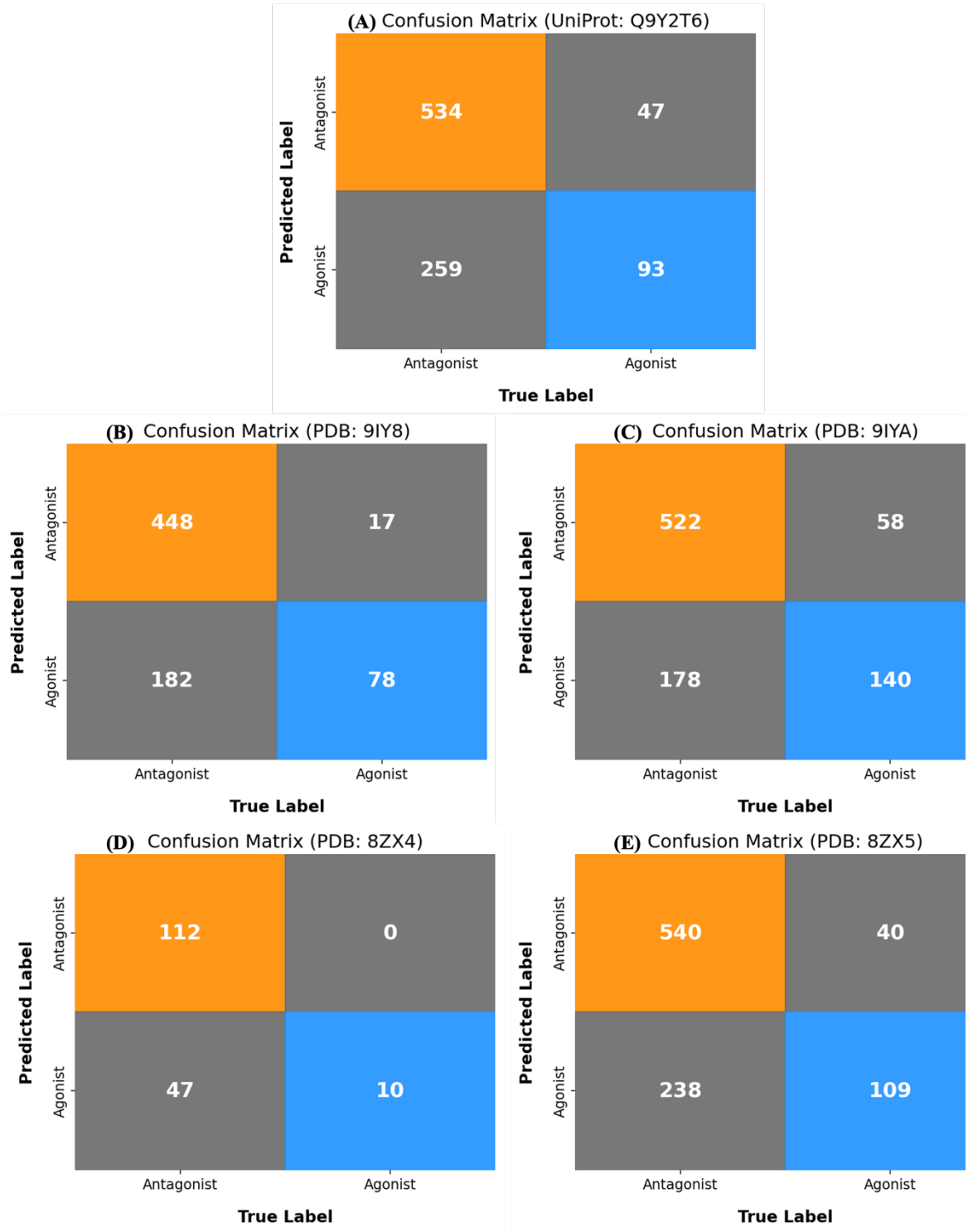


Figure 7. **Confusion Matrices for SVM- based ligand activity predictions**
Confusion matrices illustrating the performance of the support vector machine (SVM) classifier in predicting ligand agonist or antagonist activity based on atomic interaction fingerprints. Each matrix represents the classification outcome for **(A)** the AlphaFold active-state model (UniProt: Q9Y2T6); **(B)** The ligand-free apo GPR55-G_{13} complex (PDB: 9IY8); **(C)** The antagonist-bound GPR55-Fab-Nb-ONO-9710531 complex (PDB:

9IYA); **(D)** The LPI-bound GPR55-G_{13} complex (PDB: 8ZX4); and **(E)** The AM251-bound GPR55-G_{13} complex (PDB: 8ZX5). The 'True Label' on the x-axis indicates the actual pharmacological activity while the 'Predicted Label' on the y-axis shows the model's classification. The numbers in each quadrant are the count of ligand poses classified in that category. The correct predictions are highlighted in colour. Orange (top-left) indicates true negatives (correctly predicted antagonists), and blue (bottom-right) indicates true positives (correctly predicted agonists). Misclassifications are shown in grey, with false positives on the top right and false negatives on the bottom left.

Table 2. **Classification performance of the SVM models for predicting ligand activity.** Summary of the model performance matrices for the SVM classifier trained on atomic interaction fingerprints derived from four GPR55 cryo-EM structures and one AlphaFold model structure. The table shows the true negatives (TN), false positives (FP), false negatives (FN), true positives (TP), and the resulting Matthews Correlation Coefficient (MCC) values.

Receptor Structure	*TN*	*FP*	*FN*	*TP*	*MCC*
9IYA *(Antagonist-bound)*	522	58	178	140	0.39
9IY8 *(Apo, Ligand-free)*	448	17	182	78	0.37
8ZX4 *(LPI-bound)*	112	0	47	10	0.35
8ZX5 *(AM251-bound)*	540	40	238	109	0.31
Q9Y2T6 *(AlphaFold model)*	534	47	259	93	0.25

Individual docking analysis shows atomic differences of ligand binding.

In addition to the SHAP analysis, we individually docked the ten compounds used in the *in vitro* experiments to examine their interactions with the predicted GPR55 binding pocket. This approach provided a more granular, residue-level view of the molecular interactions. ***Figure 8*** shows that the mapped out binding pocket is made up of predominantly hydrophobic residues, which is consistent with the lipid-like nature of GPR55 ligands and the endogenous ligand, LPI. The only polar residue identified within the pocket is $Q271^{7.36x35}$. The binding pocket itself is relatively shallow, with only CBD, LPI, ML184, and THC extending deeper to interact with $V149^{4.53x53}$, whereas the remaining ligands remained closer to the extracellular surface. This allows the ligands to interact with the second extracellular loop (ECL2) residues like $W177^{ECL2}$ and $M167^{ECL2}$, which could potentially have a role in gating or stabilising ligand binding. Additionally, all the ligands interact with the residues $W177^{ECL2}$, $F102^{3.33x33}$, and $F246^{6.55x55}$, suggesting that these aromatic residues may act as molecular switches for receptor activation.

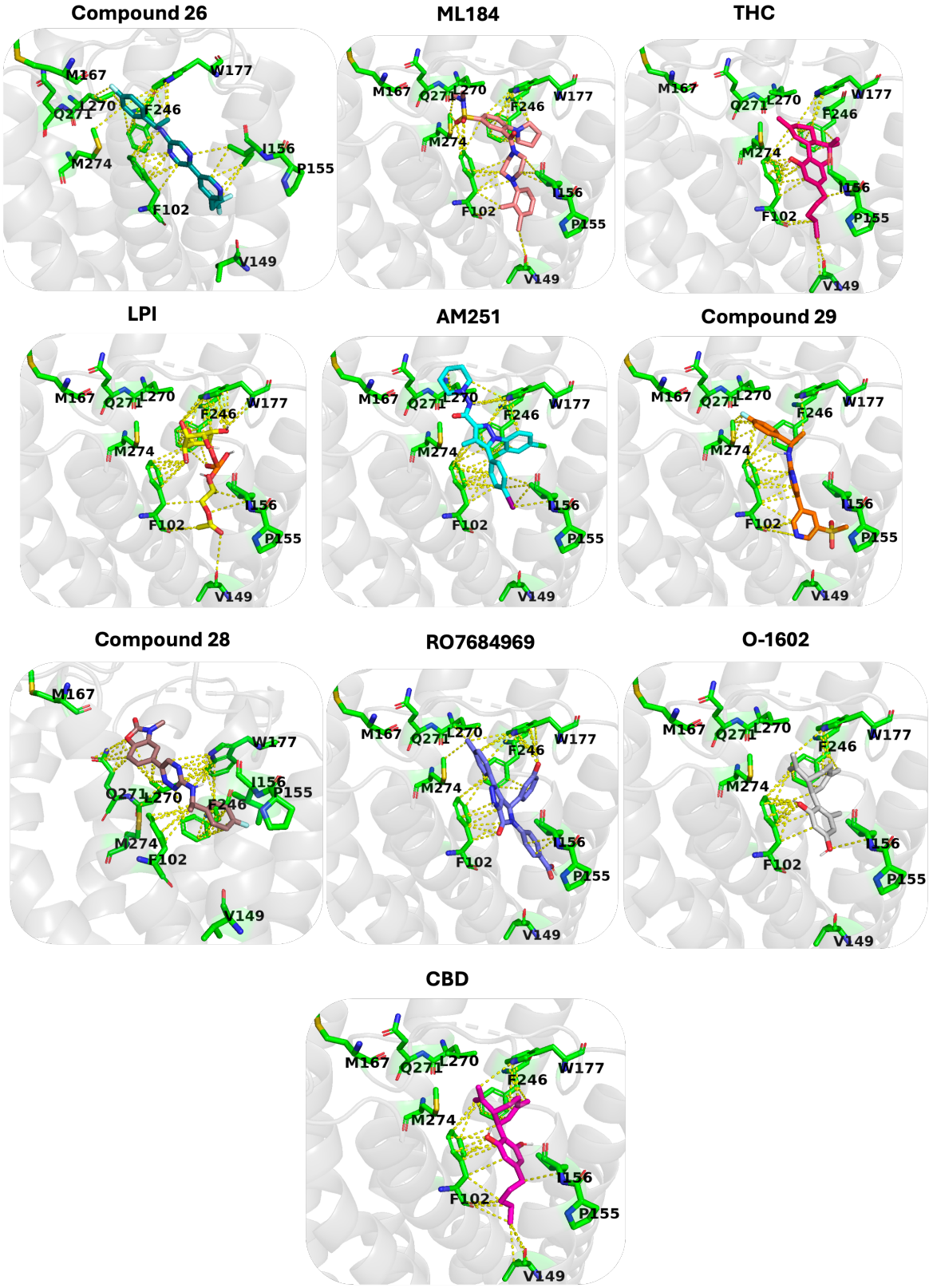


Figure 8. **Computational mapping of GPR55 ligand-binding residues and docked ligand poses.**

The predicted GPR55 binding site, identified using CatBoost machine learning, is mapped within the GPR55-G_{13} complex (PDB: 9GE2) in PyMOL. The predicted binding site residues W177, P155, M167, Q271, F102, V149, M274, F246, M172, L270, and I156 are

shown as labelled sticks. Each ligand is displayed as its highest-scoring docking pose generated with AutoDock Vina, of compounds 26, ML184, THC, LPI, AM251, compounds 28 and 29, R07684969, O-1602, and CBD. Yellow dashed lines indicate predicted interactions between residues and ligands occurring within 4 Å, highlighting potential points of contact within the binding pocket.

In vitro assay findings

While these computational predictions offer mechanistic insights into the binding patterns of ligands to GPR55, it is important to note that the training dataset may contain classification errors due to variability in reported ligand activities across different assay systems. Consequently, the predictions generated by the model are not expected to be perfectly accurate, and therefore, need to be coupled with experimental validation.

The cell-based BRET β-arrestin recruitment assay.

To establish our assay systems, we first tested ligands reported to have high affinity for GPR55 in the literature. We used ML184, a potent ligand with reported activity of 250 nM (Kotsikorou *et al.*, 2011), as a reference compound to confirm that the assay functioned reliably in our hands. We also obtained compound 26 (Hewer *et al.*, 2023), a more potent ligand with an EC_{50} of 6.2 nM, which served as an additional benchmark. Both ligands were originally identified through high-throughput, cell-based β-arrestin recruitment assays, making them an appropriate starting point for validating our system. In addition to these reference ligands, we also tested the endogenous ligand LPI and a panel of other high-potency compounds available to us, including AM251, O-1602, THC, compound 28, compound 29 (Hewer *et al.*, 2023), and RO7684969. We also included the antagonist ligand, CBD.

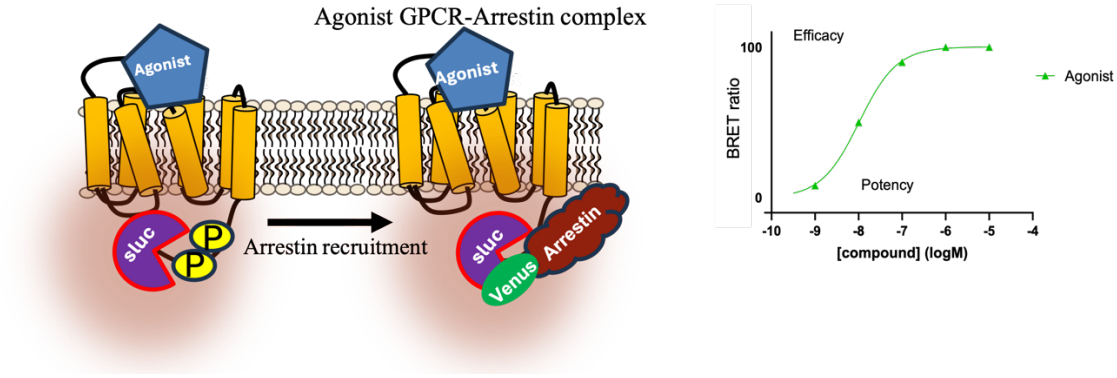


Figure 9. **The BRET-based β-arrestin2 recruitment assay.**
This assay measures the recruitment of β-arrestin2 to GPCRs upon ligand activation. The thermostable luciferase (sLuc) enzyme is fused to the C-terminal tail of the receptor, while the fluorescent protein Venus is fused to β-arrestin2. Upon receptor activation and phosphorylation, β-arrestin2 is recruited to the GPCR, bringing Venus into close proximity with sLuc. In the presence of the sLuc substrate furimazine, bioluminescence resonance

energy transfer (BRET) occurs. Receptor activation is measured by the increase in BRET ratio.

Unlike Hewer *et al.* (2023) that used the PathHunter β-arrestin assay (DiscoverX), a commercially available enzyme fragment complementation system and Kotsikorou *et al.* (2011) that used the β-arrestin2-GFP redistribution assay, we used the bioluminescence resonance energy transfer (BRET)-based techniques. BRET relies on energy transfer from a luciferase enzyme reaction (donor) to a nearby fluorescent protein (acceptor). In our assay, the donor sLuc enzyme is fused to the C-terminus of GPR55, and the acceptor Venus is fused to β-arrestin2 ***(Figure 9)***. When an agonist binds to GPR55, the receptor is phosphorylated and recruits Venus-tagged β-arrestin2, bringing the donor and acceptor into close proximity (typically within ~10 nm), resulting in fluorescence emission measured as the BRET ratio.

Linker length does not influence β-Arrestin recruitment in GPR55-sLuc constructs.

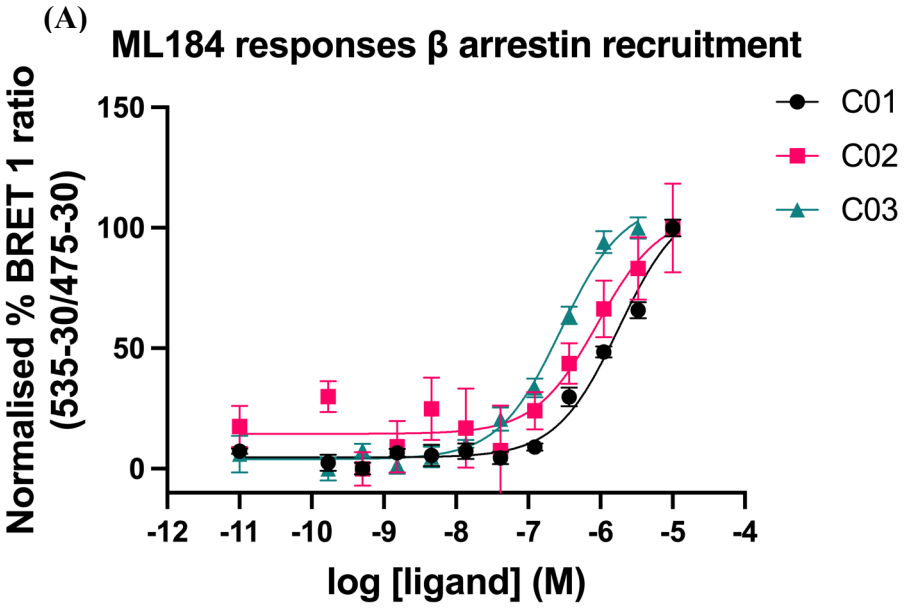
Since GPR55 has a relatively short C-terminus (13 amino acids), we generated three GPR55-sLuc constructs with different linker lengths to test whether sLuc-venus proximity affected BRET signals. C01_ pcDNA4TO _TS_GPR55-sLuc with a short GSGS linker, C02_ pcDNA4TO _TS _GPR55- CB2(340–360)-sLuc with 20 amino acids from CB2 receptor as a linker and C03_pcDNA4TO_TS_GPR55-β_2AR (413-393)-sLuc with 20 amino acids from β_2AR as a linker ***(Figure 3).*** Each construct was transfected into Venus-β-arrestin2 expressing HEKT-Rex™-293 cells, and stable cell lines were generated using zeocin selection. Cells were plated at 50,000 cells per well in 96-well Cellstar plates and grown for 48 hours to ~90% confluency, then induced with 1 µg/mL tetracycline for an additional 48 hours. The assay was performed using a buffer containing 10 mM HEPES, 0.1% BSA in HBSS, with 10 µM furimazine.

To assess the effect of the linker on assay performance, β-arrestin recruitment was measured using ML184 across the three constructs ***(Figure 10*****A*****)***. A one-way ANOVA revealed no significant differences in EC_{50} values among the three GPR55 constructs ($p = 0.7075$), indicating that linker length did not influence assay potency with ML184. The assay windows (span) were also comparable across constructs, further supporting that all three linkers produced comparable assay performance ***(Figure 10*****B*****)***.

BRET-Based β-arrestin assay reveals reduced potency of GPR55 ligands.

We then ran the β-arrestin recruitment assay on the C01 construct using our selection of ligands, ML184, compound 26, compound 28, compound 29, RO7684969, LPI, AM251, O-1602, THC and CBD in triplicate ***(Figure 11)***. For ML184, we obtained a pEC_{50} of 6.26 ± 0.03 (SEM, n = 3), corresponding to an EC_{50} of 555 nM, which was ~2.2-fold lower in potency than the reported 250 nM. For compound 26, we obtained a pEC_{50} of 8.04 ± 0.03 (sem, n = 3), corresponding to an EC_{50} of 9.2 nM, representing a ~1.5-fold decrease in potency compared to the reported EC_{50} of 6.2 nM. So, while our assay reproduced ligand activity profiles, it consistently reported slightly reduced potencies relative to published values. Interestingly, THC, which is reported in the literature as a GPR55 agonist (Lauckner *et al.*, 2008), did not elicit detectable β-arrestin recruitment in our system.

(A)



(B)

Construct	C01	C02	C03
pEC$_{50}$	5.75 ± 0.06	6.04 ± 0.13	6.55 ± 0.04
Span (%)	107.4	91.6	107.2

Figure 10. **Comparison of ML184-induced β-arrestin recruitment across GPR55 constructs.**

(A) Concentration-response curves showing the effect of the GPR55 agonist ML184 on β-arrestin recruitment in stable HEK293TR Venus-β-arrestin2 cells expressing three GPR55 constructs. Each construct contains the thermostable luciferase (sLuc) fused to the C-terminus of GPR55 via either a flexible GSGS linker (C01, black), a CB2R (residues 340-360) derived linker (C02, pink), or a β2AR (residues 313-393) derived linker (C03, turquoise). The assay was performed in buffer containing HBSS, 10 mM HEPES (pH 7.5), and 0.1% BSA with 10 µM furimazine with ligand concentrations ranging from 0.2 nM to 10 µM (3-fold dilutions). The y-axis represents the BRET ratio normalised to the percentage of maximal response. Curves were fitted using non-linear regression. No significant difference in EC$_{50}$ values was observed among the constructs (one-way ANOVA, $p = 0.7075$).

(B) Corresponding potencies and assay window (span) derived from panel A.

Data are presented as mean ± SEM, n = 3.

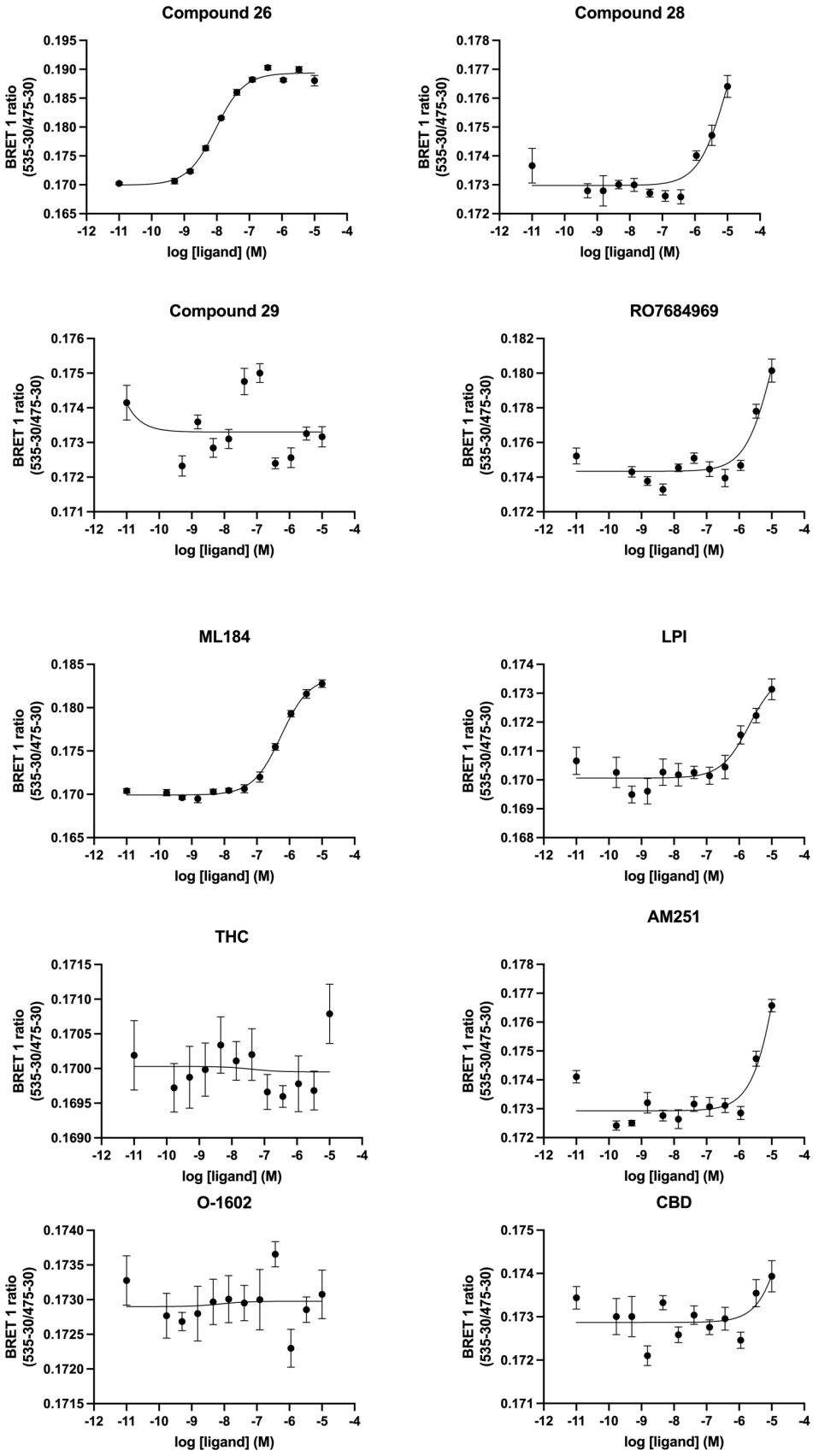


Figure 11. **Cell-based β-arrestin recruitment assays.**
Dose-response curves showing β-arrestin recruitment in stable HEK293TR Venus-β-arrestin2 cells expressing GPR55 (C01 construct with thermostable luciferase (sLuc) fused

to the C-terminus of GPR55 via a flexible GSGS linker) following stimulation with the agonists compound 26, compound 28, compound 29, RO7684969, ML184, LPI, THC, AM251, and O-1602, as well as the antagonist CBD. The assay was performed in buffer containing HBSS, 10 mM HEPES (pH 7.5), and 0.1% BSA with 10 µM furimazine, with ligand concentrations ranging from 0.2 nM to 10 µM (3-fold dilutions). The y-axis represents the raw BRET ratio (535/475 nm), and the x-axis represents log ligand concentration. Data are presented as mean ± SEM, n = 3.

The cell-based BRET G-CASE biosensor.

While the BRET-based β-arrestin recruitment assay allowed us to validate ligand activity at GPR55, it captures one part of the receptor signalling, so it fails to detect the full responses for all ligands, exemplified by THC. To address this, we next used the G-protein tricistronic activity sensor (G-CASE) assay, a widely used method for measuring GPCR pharmacology through G-protein activation (Schihada, Shekhani and Schulte, 2021). In this system, the Gα subunit is tagged at its N-terminus with a NanoLuc donor, and the Gβγ subunit is tagged at the C-terminus of Gβ with a Venus fluorescent acceptor. Upon agonist activation, dissociation of Gα and Gβγ reduces energy transfer between donor and acceptor, observed as a decrease in the BRET signal ***(Figure 12).***

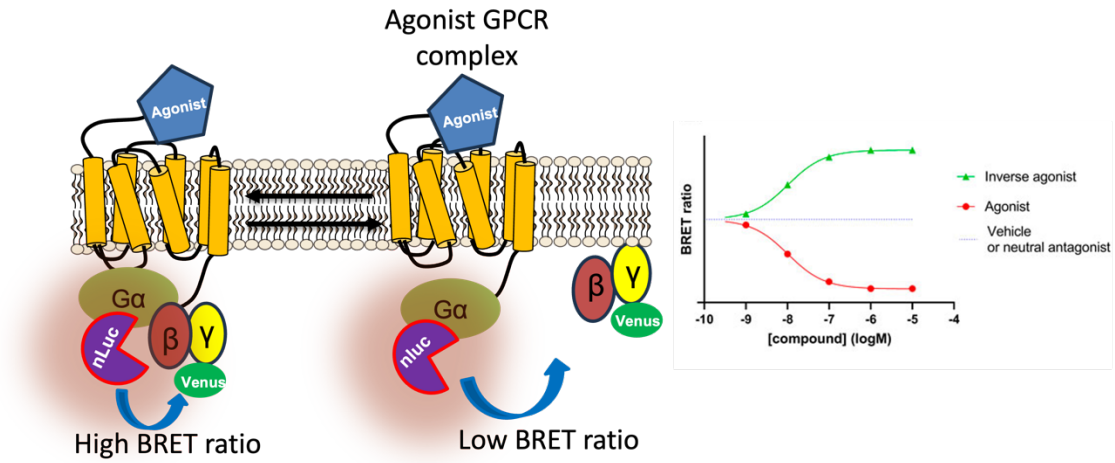


Figure 12. The G-CASE biosensor.
The G-CASE biosensor plasmid encodes a NanoLuciferase enzyme donor fused to the Gα subunit, and a Venus fluorescent acceptor fused to the N-terminus of the Gγ subunit. GPCR activation triggers G protein recruitment, leading to the dissociation of the Gα and Gβγ subunits. This separation increases the distance between the donor and acceptor, resulting in a decrease in the bioluminescence resonance energy transfer (BRET). Receptor activation is measured by the decrease in BRET ratio.

Challenges in measuring GPR55 activity using G-CASE stable cells.

For our first experiments, we recovered and cultured cryopreserved SNAP_GPR55_G_{13}-CASE stable cells generated in previous work. The cells were plated at 50,000 cells per well in 96-well plates, grown for 48 hours, and induced with 1 µg/mL tetracycline for a further 48 h before the assay. The assay was run in 10 mM HEPES, 0.1% BSA in HBSS, with 10 µM furimazine assay buffer, with ligands ML184 and compound 26. From this,

the kinetic traces did not show the expected decrease in BRET signal consistent with Gα-Gβγ dissociation. Instead, the responses were relatively flat, with overlapping curves and no concentration-dependent differences above baseline variation ***(Figure 13A)***.

Given the lack of response, we generated new double-stable cell lines by transfecting stable G_{13}-CASE cells with pcDNA4TO-TS-SNAP_CB2(1-10) _GPR55 and selecting under dual antibiotic pressure (400 µg/mL G-418 sulphate and 20 µg/mL zeocin). These cells were prepared under the same assay conditions. In this case, kinetic curves for ML184 and compound 26 showed some reduction in BRET signal over time, suggesting improved assay performance **(*Figure 13B*)**. However, the curves still overlapped across concentrations, with no clear concentration-dependent effects.

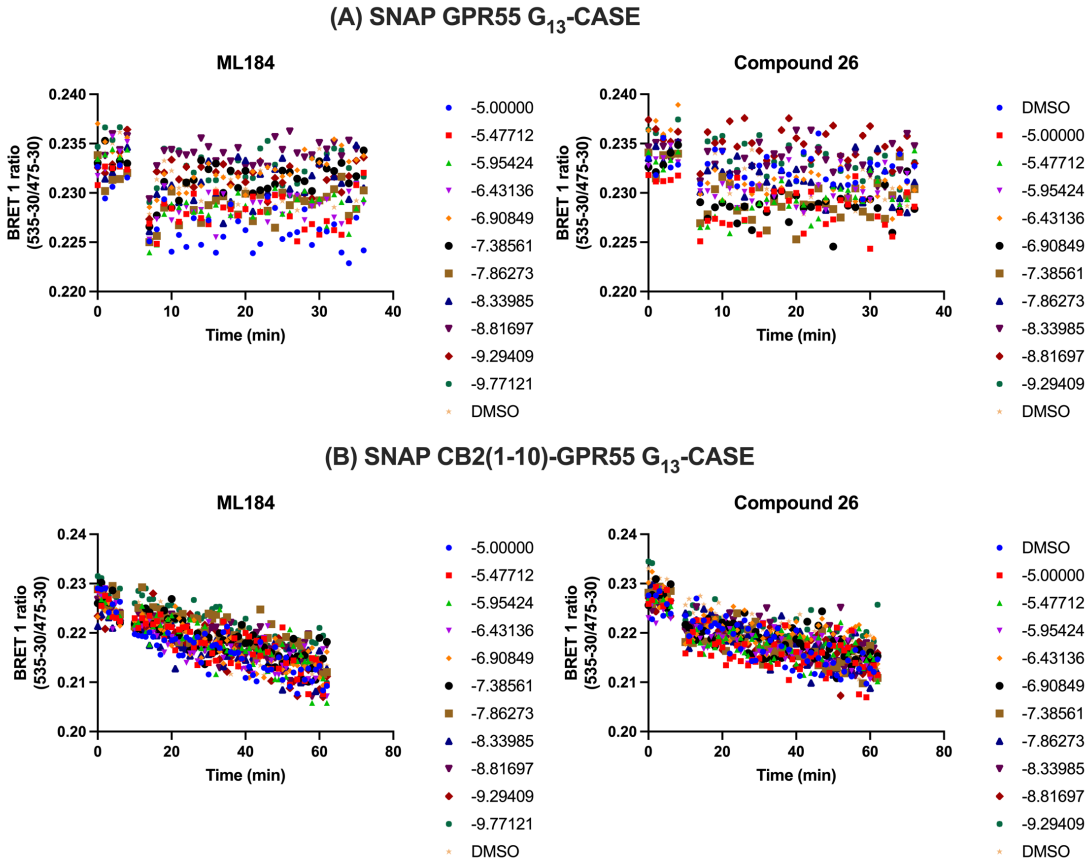


Figure 13. **Cell-based G_{13}-CASE biosensor assays.**
Kinetic BRET traces showing responses of stable HEK293TR cells expressing the SNAP_GPR55_G_{13}-CASE **(A)** and SNAP-CB2R (1-10)-GPR55_G_{13}-CASE **(B)** biosensors following stimulation with the potent GPR55 agonists ML184 (left) and compound 26 (right). The assay was performed in buffer containing HBSS, 10 mM HEPES (pH 7.5), and 0.1% BSA with 10 µM furimazine. Ligands were applied at final concentrations ranging from 0.2 nM to 10 µM (3-fold dilutions), alongside DMSO as a vehicle control, across 12 wells. The y-axis represents the raw BRET ratio (535/475 nm), and the x-axis represents time in minutes after ligand addition.

G-CASE assays shows limited ligand-dependent responses in GPR55.

We hypothesised that the poor performance of the previous G-CASE cells might have been due to their age or degradation of the Venus and Nano luciferase tags, which would impair signal detection. To address this, we generated new stable cell lines. Starting from fresh HEK293TR cells, we transfected plasmids encoding the G_{13}, G_{12}, G_q, and G_i-CASE biosensor and selected the lines with 400 μg/mL G418 sulfate. From these stable cells, we attempted to assess the effects of introducing GPR55 by suspension transient transfection. The cells were plated at 50,000 per well with and without transfection with pcDNA4TO-TS- WT_GPR55. After 48 hours, the transfected cells showed impaired growth compared to the non-transfected G-CASE cells, suggesting that GPR55 overexpression might be toxic for the cells **(*Figure 14*)**. Nonetheless, we generated double-stable lines by transfecting pcDNA4TO-TS-WT_GPR55 into the G-CASE cells, followed by dual selection with 400 μg/mL G-418 sulfate and 20 μg/mL zeocin.

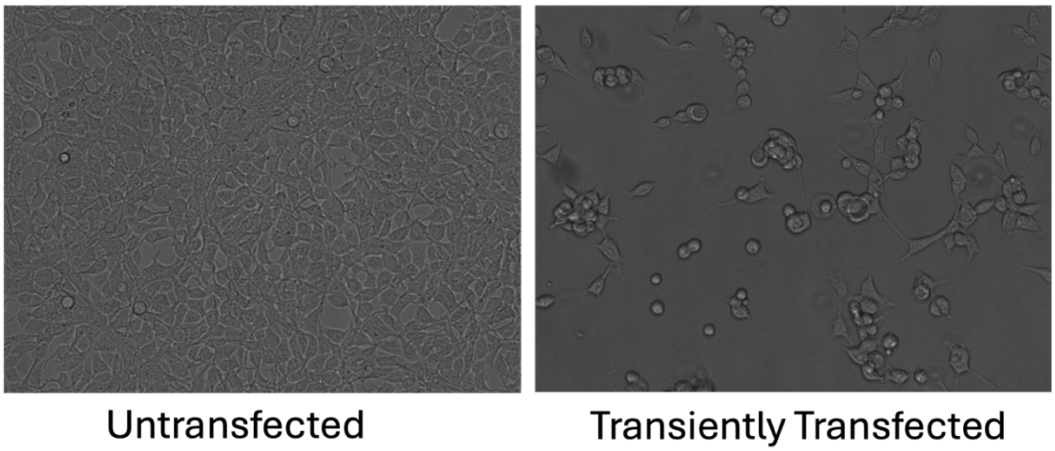


Figure 14. **GPR55 expression negatively affects cell growth in stable G-CASE biosensor cells.**
Representative images captured using the Invitrogen™ Floid™ Cell Imaging Station taken 48hours after plating of HEK293TR cells stably expressing G-protein biosensors. The stable G-CASE cells were plated at 50,000 cells per well and either left untransfected (**left**) or transiently transfected with pcDNA4TO-TS-WT_GPR55 **(right)**. Cells transiently transfected with GPR55 show lower cell density and smaller, less organised clusters.

The stable cells were seeded at 50,000 per well in 96-well CellStar plates, grown for 48 hours, and induced with 1 μg/mL tetracycline for 24 h (reduced from 48 h due to receptor overexpression possibly causing toxicity). Assays were then conducted at 37 °C in buffer containing 10 mM HEPES and 0.1% BSA in HBSS, with 10 μM furimazine, and the BRET ratio was recorded over time following stimulation with ML184 and compound 26. As shown in **(*Figure 14*)**, the G_{13}-CASE traces were highly variable, with substantial noise and overlapping between concentrations, resulting in no clear concentration-dependent decrease in BRET signal. G_{12}-CASE cells exhibited a more consistent gradual decrease in BRET ratio over time, but again without distinct concentration-dependent differences. In contrast, both the G_q-CASE and G_i-CASE biosensors unexpectedly displayed increases in BRET ratio upon ligand addition, an uncharacteristic trend of Gα-Gβγ dissociation in this assay.

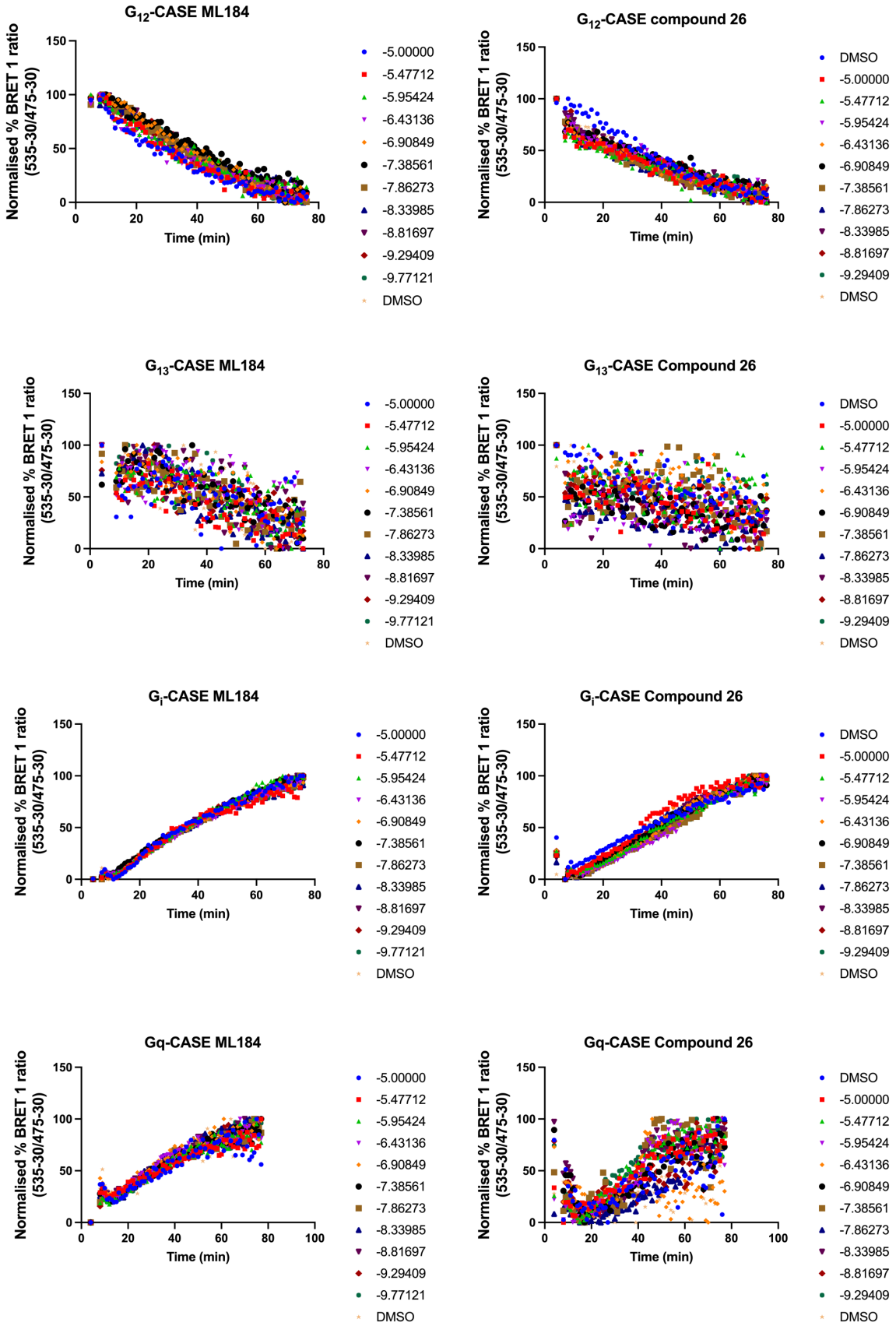


Figure 15. Kinetic BRET responses in stable G-CASE biosensor cell lines.
Stable HEK293TR cells expressing G_{13}, G_{12}, G_q, or G_i-CASE biosensors were seeded at 50,000 cells per well in 96-well plates, grown for 48 h, and induced with 1 µg/mL

tetracycline for 24 h. Prior to ligand addition, cells were pre-incubated for 15 minutes at 37 °C in HBSS containing 10 mM HEPES, 0.1% BSA, and 10 µM furimazine. Cells were then stimulated with the agonists ML184 (left) or compound 26 (right) at a final concentration of 10 µM to 0.2 nM threefold serial dilutions, alongside DMSO as a vehicle control across 12 wells. The y-axis represents the BRET ratio (535/475 nm) normalised to the percentage of maximal response, and the x-axis represents time (minutes) after ligand addition.

The membrane-based mG protein recruitment assay (MeGaBRET)

To address the shortcomings of the cell-based assays, we next developed a membrane-based mG protein recruitment (MeGa-BRET) assay, which captures ligand-driven receptor activation more directly. MeGa-BRET measures ligand-induced recruitment of mG proteins, a single domain from the G protein α-subunit that has been engineered to form a stable complex with GPCRs. In this system, GPR55-sLuc membranes are isolated from Expi293F™ cells, and the vmG protein is purified from bacterial cell cultures. A 50 µL assay mixture is then prepared in a white 384-well OptiPlate containing GPR55-sLuc membranes, vmG protein, assay buffer, and furimazine. Upon ligand stimulation, GPR55 recruitment of the mG protein brings donor and acceptor proteins within ~10 nm, resulting in a detectable increase in BRET signal **(*Figure 2)*.**

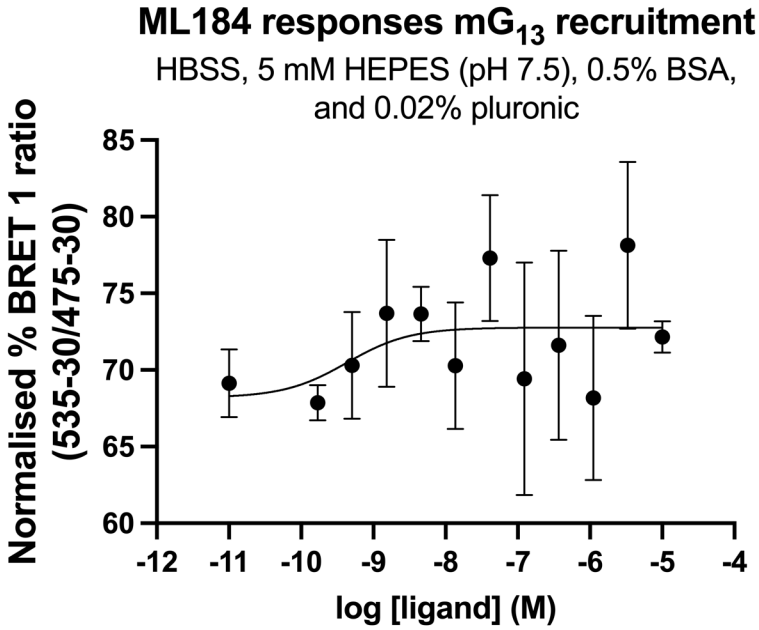


Figure 16. **Recruitment of vmG$_{13}$ protein by GPR55 in response to ML184.**
Dose-response curve showing the vmG$_{13}$ protein (15nM per well) recruitment to GPR55 in the presence of the GPR55 agonist ML184. Assays were performed using 0.33 µg per well of Expi293F™ suspension cell membranes expressing GPR55 in buffer containing HBSS, 5 mM HEPES (pH 7.5), 0.5% BSA, and 0.02% Pluronic F127. ML184 was applied at final concentrations ranging from 10 µM to 0.2 nM using threefold serial dilutions, with

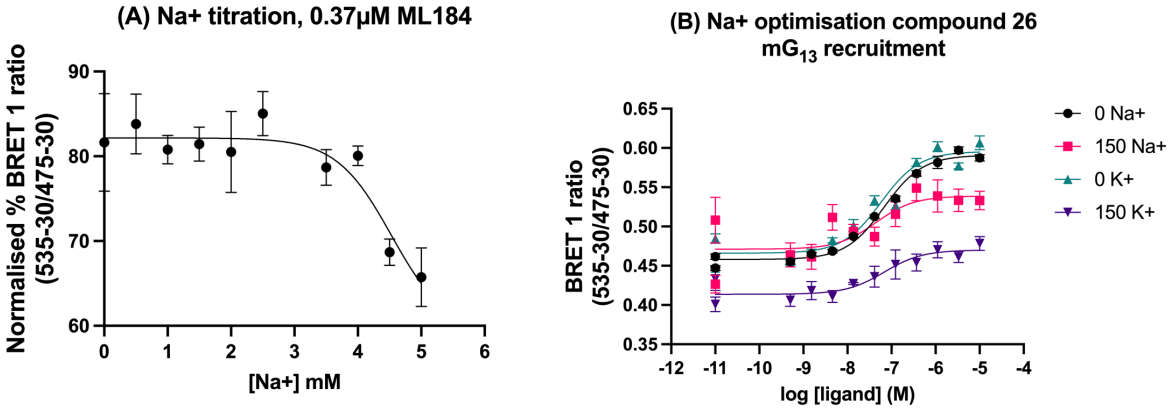
DMSO as a vehicle control. The y-axis represents the BRET ratio, normalised to the percentage of maximal response, and the x-axis represents log ligand concentration.

Since GPR55 is reported to primarily couple to the G_{13} protein, our first experiment assessed the recruitment of the vmG_{13} protein using ML184 to confirm assay functionality. The assay was performed in buffer containing HBSS, 5 mM HEPES (pH 7.5), 0.5% BSA, and 0.02% pluronic F127, adapted from membrane-based assays described in Scott-Dennis *et al.* (2023). Each well contained 0.33 µg of GPR55 membranes, 15 nM vmG_{13}, and 10 µM furimazine. ML184 final concentrations ranged from 10 µM to 0.2 nM (threefold serial dilution) **(*Figure 4*)**, with DMSO as a vehicle control, consistent with the β-arrestin recruitment and G-CASE biosensor assays. The resulting dose-response curve (***Figure 16***) displayed a shallow response window, and although Prism calculated an EC_{50} of 0.4 nM, this value is likely unreliable given that the software attempts to fit an EC_{50} regardless of data quality. With such a small response window, this assay format would not be suitable to use for reliable ligand screening.

Optimising the Na+ concentration in the assay buffer

Since sodium is reported to act as a negative allosteric modulator of class A GPCRs (Draper-Joyce *et al.*, 2018), we began by investigating the effect of sodium concentration in the assay buffer. To precisely control the salt composition, HBSS was replaced with defined NaCl solutions along with 1 mM $CaCl_2$, 1 mM $MgCl_2$, 10 mM HEPES (pH 7.5), 0.5% BSA, and 0.02% pluronic F127. We first titrated sodium concentrations from 0 to 5mM, keeping the ionic strength constant by balancing with KCl and the ligand concentration held constant at 0.37 µM.

The titration in ***Figure 17*A** though not physiologically representative, was performed to determine if small changes in the sodium ion concentration would influence our MeGaBRET assay. Since the data suggested a sodium depended decrease in BRET signal, to capture a more distinct effect of sodium, we focused only on the extremes (0 and 150mM sodium) using compound 26, our most potent ligand **(*Figure 17*B)**. To maintain the ionic strength, 0 sodium buffers contained 5 mM K^+, while 0 potassium buffers contained 5 mM Na^+. In total, we tested four conditions: high ionic strength, 150 mM Na^+, 150 mM K^+ and low ionic strength, 5 mM Na^+, 5 mM K^+. In the 150 mM Na^+ buffer, compound 26 had an EC_{50} of 44.3 nM, while in the 5 mM Na^+ buffer, the EC_{50} was 57.8 nM. However, the response window was larger under sodium-free conditions, 0.13 compared to 0.07 in the 150 mM Na^+ buffer **(*Figure 17*C).** Moreover, the EC_{50} in 5 mM K^+ (0 Na^+) buffer was lower than that in 5 mM Na^+ (0 K^+), suggesting the best assay conditions were in sodium-free conditions. Although the 150 mM Na+ buffer conditions showed reduced constitutive activity of the receptor, the shallow response window under these conditions would make it difficult to distinguish between partial and weak agonists, potentially masking weaker ligands as inactive. Therefore, we selected the sodium-free buffer to prioritise assay sensitivity over potency. The assay buffer then comprised 10 mM HEPES (pH 7.5), 1 mM $CaCl_2$, 1 mM $MgCl_2$, 5 mM KCl, 0.5% BSA, and 0.02% pluronic F127.



(C)

mM	0 Na+	150 Na+	0 K+	150 K+
pEC50s	7.17 ± 0.04	7.35 ± 0.35	7.24 ± 0.10	7.17 ± 0.18
Span	0.1328	0.0677	0.1295	0.0564

Figure 17. Effect of sodium concentration on the GPR55 MeGa-BRET assay.
The membrane based vmG_{13} recruitment assay was performed in buffer containing 10 mM HEPES (pH 7.5), 1 mM $CaCl_2$, 1 mM $MgCl_2$, 0.5% BSA, and 0.02% Pluronic F127. (**A**) Dose-response titration curve showing the effect of increasing sodium concentrations (0-5 mM) on vmG_{13} recruitment in the presence of compound 26 at a fixed concentration of 0.37µM. Ionic strength was maintained constant by balancing NaCl with KCl. The curve is plotted with the raw BRET ratio on the y-axis against sodium concentration (mM) on the x-axis. (**B**) Full dose-response curves for compound 26-mediated vmG_{13} recruitment. The assay was performed under four different buffer conditions: high ionic strength with 150 mM Na^+ (pink) or 150 mM K^+ (purple), and low ionic strength with 0 Na^+ (black) or 0 K^+ (turquoise). Ligand concentrations ranged from 0.2 nM to 10 µM at threefold serial dilutions. Curves are plotted with the raw BRET ratio on the y-axis against the log ligand concentration on the x-axis. (**C**) Summary of compound 26 potency and efficacy under the four buffer conditions.

Optimising the BSA concentration in the assay buffer

While the Na^+ optimisation allowed us to reach high efficacy with our ligands, the observed potencies were still lower than those reported in the literature and our β-arrestin recruitment assay. We therefore wanted to rule out the possibility that non-specific binding effects were disrupting ligand-receptor interactions by testing different concentrations of BSA in the assay buffer.

BSA acts as a carrier protein that reduces non-specific binding of hydrophobic ligands to plastic surfaces or other assay components. However, at higher concentrations, BSA can also bind and sequester small molecules, reducing the concentration of free (active) ligand (Blakeley *et al.*, 2015; Sykes *et al.*, 2016). For this, we evaluated 0, 0.1, 0.2, 0.3, 0.4 and 0.5 w/v % BSA and generated dose-response curves for both the synthetic agonist ML184 and the endogenous ligand LPI (***Figure 18***).

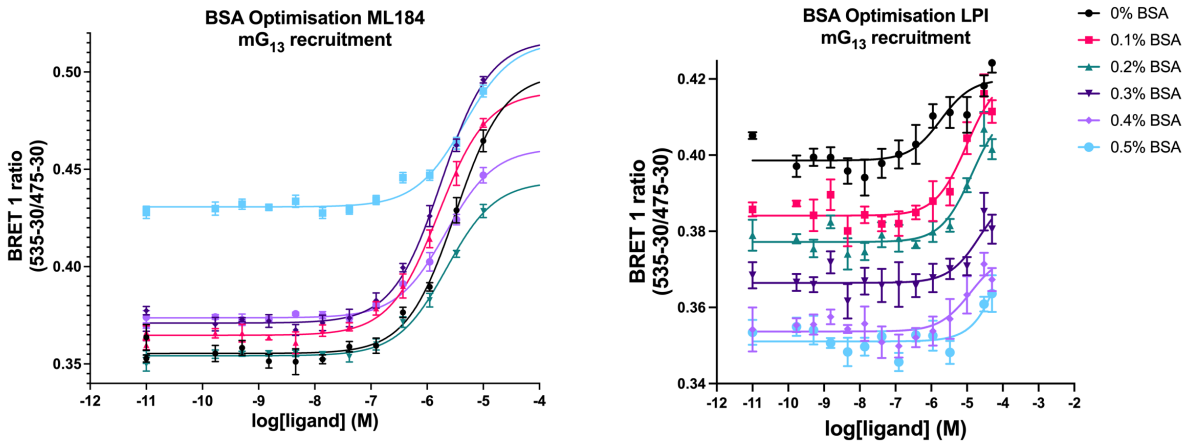


Figure 18. **Effect of BSA concentration on GPR55 ligand responses in the MeGa-BRET.** Dose-response curves showing the effect of increasing BSA concentrations in the assay buffer on vmG$_{13}$ recruitment in the presence of ML184 (**left**) and LPI (**right**). Assays were performed in buffer containing 10 mM HEPES (pH 7.5), 1 mM $CaCl_2$, 1 mM $MgCl_2$, 0.02% Pluronic F127, and 0% (blue), 0.1% (lilac), 0.2% (purple), 0.3% (green), 0.4% (pink), and 0.5% (black) BSA concentrations. Ligands were applied in threefold serial dilutions starting from 10 µM to 0.2nM, with DMSO as the vehicle control. The raw BRET ratio (535/475 nm) is plotted on the y-axis, and the log of the ligand concentration is plotted on the x-axis. Data are presented as mean ± SEM, n = 3.

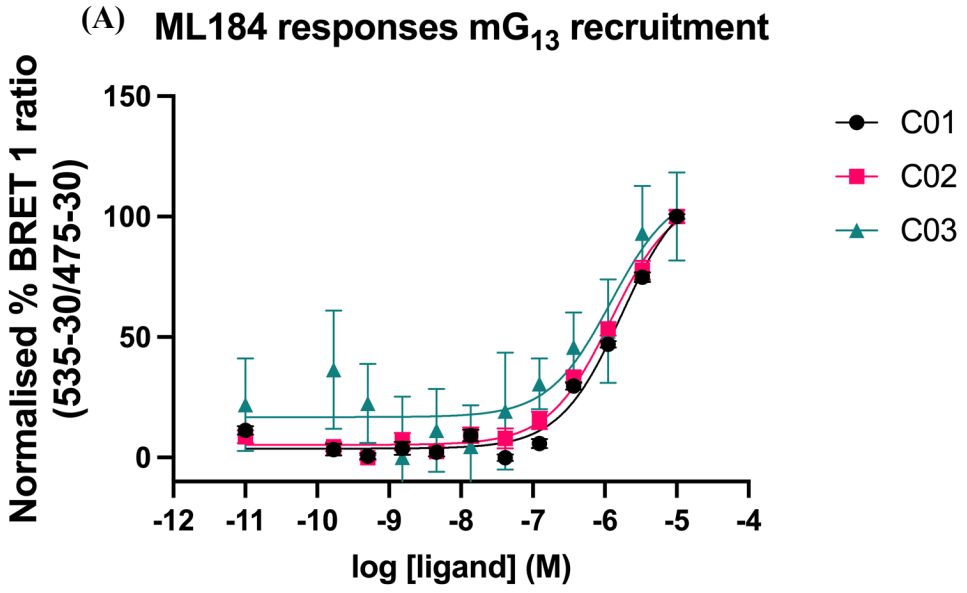
The results in ***Table 3*** show that for both ligands, 0% BSA produced an elevated baseline and a shallow response window, suggesting some non-specific interactions were affecting the assay. For ML184, increasing BSA concentrations lowered the baseline and increased the response window of the assay. Potency was relatively similar across BSA concentrations, although a slight loss of potency was observed at the highest concentration (0.5% BSA). So, BSA concentrations between 0.1% and 0.4% would be suitable for ML184. In contrast, LPI displayed some dependence on BSA concentration. At 0% BSA, potency was highest (EC_{50} = 1.36 µM), but the baseline was also elevated, and the response window was small. Adding 0.1% BSA reduced the baseline and increased the response window, while higher concentrations of BSA produced progressive rightward shifts in the dose-response curve and a reduction in the size of the response window.
Taking these data together, we selected 0.1% BSA as the final assay condition, as it provided the best balance between minimising non-specific binding and maintaining measurable responses. The final assay buffer comprised 10 mM HEPES (pH 7.5), 1 mM $CaCl_2$, 1 mM $MgCl_2$, 5 mM KCl, 0.1% BSA, and 0.01% pluronic F127.

Table 3. Effect of BSA concentration on ML184 and LPI potency and efficacy.
This table summarises the pEC50 and span values for the agonists ML184 and LPI at varying BSA concentrations (0%, 0.1%, 0.2%, 0.3%, 0.4%, and 0.5%). Data were derived from the dose-response curves shown in ***Figure 18***. Data are presented as mean ± SEM, n = 3.

BSA w/v (%)	ML184		LPI	
	pEC50	Span	pEC50	Span
0	5.342 ± 0.077	0.0850	5.733 ± 0.16	0.0214
0.1	5.669 ± 0.040	0.0872	5.012 ± 0.12	0.0370
0.2	5.746 ± 0.032	0.1453	4.861 ± 0.13	0.0358
0.3	5.657 ± 0.040	0.0896	4.638 ± 0.29	0.0245
0.4	5.797 ± 0.036	0.1252	4.907 ± 0.23	0.0203
0.5	5.497 ± 0.051	0.1438	3.748 ± 1.36	0.0597

Ligand potency across constructs C01, C02 and C03

To assess the effect of the linker on the GPR55-sLuc constructs on assay performance, mG protein recruitment was tested using ML184 in the 10 mM HEPES (pH 7.5), 1 mM $CaCl_2$, 1 mM $MgCl_2$, 5 mM KCl, 0.1% BSA, and 0.01% pluronic F127 assay buffer **(*Figure 19* A** and **B)**. One-way ANOVA revealed no significant differences in EC_{50} values among the three GPR55-sLuc constructs p = 0.0868. The response windows were also comparable across constructs, supporting that all three linkers produced similar assay performance.



(B)

Construct	C01	C02	C03
pEC_{50}	5.76 ± 0.04	5.92 ± 0.04	5.92 ± 0.21
Span (%)	111.5	103.7	95.5

Figure 19. **Comparison of ML184-induced vmG_{13} recruitment across GPR55 constructs in MeGa-BRET.**
Concentration-response curves showing the effect of the GPR55 agonist ML184 on vmG_{13} recruitment to membranes expressing GPR55 fused to sLuc at the C-terminus via either a flexible GSGS linker (C01, black), a CB2R (residues 340–360) derived linker (C02, pink), or a β2AR (residues 313–393) derived linker (C03, turquoise). The assay buffer consisted of 10 mM HEPES (pH 7.5), 1 mM $CaCl_2$, 1 mM $MgCl_2$, 5 mM KCl, 0.1% BSA, and 0.01% pluronic F127. ML184 was applied at final concentrations ranging from 10 μM to 0.2 nM using threefold serial dilutions, with DMSO as a vehicle control. The curves show BRET ratio, normalised to the percentage of maximal response on the y-axis, and the log ligand concentration on the x-axis. Curves were fitted using non-linear regression. A one-way ANOVA indicated no significant difference in EC_{50} values among the constructs ($p = 0.0868$). (**B**) Potency and efficacy data of ML184 with each construct from panel A. Data are presented as mean ± SEM, n = 3.

MeGaBRET successfully quantifies ligand induced GPR55 activation.

We then ran the mG_{13} protein recruitment assay using our selection of ligands: ML184, compound 26, compound 28, compound 29, RO7684969, LPI, AM251, O-1602 and THC in triplicate **(*Figure 20*)**. For ML184, we obtained an EC_{50} of 1.1 μM, which was ~4.4-fold lower in potency than the reported 250 nM and ~2-fold lower than its potency in the β-arrestin recruitment assay. For compound 26, we obtained an EC_{50} of 41nM, representing a ~6.6-fold decrease in potency compared to the reported EC_{50} of 6.2 nM and ~4.5-fold decrease compared to 9.2 nM from the β-arrestin recruitment assay **(*Table 1)***. So, while our assay reproduced ligand activity profiles, it consistently reported slightly reduced potencies relative to the β-arrestin-based recruitment assays. Interestingly, THC showed some vmG_{13} protein recruitment with an EC50 of ~55.5 μM, highlighting that ligands with bias toward G protein pathways are overlooked in β-arrestin assays. As an additional check to exclude random collision BRET as the signal source, we tested CBD, a GPR55 antagonist. CBD produced no concentration-dependent increase in mG_{13} protein recruitment, suggesting that the observed signals represent specific receptor-mediated interactions.

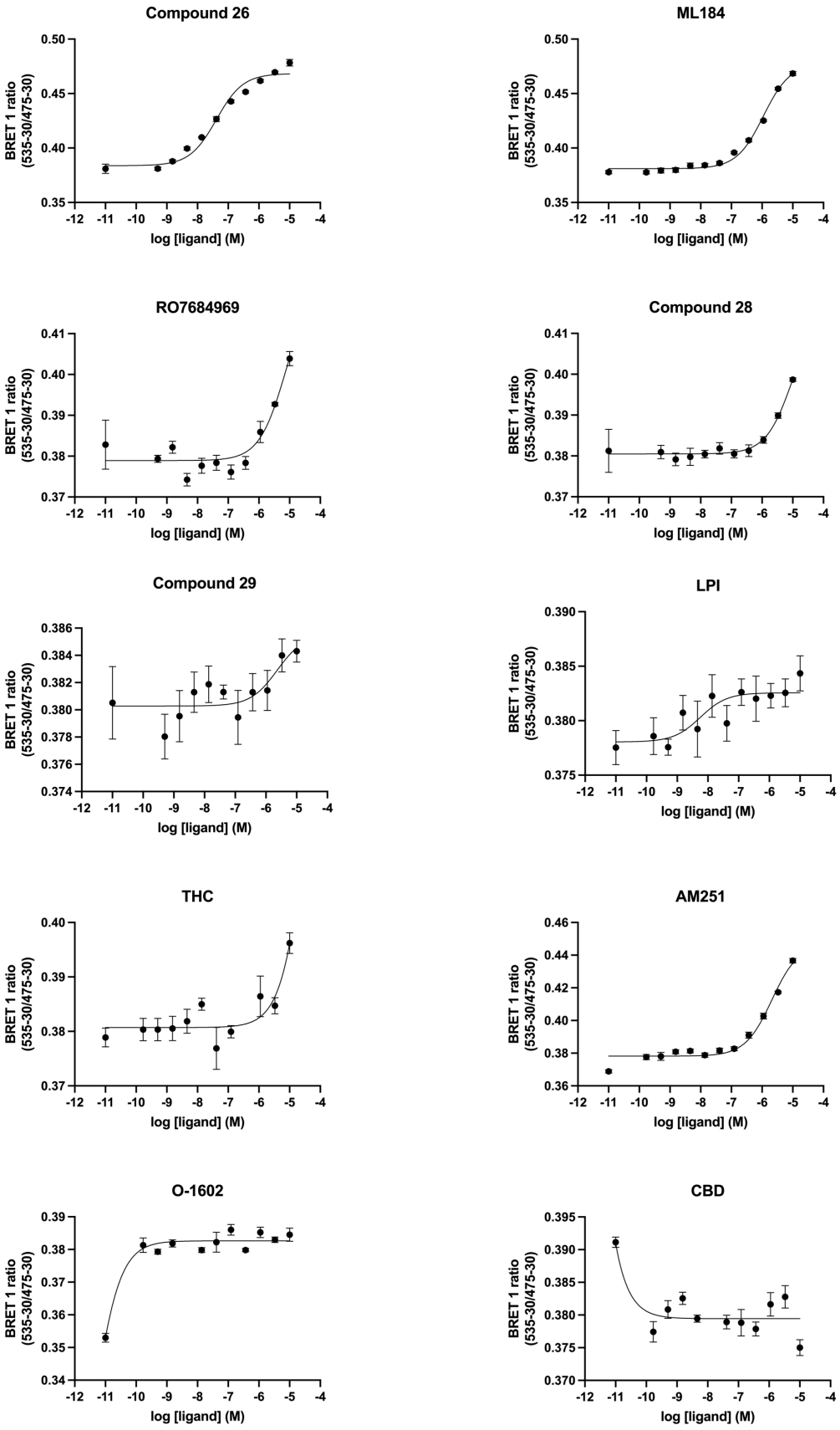
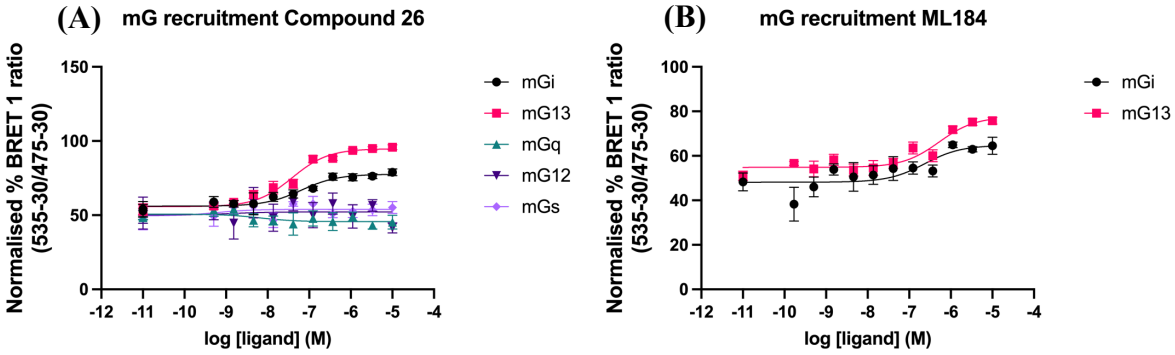


Figure 20. **Membrane-based vmG$_{13}$ recruitment assays.**
Concentration-response curves showing vmG$_{13}$ protein (15nM per well) recruitment to 0.33 µg per well of Expi293F™ suspension cell membranes expressing GPR55-sLuc following

stimulation with the agonists compound 26, ML184, RO7684969, compound 28, compound 29, LPI, THC, AM251, and O-1602, as well as the antagonist CBD at final concentrations ranging from 10 µM to 0.2 nM using threefold serial dilutions, with DMSO as a vehicle control. Assays were performed in buffer containing 10 mM HEPES (pH 7.5), 1 mM $CaCl_2$, 1 mM $MgCl_2$, 5 mM KCl, 0.1% BSA, and 0.01% pluronic F127. The y-axis represents the raw BRET ratio (535/475 nm), and the x-axis represents log ligand concentration. Data are presented as mean ± SEM, n = 3.

Exploration of G-protein coupling specificity

All the assay optimisations and initial validation experiments were performed using the vmG_{13} protein. However, since GPR55 has also been reported to couple to the $G\alpha_{12}$ and $G\alpha_q$ proteins, we next tested whether our assay conditions could detect recruitment of the vmG_{12} and vmG_q proteins. As an additional control for specificity, we also assessed the vmG_s and vmG_i proteins. The most potent ligand, compound 26, was used as the reference agonist to validate assay performance, with vmG_{13} protein recruitment serving as the positive control. All experiments were carried out in assay buffer containing 10 mM HEPES (pH 7.5), 1 mM $CaCl_2$, 1 mM $MgCl_2$, 5 mM KCl, 0.1% BSA, and 0.01% pluronic F127 (***Figure 21*****A** and **C**).



(C)

vmG	13	12	q	i	s
Compound 26 pEC50s	7.41 ± 0.07	n.d.	n.d.	7.19 ± 0.14	n.d.
ML184 pEC50s	6.28 ± 0.12	-	-	6.63 ± 0.39	-

Figure 21. vmG protein recruitment to GPR55-sLuc membranes.
(**A**) Concentration-response curves showing recruitment of vmG_{13} (pink), vmG_{12} (purple), vmG_i (black), vmG_q (turquoise), and vmG_s (lilac) proteins to membranes expressing GPR55-sLuc following stimulation with compound 26. (**B**) Concentration-response curves showing recruitment of vmG_{13} (pink) and vmG_i (black) proteins following stimulation with ML184. (**C**) Summary table comparing pEC_{50} values for vmG protein subtypes in response to compound 26 and ML184. '-' indicates conditions where data were not collected. All assays were performed with 15 nM vmG protein and 0.33 µg of Expi293F™ suspension cell membranes (C01 construct) expressing GPR55 per well. The assay buffer contained 10 mM HEPES (pH 7.5), 1 mM $CaCl_2$, 1 mM $MgCl_2$, 5 mM KCl, 0.1% BSA, and 0.01% Pluronic F127. The y-axis

represents the BRET ratio (535/475 nm) normalised to the percentage of maximal response, and the x-axis represents log ligand concentration. Data are presented as mean ± SEM, n = 3.

As expected, there was no recruitment of the mG_s protein. Surprisingly, we also failed to detect mG_q protein recruitment, despite previous reports in the literature (Lauckner *et al.*, 2008). To confirm that the lack of recruitment was not due to the degradation of the purified protein, we tested the vmG_q protein construct in a β_2-adrenergic receptor control assay, where robust recruitment was observed (data not shown). This indicated that the purified vmG_q protein was functional but was not recruited by GPR55.
Recruitment of the mG_{12} protein proved more difficult to determine. Across three independent experiments, we did not observe a reproducible response. We suspected that the purified vmG_{12} protein might have degraded, reducing its suitability for the assay. To test this, we cultured and purified a fresh batch of vmG_{12}. The SDS-PAGE analysis in ***(Figure 22)*** revealed a protein band at the expected molecular weight of ~54 kDa, as well as thicker bands around 27 kDa, consistent with the sizes of Venus and mG_{12} proteins. This degradation likely contributed to the inconsistent recruitment signals. Unfortunately, the lack of a validated positive control receptor-ligand pair for the mG_{12} protein meant we could not verify this assay further.

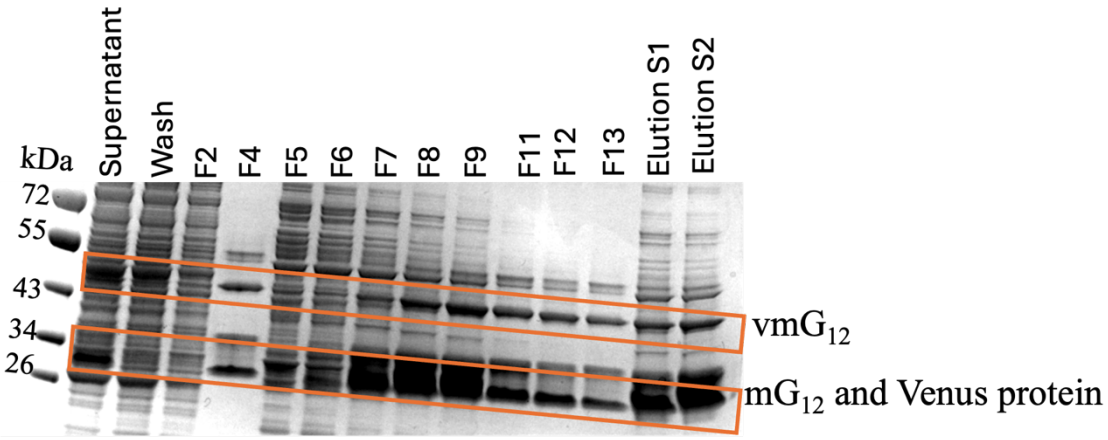


Figure 22. **SDS-PAGE analysis of vmG12 protein expression.**
His-TEV-Venus-mini-G12 (vmG12) was expressed in E. coli BL21(DE3) LOBSTR cells and purified by Ni-NTA affinity chromatography using a HisTrap FF crude column on an ÄKTA™ Start system. Elution fractions were analysed by SDS-PAGE and stained with Coomassie Blue. Molecular weight markers are shown on the left (kDa). Orange boxes highlight the expected protein bands, with the vmG12 fusion protein appearing at ~54 kDa and degradation products corresponding to Venus and mG12 observed at ~27 kDa.

Unexpectedly, we observed clear concentration-dependent recruitment of the vmG_i protein, a G-protein subtype not widely reported to couple with GPR55. While the efficacy of vmG_i protein recruitment was lower than that observed for the vmG_{13} protein, the potencies were comparable **(*Figure 21*C)**. The functionality of the vmG_i protein was also validated using CB1 and CB2 receptors as positive controls in parallel assays (data not shown). To further confirm this unexpected coupling, we repeated the experiment using ML184, which also produced concentration-dependent vmG_i protein recruitment **(*Figure 21*B)**.

Chapter Four: Discussion

Analysis of computational work.

Despite its emerging role as a therapeutic target in cancer, inflammation, pain, and metabolic disorders, the pharmacology of GPR55 remains poorly defined, largely due to conflicting assay results and the lack of potent and selective ligands (Simcocks et al., 2014). In this study, we sought to address these challenges by combining computational and experimental approaches to achieve a more detailed pharmacological characterisation of GPR55. Using AutoDock Vina molecular docking software, Arpeggio to generate interaction fingerprints, and the CatBoost machine learning classifier model, we identified the residues W177^{ECL2}, P155$^{4.59x60}$, M167^{ECL2}, Q271$^{7.36x35}$, F102$^{3.33x33}$, V149$^{4.53x53}$, M274$^{7.39x38}$, F246$^{6.55x55}$, M172^{ECL2}, L270$^{7.35x34}$, and I156$^{4.60x61}$ as potentially crucial for governing ligand pharmacology. Then, developed a membrane-based mG protein recruitment assay (MeGaBRET) for GPR55 to provide a more controllable and robust platform to functionally validate ligand activity. Together, these complementary approaches enabled us to begin bridging the gap between structural predictions and functional outcomes.

Transitioning from 'which' to 'how' ligands bind to GPR55.

When this project began, GPR55, like many recently deorphanised receptors, had no resolved structures. Much of the early research was guided by the hypothesis that GPR55 acts as a cannabinoid receptor, which provided a useful starting point for testing ligands already known to bind the CB1 and CB2 receptors (Ryberg *et al.*, 2007). Using this rationale, high-throughput functional assays like the β-arrestin recruitment, [^{35}S]GTPγS, Ca^{2+} and ERK activation assays (Kapur *et al.*, 2009; Oka *et al.*, 2007; Lauckner *et al.*, 2008) were employed to determine whether these ligands also interacted with GPR55. However, these approaches only established which ligands could bind, without explaining how they did so. This gap in knowledge represents a major bottleneck in drug discovery, as rational drug design requires a detailed understanding of ligand-receptor interactions (Lounnas *et al.*, 2013). By determining how a compound binds, specifically by identifying the key amino acid residues involved, we can start to understand how those interactions stabilise specific receptor conformations, and how these conformational changes are connected to signalling pathways. Once such molecular details are mapped out, they can be used to inform the discovery of novel drugs or for modifying existing compounds to improve potency, selectivity, or pharmacological properties.

Our predicted GPR55 ligand binding pocket.

Therefore, this work began with an effort to understand how ligands bind to GPR55. Specifically, to identify what distinguishes an agonist from an antagonist by inspecting the receptor residues they interact with using computational methods. The computational workflow identified W177^{ECL2}, P155$^{4.59x60}$, M167^{ECL2}, Q271$^{7.36x35}$, F102$^{3.33x33}$, V149$^{4.53x53}$, M274$^{7.39x38}$, F246$^{6.55x55}$, M172^{ECL2}, L270$^{7.35x34}$, I156$^{4.60x61}$ as the main residues interacting with GPR55 ligands. The majority of these are hydrophobic residues, which fits with the lipid-based nature of the endogenous ligand LPI and the hydrophobic character of many GPR55 ligands. Additionally, other residues such as F110$^{3.41x41}$, H170^{ECL2}, L185$^{5.42x43}$, F188$^{5.48x46}$, and Y106$^{3.37x37}$ were also predicted in our docking results, but their interactions were not consistent across structures, suggesting they may be unique to specific receptor conformational structures.

Key ligand interactions and binding patterns

Docking was then performed on the ten ligands available for experimental testing (compound 26, ML184, LPI, AM251, O-1602, THC, compound 28, compound 29, RO7684969, and CBD). The aim was to predict their binding interactions before laboratory assays, in order to assess whether computationally identified differences could later be linked to signalling outcomes, potencies, or pharmacological profiles. Our molecular docking exercise predicted that all ten ligands made interactions with residues W177^{ECL2}, F102$^{3.33x33}$, and F246$^{6.55x55}$, suggesting these residues may act as molecular switches critical for stabilising ligand binding. The residue Q271$^{7.36x35}$ was the only polar binding residue predicted. We also predicted that CBD, LPI, ML184, and THC extended further into the binding pocket to interact with V149$^{4.53x53}$, although this did not translate into similar binding patterns among these ligands in the signalling assays. While CBD was the only literature confirmed antagonist (Kapur *et al.*, 2009) we tested, our docking data did not reveal any interactions unique to it. Similarly, the potent agonists, compound 26 and ML184, did not exhibit unique interaction patterns that could fully explain their high potency. Moreso, while the predicted antagonist-specific residue I156$^{4.60x61}$ did interact with antagonist CBD, it also formed interactions with LPI, ML184, and THC, suggesting it is not a sole determinant of antagonist activity.

Comparison with resolved GPR55 cryo-EM structures

When compared to the recently published GPR55 cryo-electron microscopy structures (Claff *et al.*, 2025; Xia *et al.*, 2024), there was partial agreement with our predictions. The structures validated many residues in our docking results, including F102$^{3.33x33}$, I156$^{4.60x61}$, L270$^{7.35x34}$, M172^{ECL2}, M274$^{7.39x38}$, F246$^{6.55x55}$, Q271$^{7.36x35}$, and W177^{ECL2}. They also confirmed that residues H170^{ECL2}, and Y106$^{3.37x37}$ were actually part of the binding pocket. Additional residues such as N16$^{1.28x28}$, N171^{ECL2}, R253$^{6.62x62}$, F169^{ECL2}, M172^{ECL2}, Y101$^{3.32x32}$, and hydrophilic residues E98$^{3.29x29}$, Q23$^{1.35x35}$, and Q249$^{6.58x58}$ were also highlighted, which had not been identified by our simple docking approach. The resolved cryo-EM structures also confirmed our predictions that the binding pocket was primarily mediated by the hydrophobic interactions of W177^{ECL2}, M172^{ECL2}, F169^{ECL2}, Y101$^{3.32x32}$, M274$^{7.39x38}$, and L270$^{7.35x34}$ residues. Although our docking model identified residues P155$^{4.59x60}$, M167^{ECL2} and V149$^{4.53x53}$ as also being part of the binding pocket, these were not explicitly shown to be crucial for binding in the published cryo-EM structures, highlighting a limitation of our simple docking approach.

Limitations of ensemble docking and SVM classification accuracy

While our computational approach provided valuable insights into the binding patterns of GPR55, its classification performance shown as MCC values ranging in the moderate 0.25 to 0.39 across different receptor structures (***Table 2***) signal some methodological limitations. One major challenge was the model's limited ability to identify more residues that are important for antagonist binding. This is reflected in the high counts of false negatives observed in the confusion matrices, where antagonists were incorrectly classified as agonists. A likely contributing factor if the dataset size. Jiménez-Rosés *et al.* (2022) reported that reasonable performance of classifiers such as random forest can be achieved with datasets of around 300-450 compounds, but that larger datasets are required to capture more complex relationships, such as continuous rather than binary structure-activity trends. Furthermore, our docking results are a summary of the interactions from all the receptors with only one inactive state receptor. By relying mainly on active-state structures, we may overlook ligands that preferentially bind to the inactive receptor, since it is difficult for the model to learn from forms that are underrepresented or absent. An additional factor is the reliance on reported

pharmacological activity. The accuracy of our model's predictions is directly tied to the quality of the curated dataset. Inaccuracies in source data or biases in the assays used to classify ligand pharmacology could directly affect the model's predictive performance.

Beyond data limitations, our docking strategy using Autodock Vina (Trott and Olson, 2010) also presents some constraints. Specifically, we use a semi-rigid docking approach, which treats the receptor as rigid and the ligand as flexible up to ten binding poses. Although we attempted to account for receptor flexibility by performing ensemble docking across multiple cryo-EM structures, each representing slightly different conformations depending on the bound ligand. Nonetheless, this approach still relies on essentially rigid receptor models. As a result, it only captures a limited subset of the possible ligand binding poses and may overlook dynamic interactions that occur in a fully flexible receptor environment. We also restrict docking to a customised grid made around the known orthosteric ligand binding pocket. While this approach helps to reduce noise from random binding events, it limits our ability to detect allosteric sites or cases where the ligands may occupy multiple pockets simultaneously. Additionally, although Autodock Vina can rank ligands by predicted binding affinity, it cannot identify which docking poses are functionally relevant. Consequently, our dataset contains some noise from poses that are unlikely to reflect the true binding mode. However, in a large enough dataset of diverse ligands and multiple docking poses, the functionally important atomic interactions are expected to be overrepresented, while the noise (irrelevant poses) tend to average out. This rationale underlies the use of atomic interaction fingerprints for machine learning allowing meaningful patterns to emerge despite docking uncertainties (Jiménez-Rosés *et al.*, 2022).

Analysis of experimental work

Although our computational analyses highlighted key residues and potential interaction patterns for GPR55 ligands, these predictions, like all computational work, need experimental validation to confirm their biological relevance. To do this, we designed an experimental strategy aimed at both testing our hypotheses and addressing some of the known challenges in GPR55 pharmacology. We combined established whole-cell assays β-arrestin recruitment and the G-CASE biosensor with a newly developed membrane-based assay, selected for its ability to provide sensitive and controllable measures of ligand activity.

A persistent challenge in GPR55 research has been the poor reproducibility and inconsistency of assay results across laboratories and assay platforms. For instance, it was only relatively recently that lysophosphatidylinositol (LPI) was widely recognised as the endogenous ligand of GPR55, leading to its formal deorphanisation (Ross, 2009; Shore and Reggio, 2015). Therefore, we began our experimental work by first attempting to reproduce published findings using the β-arrestin recruitment and the G-CASE biosensor assays, two widely adopted cell-based assays. Cell-based assays are advantageous because they better capture the physiological context of receptor signalling, including receptor localisation, accessory proteins, and cellular environment, which can influence ligand activity and signalling outcomes.

Analysis of the β-Arrestin Recruitment Assay

We first focused on the β-arrestin recruitment assay, as it is one of the most widely reported methods for assessing ligand pharmacology at GPR55 (Hewer *et al.*, 2023; Kotsikorou *et al.*,

2011; Kapur *et al.*, 2009). This approach is particularly valuable for orphan GPCRs because it provides a pathway-independent readout of receptor activation when the identity of coupled G proteins or downstream second messengers is unknown. Furthermore, since β-arrestin recruitment is an early event in GPCR signalling, it offers a robust measure of receptor activation and enables the quantification of ligand potency and efficacy.

Limitations of the β-Arrestin Recruitment Assay

However, a key limitation of this assay is its susceptibility to biased signalling. Not all agonists will promote a conformational change of the receptor that will allow for the recruitment of β arrestin, meaning that negative results do not necessarily indicate a lack of receptor activity. For example, in our BRET-based β-arrestin recruitment assay in HEK293TR cells, THC produced no measurable change in BRET signal. This finding is consistent with that of Kapur *et al.* (2009) who also reported no β-arrestin recruitment by THC in GPR55-expressing HEK293 and U2OS cells using βarrestin2-GFP redistribution assays (Shenoy and Lefkowitz, 2003). Based on these results alone, one might conclude that THC is not an agonist at GPR55. However, when we performed a mG_{13} recruitment assay, we observed agonist activity with a low potency (EC50 ~245 μM). Taken together, these data demonstrate that THC does not signal through β-arrestin but is instead biased towards the G_{13} protein signalling pathway.

Another limitation of the β-arrestin recruitment assay is that it is a whole-cell based approach, which makes it vulnerable to variability between laboratories. Differences in cell type, expression system, and assay design can all influence the outcome, leading to inconsistencies that complicate reproducibility and standardisation across studies. A good example of this issue is ML184, one of our most potent GPR55 ligands. In our BRET-based β-arrestin recruitment assay using HEK293TR cells, we observed an EC_{50} of 550nM. Kotsikorou *et al.* (2011) reported a lower EC_{50} of 250nM using βarr2-GFP redistribution in GPR55-expressing HEK293 and U2OS cells. By contrast, Hewer *et al.* (2023) reported an even more potent EC_{50} of 15nM using the PathHunter β-arrestin assay (DiscoverX), a commercially available enzyme fragment complementation system in HEK293-EA cells (Zhao *et al.*, 2008). These discrepancies show the variability of β-arrestin recruitment assays and the impact this has on how we interpret ligand pharmacology at GPR55. It also highlights why it is important to validate results across multiple assays and to work towards more standardised approaches for screening GPR55 ligands.

Unsuccessful implementation of the G-CASE biosensor for GPR55.

Similarly, our use of the G-CASE biosensor assay was intended to provide an additional cell-based assay to validate the results from the β-arrestin recruitment assay. The G-CASE biosensor assay is another BRET-based method that directly measures the dissociation of the Gα subunit from the Gβγ subunits, providing a more direct readout of receptor activation. However, despite multiple attempts to optimise the assay, we were unable to obtain a reliable response for any of the GPR55 ligands. It remains unclear whether the difficulty arose from GPR55 overexpression being toxic to the cells, although this did not appear to affect the β-arrestin assay performed in the same cell line. In hindsight, a useful check would have been to use a localisation assay (Lan *et al.*, 2012) to confirm GPR55 expression at the membrane. Instead, we only monitored the G protein expression by tracking the Venus fluorescence on the green channel of the Invitrogen™ FLoid™ Cell Imaging Station, which would not identify any issues with receptor expression.

Advantages of MeGaBET over conventional cell-based assays.

Given the variability and limitations we observed with conventional cell-based assays, we next developed a membrane-based mG protein recruitment assay (MeGaBRET). Unlike whole-cell approaches, this assay allows for control over the assay environment, including the amount of receptor and mG proteins present, providing a more manageable system for assessing ligand activity. Also, MeGa-BRET can be applied to orphan GPCRs. If the receptor's endogenous G protein coupling is unknown, a solution of combined mG proteins can be used to assess the functional effects of compounds, allowing the assay to identify receptor activity without prior knowledge of its signalling partners.

A further advantage of MeGaBRET is its enhanced workflow speed. Cell-based assays typically require stable cell lines, which can take up to four weeks to establish, with double-stable lines taking even longer. Also, the running of the cell-based assay itself generally requires about five days from initial cell plating. In contrast, MeGaBRET using Expi293F™ suspension cells require only about five days from transfection to harvesting, followed by a single day for membrane preparation. The production of mG proteins also takes about five days from bacterial transformation to purification, meaning the overall workflow is still considerably faster than developing stable cell lines.

Using the BRET-based mG_{13} protein recruitment assay, we tested the activity of our panel of ten GPR55 ligands. One of the key observations from MeGa-BRET was that the endogenous ligand LPI and THC both showed strong bias towards mG_{13} protein recruitment. This is particularly interesting because both ligands interact with the same set of binding site residues, $V149^{4.53x53}$, $I156^{4.60x61}$, $F102^{3.33x33}$, $W177^{ECL2}$, and $F246^{6.55x55}$, suggesting that one or more of these interactions might be important in driving G protein bias.

Another notable finding was that although most ligands showed lower potency in the membrane-based assay compared to the β-arrestin recruitment assay, the response window was larger in the MeGa-BRET assays. For example, ML184 had an EC_{50} of 1.1 μM in the MeGa-BRET assay, with a span of 0.097, compared to an EC_{50} of 550 nM and a span of only 0.014 in the β-arrestin recruitment assay. This wider response window is highly advantageous as it provides a clearer and more robust signal, making it easier to distinguish between full and partial agonists and to detect low-efficacy ligands that might otherwise be overlooked or misclassified in assays with a narrower window. It also improves reproducibility by reducing the impact of small variations in experimental conditions. Together, these features highlight the membrane-based assay as a stronger platform for ligand screening than conventional cell-based assays.

Limitations of MeGaBRET.

However, the relatively low potency we observed may be due to a technical limitation in how the assay was set up. Unlike in other G protein-based assays, we did not include 5'-guanylylimidodiphosphate (GppNHp), a stable, non-hydrolysable analogue of GTP that binds and irreversibly activates endogenous G proteins, leading to their dissociation from the receptor (Mystek *et al.*, 2015; Mach *et al.*, 2024). Once the endogenous G proteins are dissociated, the introduced mG proteins can bind more effectively to the receptor. This would likely improve the apparent potency of the ligands by reducing interference from endogenous G proteins. Incorporating GppNHp in future experiments would therefore be a straightforward optimisation that could enhance the sensitivity of the assay and provide a more accurate measure of ligand pharmacology. This may also explain why O-1602 produced no measurable

response in any of our assays, despite being reported as a potent GPR55 ligand with an EC_{50} of 13 nM in GTPγS binding assays (Ryberg *et al.*, 2009).

Overall, these features make the MeGa-BRET assay a powerful and flexible platform for GPR55 ligand screening. It combines the reproducibility and control of a simplified system with the ability to assess low-efficacy ligands and rapidly test multiple compounds. However, like any assay, it is not without limitations. For example, it performed reliably for mG_{13} and mG_i protein recruitment but less effectively for mG_q and mG_{12}, both of which have also been implicated in GPR55 signalling. This limitation may reflect differences in the optimal buffer conditions required for individual mG proteins, which could be addressed through further assay optimisation.

Another limitation of the MeGaBRET system is in the production of the mG proteins. As these constructs are expressed in *E. coli*, they can lack the post-translational modifications present in mammalian proteins, which may influence their folding, stability, or functional properties. In addition, the vmG proteins contain numerous reduced cysteines that are essential for their activity, requiring the use of reducing agents such as DTT in all purification and storage buffers. However, since DTT is a nickel ion chelator, its concentration and quality had to be carefully controlled to prevent stripping of nickel from the Ni-NTA columns during purification. Furthermore, the linker between Venus and the mG protein is prone to degradation and still requires optimisation, contributing to the instability of the chimeric protein. These considerations highlight the importance of including positive controls for each vmG protein, ideally using well characterised receptor-ligand pairs. In this work, however, the positive controls were the high-potency ligands rather than a validated receptor system for vmG_{13}, since no such system was available. Nevertheless, with consistent results across three replicates, we are confident that our findings were reproducible.

Conclusions and future directions

The work presented here provides new insights into the pharmacology of GPR55, a receptor of growing therapeutic interest in cancer, inflammation, pain, and metabolic disorders. Despite its potential, the signalling mechanisms of GPR55 remain poorly defined, in part due to assay variability and a lack of selective ligands. By combining molecular docking, interatomic fingerprinting, and machine learning, this study successfully mapped the GPR55 binding pocket and identified $W177^{ECL2}$, $F102^{3.33x33}$, and $F246^{6.55x55}$ as key residues that may act as molecular switches for ligand binding and signalling outcomes. This "how" of ligand binding offers valuable guidance for medicinal chemistry, supporting the rational design of new ligands or the optimisation of existing compounds.

Experimentally, we complemented these computational predictions with cell-based β-arrestin and G-CASE biosensor assays and developed a new membrane-based vmG protein recruitment assay. While the cell-based assays better capture physiological context, they proved variable and technically challenging. The MeGa-BRET assay offers a simplified, controllable, and faster setup, enabling clearer differentiation when screening ligands.

Looking forward, incorporating molecular dynamics simulations would provide a better picture of receptor-ligand interactions than semi-rigid docking alone. Experimentally, integrating GppNHp into the MeGa-BRET system, using beta-mercaptoethanol (BME) intead of DTT during mG protein purification, optimising the linker between the Venus and mG protein and refining buffer conditions for the different vmG proteins could enhance the sensitivity and

accuracy of pharmacological measurements. Beyond GPR55, the adaptability of MeGa-BRET means it could be applied to orphan GPCRs, offering a powerful platform for both ligand screening and receptor deorphanisation.

In conclusion, this work demonstrates the value of combining computational and experimental approaches to study GPR55. Together, these strategies not only advance our mechanistic understanding of this receptor but also provide a new tool and framework for robust ligand screening. By bridging prediction with validation, this work lays the foundation for future drug discovery efforts and supports the broader goal of developing therapeutics targeting GPR55.

References

Alexander, S. P. H. , Christopoulos, A., Davenport, A. P., Kelly, E., Mathie, A. A., Peters, J. A., Veale, E. L., Armstrong, J. F., Faccenda, E., Harding, S. D., Davies, J. A., Abbracchio, M. P., Abraham, G., Agoulnik, A., Alexander, W. and Al-Hosaini, K. and Back, M. and Baker, J. G. and Barnes, N. M., Bathgate, R., Beaulieu, J. M., Beck-Sickinger, A. G., Behrens, M., Bernstein, K. E., Bettler, B., Birdsall, N. J. M., Blaho, V., Boulay, F., Bousquet, C., Brauner-Osborne, H., Burnstock, G., Calo, G., Castano, J. P., Catt, K. J., Ceruti, S., Chazot, P., Chiang, N., Chini, B., Chun, J., Cianciulli, A., Civelli, O., Clapp, L. H., Couture, R., Cox, H. M., Csaba, Z., Dahlgren, C., Dent, G., Douglas, S. D., Dournaud, P., Eguchi, S., Escher, E., Filardo, E. J., Fong, T., Fumagalli, M., Gainetdinov, R. R., Garelja, M. L., de Gasparo, M., Gerard, C., Gershengorn, M., Gobeil, F., Goodfriend, T. L., Goudet, C., Gratz, L., Gregory, K. J., Gundlach, A. L., Hamann, J., Hanson, J., Hauger, R. L., Hay, D. L., Heinemann, A., Herr, D., Hollenberg, M. D., Holliday, N. D., Horiuchi, M., Hoyer, D., Hunyady, L., Husain, A., AP, I. J., Inagami, T., Jacobson, K. A., Jensen, R. T.,Jockers, R., Jonnalagadda, D., Karnik, S., Kaupmann, K., Kemp, J., Kennedy, C., Kihara, Y., Kitazawa, T.,Kozielewicz, P.,Kreienkamp, H. J., Kukkonen, J. P., Langenhan, T., Larhammar, D., Leach, K., Lecca, D., Lee, J. D., Leeman, S. E., Leprince, J., Li, X. X., Lolait, S. J., Lupp, A., Macrae, R., Maguire, J., Malfacini, D., Mazella, J., McArdle, C. A., Melmed, S., Michel, M. C., Miller, L. J., Mitolo, V., Mouillac, B., Muller, C. E., Murphy, P. M., Nahon, J. L., Ngo, T., Norel, X., Nyimanu, D., O'Carroll, A. M.,Offermanns, S., Panaro, M. A., Parmentier, M., Pertwee, R. G., Pin, J. P., Prossnitz, E. R., Quinn, M., Ramachandran, R., Ray, M., Reinscheid, R. K., Rondard, P., Rovati, G. E., Ruzza, C., Sanger, G. J., Schoneberg, T., Schulte, G., Schulz, S., Segaloff, D. L., Serhan, C. N., Singh, K. D., Smith, C. M., Stoddart, L. A., Sugimoto, Y., Summers, R., Tan, V. P., Thal, D., Thomas, W. W., Timmermans, P., Tirupula, K., Toll, L., Tulipano, G., Unal, H., Unger, T., Valant, C., Vanderheyden, P., Vaudry, D. and Vaudry, H. and Vilardaga, J. P. and Walker, C. S. and Wang, J. M. and Ward, D. T., Wester, H. J., Willars, G. B., Williams, T. L., Woodruff, T. M., Yao, C. and Ye, R. D. (2023) 'The Concise Guide to PHARMACOLOGY 2023/24: G protein-coupled receptors', *Br J Pharmacol,* 180 Suppl 2, pp. S23-S144.

Andradas, C., Blasco-Benito, S., Castillo-Lluva, S., Dillenburg-Pilla, P., Diez-Alarcia, R., Juanes-García, A., García-Taboada, E., Hernando-Llorente, R., Soriano, J., Hamann, S., Wenners, A., Alkatout, I., Klapper, W., Rocken, C., Bauer, M., Arnold, N., Quintanilla, M., Megías, D., Vicente-Manzanares, M., Urigüen, L., Gutkind, J. S., Guzmán, M., Pérez-Gómez, E. and Sánchez, C. (2016) 'Activation of the orphan receptor GPR55 by lysophosphatidylinositol promotes metastasis in triple-negative breast cancer', *Oncotarget,* 7(30), pp. 47565-47575.

Aragay, A. M., Katz, A. and Simon, M. I. (1992) 'The G alpha q and G alpha 11 proteins couple the thyrotropin-releasing hormone receptor to phospholipase C in GH3 rat pituitary cells', *Journal of Biological Chemistry,* 267(35), pp. 24983-24988.

Armstrong, J. F., Faccenda, E., Harding, S. D., Pawson, A. J., Southan, C., Sharman, J. L., Campo, B., Cavanagh, D. R., Alexander, S. P. H., Davenport, A. P., Spedding, M. and Davies, J. A. (2019) 'The IUPHAR/BPS Guide to PHARMACOLOGY in 2020: extending immunopharmacology content and introducing the IUPHAR/MMV Guide to MALARIA PHARMACOLOGY', *Nucleic Acids Research,* 48(D1).

Baek, M., DiMaio, F., Anishchenko, I., Dauparas, J., Ovchinnikov, S., Lee, G. R., Wang, J., Cong, Q., Kinch, L. N., Schaeffer, R. D., Millán, C., Park, H., Adams, C., Glassman, C. R., DeGiovanni, A., Pereira, J. H., Rodrigues, A. V., van Dijk, A. A., Ebrecht, A. C., Opperman, D. J., Sagmeister, T., Buhlheller, C., Pavkov-Keller, T., Rathinaswamy, M. K., Dalwadi, U., Yip, C. K., Burke, J. E., Garcia, K. C., Grishin, N. V., Adams, P. D., Read, R. J. and Baker, D. (2021) 'Accurate prediction of protein structures and interactions using a three-track neural network', *Science,* 373(6557), pp. 871-876.

Baker, D., Pryce, G., Davies, W. L. and Hiley, C. R. (2006) 'In silico patent searching reveals a new cannabinoid receptor', *Trends in Pharmacological Sciences,* 27(1), pp. 1-4.

Balenga, N. A. B., Henstridge, C. M., Kargl, J. and Waldhoer, M. (2011) 'Pharmacology, Signaling and Physiological Relevance of the G Protein-coupled Receptor 55', *Advances in pharmacology,* (62), pp. 251-277.

Benchling (2024) 'Cloud-Based Informatics Platform for Life Sciences R&D', *Benchling*.

Benovic, J., DeBlasi, A., Stone, W., Caron, M. and Lefkowitz, R. (1989) 'Beta-adrenergic receptor kinase: primary structure delineates a multigene family', *Science,* 246(4927), pp. 235-240.

Bhattacharya, S., Lam, A. R., Li, H., Balaraman, G., Niesen, M. J. M. and Vaidehi, N. (2013) 'Critical analysis of the successes and failures of homology models of G protein-coupled receptors', *Proteins: Structure, Function, and Bioinformatics,* 81(5), pp. 729-739.

Biringer, R. G. (2021) 'Endocannabinoid signaling pathways: beyond CB1R and CB2R', *J Cell Commun Signal,* 15(3), pp. 335-360.

Bjarnadóttir, T. K., Gloriam, D. E., Hellstrand, S. H., Kristiansson, H., Fredriksson, R. and Schiöth, H. B. (2006) 'Comprehensive repertoire and phylogenetic analysis of the G protein-coupled receptors in human and mouse', *Genomics,* 88(3), pp. 263-273.

Blakeley, D., Sykes, D. A., Ensor, P., Bertran, E., Aston, P. J. and Charlton, S. J. (2015) 'Simulating the influence of plasma protein on measured receptor affinity in biochemical assays reveals the utility of Schild analysis for estimating compound affinity for plasma proteins', *Br J Pharmacol,* 172(21), pp. 5037-49.

Bondar, A. and Lazar, J. (2020) 'Optical sensors of heterotrimeric G protein signaling', *FEBS Journal,* 288(8), pp. 2570-2584.

Carpenter, B., Nehmé, R., Warne, T., Leslie, A. G. W. and Tate, C. G. (2016) 'Structure of the adenosine A2A receptor bound to an engineered G protein', *Nature,* 536(7614), pp. 104-107.

Carpenter, B. and Tate, C. G. (2016) 'Engineering a minimal G protein to facilitate crystallisation of G protein-coupled receptors in their active conformation', *Protein Engineering, Design and Selection,* 29(12), pp. 583-594.

Cebi, E., Lee, J., Subramani, V. K., Bak, N., Oh, C. and Kim, K. K. (2024) 'Cryo-electron microscopy-based drug design', *Frontiers in Molecular Biosciences,* Volume 11 - 2024.

Celorrio, M., Rojo-Bustamante, E., Fernández-Suárez, D., Sáez, E., Estella-Hermoso de Mendoza, A., Müller, C. E., Ramírez, M. J., Oyarzábal, J., Franco, R. and Aymerich, M. S. (2017) 'GPR55: A therapeutic target for Parkinson's disease?', *Neuropharmacology,* 125, pp. 319-332.

Chang, H., Li, X., Shen, L., Ge, X., Hao, S., Wu, L., Liu, S., Liu, J., Vadim, C. and Hua, T. (2024) 'Structure basis of ligand recognition and activation of GPR55', *Cell Research,* 35.

Chen, Z., Ren, X., Zhou, Y. and Huang, N. (2024) 'Exploring structure-based drug discovery of GPCRs beyond the orthosteric binding site', *hLife,* 2(5), pp. 211-226.

Claff, T., Ebenhoch, R., Kley, J. T., Aniket, M., Nar, H. and Weichert, D. (2025) 'Structural basis for lipid-mediated activation of G protein-coupled receptor GPR55', *Nature Communications,* 16(1).

Costa-Neto, C. M., Parreiras-e-Silva, L. T. and Bouvier, M. (2016) 'A Pluridimensional View of Biased Agonism', *Molecular Pharmacology,* 90(5), pp. 587-595.

Costanzi, S. (2011) 'Homology Modeling of Class A G Protein-Coupled Receptors', *Methods in molecular biology,* (857), pp. 259-279.

Davis, M. W. and Jorgensen, E. M. (2022) 'ApE, A Plasmid Editor: A Freely Available DNA Manipulation and Visualization Program', *Frontiers in Bioinformatics,* 2.

Dessauer, C. W., Chen-Goodspeed, M. and Chen, J. (2002) 'Mechanism of Gαi-mediated Inhibition of Type V Adenylyl Cyclase', *Journal of Biological Chemistry,* 277(32), pp. 28823-28829.

Draper-Joyce, C. J., Verma, R. K., Michino, M., Shonberg, J., Kopinathan, A., Klein Herenbrink, C., Scammells, P. J., Capuano, B., Abramyan, A. M., Thal, D. M., Javitch, J. A., Christopoulos, A., Shi, L. and Lane, J. R. (2018) 'The action of a negative allosteric modulator at the dopamine D2 receptor is dependent upon sodium ions', *Scientific Reports,* 8(1).

Drotár, P., Jamasb, A. R., Day, B., Cangea, C. and Liò, P. (2021) 'Structure-aware generation of drug-like molecules', *arXiv (Cornell University)*.

Eberhardt, J., Santos-Martins, D., Tillack, A. F. and Forli, S. (2021) 'AutoDock Vina 1.2.0: New Docking Methods, Expanded Force Field, and Python Bindings', *Journal of Chemical Information and Modeling,* 61(8), pp. 3891-3898.

Eichel, K., Jullié, D. and von Zastrow, M. (2016) 'β-Arrestin drives MAP kinase signalling from clathrin-coated structures after GPCR dissociation', *Nature Cell Biology,* 18(3), pp. 303-310.

Fan, H. and Mark, A. E. (2004) 'Refinement of homology-based protein structures by molecular dynamics simulation techniques', *Protein Science,* 13(1), pp. 211-220.

Ferro, R., Adamska, A., Lattanzio, R., Mavrommati, I., Edling, C. E., Arifin, S. A., Fyffe, C. A., Sala, G., Sacchetto, L., Chiorino, G., De Laurenzi, V., Piantelli, M., Sansom, O. J., Maffucci, T. and Falasca, M. (2018) 'GPR55 signalling promotes proliferation of pancreatic cancer cells and tumour growth in mice, and its inhibition increases effects of gemcitabine', *Oncogene,* 37(49), pp. 6368-6382.

Fredriksson, R., Lagerström, M. C., Lundin, L.-G. and Schiöth, H. B. (2003) 'The G-Protein-Coupled Receptors in the Human Genome Form Five Main Families. Phylogenetic Analysis, Paralogon Groups, and Fingerprints', *Molecular Pharmacology,* 63(6), pp. 1256-1272.

Gangadharan, V., Selvaraj, D., Kurejova, M., Njoo, C., Gritsch, S., Škoricová, D., Horstmann, H., Offermanns, S., Brown, A. J., Kuner, T., Tappe-Theodor, A. and Kuner, R. (2013) 'A novel biological role for the phospholipid lysophosphatidylinositol in nociceptive sensitization via activation of diverse G-protein signalling pathways in sensory nerves in vivo', *Pain,* 154(12), pp. 2801-2812.

Guillamat-Prats, R., Hering, D., Derle, A., Rami, M., Härdtner, C., Santovito, D., Rinne, P., Bindila, L., Hristov, M., Pagano, S., Vuilleumier, N., Schmid, S., Janjic, A., Enard, W., Weber, C., Maegdefessel, L., Faussner, A., Hilgendorf, I. and Steffens, S. (2022) 'GPR55 in B cells limits atherosclerosis development and regulates plasma cell maturation', *Nature Cardiovascular Research,* 1(11), pp. 1056-1071.

Gurevich, E. V., Tesmer, J. J. G., Mushegian, A. and Gurevich, V. V. (2012) 'G protein-coupled receptor kinases: More than just kinases and not only for GPCRs', *Pharmacology & Therapeutics,* 133(1), pp. 40-69.

Harwood, C. R., Sykes, D. A., Redfern-Nichols, T., Underwood, O., Nicholson, C., Khoshgrudi, A. N., Koers, E. J., Ladds, G., Briddon, S. J. and Veprintsev, D. B. (2025) 'Agonist efficacy at the β(2)AR is driven by the faster association rate of the G(s) protein', *Front Pharmacol,* 16, pp. 1367991.

Hasenoehrl, C., Feuersinger, D., Sturm, E. M., Bärnthaler, T., Heitzer, E., Graf, R., Grill, M., Pichler, M., Beck, S., Butcher, L., Thomas, D., Ferreirós, N., Schuligoi, R., Schweiger, C., Haybaeck, J. and Schicho, R. (2017) 'G protein-coupled receptor GPR55 promotes colorectal cancer and has opposing effects to cannabinoid receptor 1', *International Journal of Cancer,* 142(1), pp. 121-132.

Hauser, A. S., Attwood, M. M., Rask-Andersen, M., Schiöth, H. B. and Gloriam, D. E. (2017) 'Trends in GPCR drug discovery: new agents, targets and indications', *Nature reviews. Drug discovery,* 16(12), pp. 829-842.

He, X. H., You, C. Z., Jiang, H. L., Jiang, Y., Xu, H. E. and Cheng, X. (2023) 'AlphaFold2 versus experimental structures: evaluation on G protein-coupled receptors', *Acta Pharmacol Sin,* 44(1), pp. 1-7.

Heller, S., McNaught, A., Stein, S., Tchekhovskoi, D. and Pletnev, I. (2013) 'InChI - the worldwide chemical structure identifier standard', *Journal of Cheminformatics,* 5(1).

Henstridge, C. M., Balenga, N. A. B., Ford, L. A., Ross, R. A., Waldhoer, M. and Irving, A. J. (2009) 'The GPR55 ligand L-α-lysophosphatidylinositol promotes RhoA-dependent Ca2+ signaling and NFAT activation', *The FASEB Journal,* 23(1), pp. 183-193.

Henstridge, C. M., Balenga, N. A. B., Schröder, R., Kargl, J. K., Platzer, W., Martini, L., Arthur, S., Penman, J., Whistler, J. L., Kostenis, E., Waldhoer, M. and Irving, A. J. (2010) 'GPR55 ligands promote receptor coupling to multiple signalling pathways', *British Journal of Pharmacology,* 160(3), pp. 604-614.

Heo, L. and Feig, M. (2022) 'Multi-state modeling of G-protein coupled receptors at experimental accuracy', *Proteins,* 90(11), pp. 1873-1885.

Hewer, R. C., Christie, L. A., Doyle, K. J., Xu, X., Roberts, M. J., Dickson, L., Cheung, T., Cadwalladr, D. H., Pickford, P., Teall, M., Sheardown, S., Narayana, L., Brice, N. L., Dawson, L. A., Carlton, M. and Bürli, R. W. (2023) 'Discovery and Characterization of Novel CNS-Penetrant GPR55 Agonists', *Journal of Medicinal Chemistry,* 66(18), pp. 12858-12876.

Hilger, D., Masureel, M. and Kobilka, B. K. (2018) 'Structure and dynamics of GPCR signaling complexes', *Nature Structural & Molecular Biology,* 25(1), pp. 4-12.

Hill, J. D., Zuluaga-Ramirez, V., Gajghate, S., Winfield, M. and Persidsky, Y. (2018) 'Activation of GPR55 increases neural stem cell proliferation and promotes early adult hippocampal neurogenesis', *Br J Pharmacol,* 175(16), pp. 3407-3421.

Hu, G.-M., Mai, T.-L. and Chen, C.-M. (2017) 'Visualizing the GPCR Network: Classification and Evolution', *Scientific Reports,* 7(1), pp. 15495.

Irwin, J. J. and Shoichet, B. K. (2005) 'ZINC – A Free Database of Commercially Available Compounds for Virtual Screening', *Journal of chemical information and modeling,* 45(1), pp. 177-182.

Isert, C., Atz, K. and Schneider, G. (2023) 'Structure-based drug design with geometric deep learning', *Current Opinion in Structural Biology,* 79, pp. 102548.

Jean-Charles, P. Y., Kaur, S. and Shenoy, S. K. (2017) 'G Protein-Coupled Receptor Signaling Through β-Arrestin-Dependent Mechanisms', *J Cardiovasc Pharmacol,* 70(3), pp. 142-158.

Jiménez-Rosés, M., Morgan, B. A., Jimenez Sigstad, M., Tran, T. D. Z., Srivastava, R., Bunsuz, A., Borrega-Román, L., Hompluem, P., Cullum, S. A., Harwood, C. R., Koers, E. J., Sykes, D. A., Styles, I. B. and Veprintsev, D. B. (2022) 'Combined docking and machine learning identify key molecular determinants of ligand pharmacological activity on β2 adrenoceptor', *Pharmacology Research & Perspectives,* 10(5), pp. e00994.

Johns, D. G., Behm, D. J., Walker, D. J., Ao, Z., Shapland, E. M., Daniels, D. A., Riddick, M., Dowell, S., Staton, P. C., Green, P., Shabon, U., Bao, W., Aiyar, N., Yue, T. L., Brown, A. J., Morrison, A. D. and Douglas, S. A. (2007) 'The novel endocannabinoid receptor GPR55 is activated by atypical cannabinoids but does not mediate their vasodilator effects', *British Journal of Pharmacology,* 152(5), pp. 825-831.

Jubb, H. C., Higueruelo, A. P., Ochoa-Montaño, B., Pitt, W. R., Ascher, D. B. and Blundell, T. L. (2017) 'Arpeggio: A Web Server for Calculating and Visualising Interatomic Interactions in Protein Structures', *Journal of Molecular Biology,* 429(3), pp. 365-371.

Jumper, J., Evans, R., Pritzel, A., Green, T., Figurnov, M., Ronneberger, O., Tunyasuvunakool, K., Bates, R., Žídek, A., Potapenko, A., Bridgland, A., Meyer, C., Kohl, S. A. A., Ballard, A. J., Cowie, A., Romera-Paredes, B., Nikolov, S., Jain, R., Adler, J., Back, T., Petersen, S., Reiman, D., Clancy, E., Zielinski, M., Steinegger, M., Pacholska, M., Berghammer, T., Bodenstein, S., Silver, D., Vinyals, O., Senior, A. W., Kavukcuoglu, K., Kohli, P. and Hassabis, D. (2021) 'Highly Accurate Protein Structure Prediction with Alphafold', *Nature,* 596(7873), pp. 583-589.

Kamato, D., Thach, L., Bernard, R., Chan, V., Zheng, W., Kaur, H., Brimble, M., Osman, N. and Little, P. J. (2015) 'Structure, Function, Pharmacology, and Therapeutic Potential of the G Protein, GÎ±/q,11', *Frontiers in Cardiovascular Medicine,* 2(14).

Kapur, A., Zhao, P., Sharir, H., Bai, Y., Caron, M. G., Barak, L. S. and Abood, M. E. (2009) 'Atypical Responsiveness of the Orphan Receptor GPR55 to Cannabinoid Ligands', *Journal of Biological Chemistry,* 284(43), pp. 29817-29827.

Kargl, J., Andersen, L., Hasenöhrl, C., Feuersinger, D., Stančić, A., Fauland, A., Magnes, C., Amin, E. H., Lax, S., Uranitsch, S., Johannes, H., Heinemann, Á. and Schicho, R. (2015) 'GPR55 promotes migration and adhesion of colon cancer cells indicating a role in metastasis', *British Journal of Pharmacology,* 173(1), pp. 142-154.

Kenakin, T. and Christopoulos, A. (2013) 'Signalling bias in new drug discovery: detection, quantification and therapeutic impact', *Nature Reviews Drug Discovery,* 12(3), pp. 205-216.

Kotsikorou, E., Madrigal, K. E., Hurst, D. P., Sharir, H., Lynch, D. L., Heynen-Genel, S., Milan, L. B., Chung, T. D. Y., Seltzman, H. H., Bai, Y., Caron, M. G., Barak, L., Abood, M. E. and Reggio, P. H. (2011) 'Identification of the GPR55 Agonist Binding Site Using a Novel Set of High-Potency GPR55 Selective Ligands', *Biochemistry,* 50(25), pp. 5633-5647.

L. Mohan, M., T. Vasudevan, N., K. Gupta, M., E. Martelli, E. and V. Naga Prasad, S. (2012) 'G-Protein Coupled Receptor Resensitization - Appreciating the Balancing Act of Receptor Function', *Current Molecular Pharmacology,* 5(3), pp. 350-361.

Lan, T.-H., Liu, Q., Li, C., Wu, G. and Lambert, N. A. (2012) 'Sensitive and High Resolution Localization and Tracking of Membrane Proteins in Live Cells with BRET', *Traffic,* 13(11), pp. 1450-1456.

Lauckner, J. E., Jensen, J. B., Chen, H. Y., Lu, H. C., Hille, B. and Mackie, K. (2008) 'GPR55 is a cannabinoid receptor that increases intracellular calcium and inhibits M current', *Proceedings of the National Academy of Sciences,* 105(7), pp. 2699-2704.

Libert, F., Schiffmann, S. N., Lefort, A., Parmentier, M., Gérard, C., Dumont, J. E., Vanderhaeghen, J. J. and Vassart, G. (1991) 'The orphan receptor cDNA RDC7 encodes an A1 adenosine receptor', *The EMBO Journal,* 10(7), pp. 1677-1682.

Liu, B., Song, S., Jones, P. M. and Persaud, S. J. (2015) 'GPR55: From orphan to metabolic regulator?', *Pharmacology & Therapeutics,* 145, pp. 35-42.

Liudmila Ostroumova, P., Gleb, G., Aleksandr, V., Anna Veronika, D. and Andrey, G. (2017) 'CatBoost: unbiased boosting with categorical features', *arXiv (Cornell University)*.

Lounnas, V., Ritschel, T., Kelder, J., McGuire, R., Bywater, R. P. and Foloppe, N. (2013) 'Current progress in Structure-Based Rational Drug Design marks a new mindset in drug discovery', *Comput Struct Biotechnol J,* 5, pp. e201302011.

Lundberg, S. and Lee, S.-I. (2017) 'A Unified Approach to Interpreting Model Predictions', *arXiv.org*.

Mach, L., Omran, A., Bouma, J., Radetzki, S., Sykes, D. A., Guba, W., Li, X., Höffelmeyer, C., Hentsch, A., Gazzi, T., Mostinski, Y., Wasinska-Kalwa, M., de Molnier, F., van der Horst, C., von Kries, J. P., Vendrell, M., Hua, T., Veprintsev, D. B., Heitman, L. H., Grether, U. and Nazare, M. (2024) 'Highly Selective Drug-Derived Fluorescent Probes for the Cannabinoid Receptor Type 1 (CB(1)R)', *J Med Chem,* 67(14), pp. 11841-11867.

Matthews, B. W. (1975) 'Comparison of the predicted and observed secondary structure of T4 phage lysozyme', *Biochimica et Biophysica Acta (BBA) - Protein Structure,* 405(2), pp. 442-451.

Mendez, D., Gaulton, A., Bento, A. P., Chambers, J., De Veij, M., Félix, E., Magariños, María P., Mosquera, Juan F., Mutowo, P., Nowotka, M., Gordillo-Marañón, M., Hunter, F., Junco, L., Mugumbate, G., Rodriguez-Lopez, M., Atkinson, F., Bosc, N., Radoux, Chris J., Segura-Cabrera, A., Hersey, A. and Leach, Andrew R. (2018) 'ChEMBL: towards direct deposition of bioassay data', *Nucleic Acids Research,* 47(D1), pp. D930-D940.

Merkel, D. (2014) 'Docker: lightweight Linux containers for consistent development and deployment', *Linux Journal,* 2014(239), pp. 2.

Mohammad Nezhady, M. A., Rivera, J. C. and Chemtob, S. (2020) 'Location Bias as Emerging Paradigm in GPCR Biology and Drug Discovery', *iScience,* 23(10), pp. 101643.

Moreno-Navarrete, J. M., Catalán, V., Whyte, L., Díaz-Arteaga, A., Vázquez-Martínez, R., Rotellar, F., Guzmán, R., Gómez-Ambrosi, J., Pulido, M. R., Russell, W. R., Imbernón, M., Ross, R. A., Malagón, M. M., Dieguez, C., Fernández-Real, J. M., Frühbeck, G. and Nogueiras, R. (2012) 'The <scp>l</scp>-α-Lysophosphatidylinositol/GPR55 System and Its Potential Role in Human Obesity', *Diabetes,* 61(2), pp. 281-291.

Mystek, P., Tworzydło, M., Dziedzicka-Wasylewska, M. and Polit, A. (2015) 'New insights into the model of dopamine D1 receptor and G-proteins interactions', *Biochimica et Biophysica Acta (BBA) - Molecular Cell Research,* 1853(3), pp. 594-603.

Nehmé, R., Carpenter, B., Singhal, A., Strege, A., Edwards, P. C., White, C. F., Du, H., Grisshammer, R. and Tate, C. G. (2017) 'Mini-G proteins: Novel tools for studying GPCRs in their active conformation', *PLOS ONE,* 12(4), pp. e0175642-e0175642.

O'Boyle, N. M., Banck, M., James, C. A., Morley, C., Vandermeersch, T. and Hutchison, G. R. (2011) 'Open Babel: An open chemical toolbox', *Journal of Cheminformatics,* 3(1).

Oka, S., Nakajima, K., Yamashita, A., Kishimoto, S. and Sugiura, T. (2007) 'Identification of GPR55 as a lysophosphatidylinositol receptor', *Biochemical and Biophysical Research Communications,* 362(4), pp. 928-934.

Okuno, T. and Yokomizo, T. (2011) 'What is the natural ligand of GPR55?', *J Biochem,* 149(5), pp. 495-7.

Onaivi, E. S. (2008) *Marijuana and Cannabinoid Research.* Springer Science & Business Media.

Pándy-Szekeres, G., Munk, C., Tsonkov, T. M., Mordalski, S., Harpsøe, K., Hauser, A. S., Bojarski, A. J. and Gloriam, D. E. (2017) 'GPCRdb in 2018: adding GPCR structure models and ligands', *Nucleic Acids Research,* 46(D1), pp. D440-D446.

Pérez-Gómez, E., Andradas, C., Flores, J. M., Quintanilla, M., Paramio, J. M., Guzmán, M. and Sánchez, C. (2013) 'The orphan receptor GPR55 drives skin carcinogenesis and is upregulated in human squamous cell carcinomas', *Oncogene,* 32(20), pp. 2534-2542.

Pettersen, E. F., Goddard, T. D., Huang, C. C., Couch, G. S., Greenblatt, D. M., Meng, E. C. and Ferrin, T. E. (2004) 'UCSF Chimera--a visualization system for exploratory research and analysis', *Journal of Computational Chemistry,* 25(13), pp. 1605-1612.

Rasheed, S. A. K., Subramanyan, L. V., Lim, W. K., Udayappan, U. K., Wang, M. and Casey, P. J. (2021) 'The emerging roles of Gα12/13 proteins on the hallmarks of cancer in solid tumors', *Oncogene,* 41, pp. 1-12.

Ravindranath, P. A., Forli, S., Goodsell, D. S., Olson, A. J. and Sanner, M. F. (2015) 'AutoDockFR: Advances in Protein-Ligand Docking with Explicitly Specified Binding Site Flexibility', *PLOS Computational Biology,* 11(12), pp. e1004586.

Ross, R. A. (2009) 'The enigmatic pharmacology of GPR55', *Trends in Pharmacological Sciences,* 30(3), pp. 156-163.

Ross, R. A. (2011) 'L-α-Lysophosphatidylinositol meets GPR55: a deadly relationship', *Trends in Pharmacological Sciences,* 32(5), pp. 265-269.

Ryberg, E., Larsson, N., Sjögren, S., Hjorth, S., Hermansson, N.-O., Leonova, J., Elebring, T., Nilsson, K., Drmota, T. and Greasley, P. J. (2007) 'The orphan receptor GPR55 is a novel cannabinoid receptor', *British Journal of Pharmacology,* 152(7), pp. 1092-1101.

Ryberg, E., Larsson, N., Sjögren, S., Hjorth, S., Hermansson, N. O., Leonova, J., Elebring, T., Nilsson, K., Drmota, T. and Greasley, P. J. (2009) 'The orphan receptor GPR55 is a novel cannabinoid receptor', *British Journal of Pharmacology,* 152(7), pp. 1092-1101.

Sawzdargo, M., Nguyen, T., Lee, D. K., Lynch, K. R., Cheng, R., Heng, H. H. Q., George, S. R. and O'Dowd, B. F. (1999) 'Identification and cloning of three novel human G protein-coupled receptor genes GPR52, ΨGPR53 and GPR55: GPR55 is extensively expressed in human brain', *Molecular Brain Research,* 64(2), pp. 193-198.

Schihada, H., Klompstra, T. M., Humphrys, L. J., Cervenka, I., Dadvar, S., Kolb, P., Ruas, J. L. and Schulte, G. (2022) 'Isoforms of GPR35 have distinct extracellular N-termini that

allosterically modify receptor-transducer coupling and mediate intracellular pathway bias', *Journal of biological chemistry/□The □Journal of biological chemistry,* 298(9), pp. 102328-102328.

Schihada, H., Shekhani, R. and Schulte, G. (2021) 'Quantitative assessment of constitutive G protein–coupled receptor activity with BRET-based G protein biosensors', *Science Signaling,* 14(699).

Scott-Dennis, M., Rafani, F. A., Yi, Y., Perera, T., Harwood, C. R., Guba, W., Rufer, A. C., Grether, U., Veprintsev, D. B. and Sykes, D. A. (2023) 'Development of a membrane-based Gi-CASE biosensor assay for profiling compounds at cannabinoid receptors', *Frontiers in Pharmacology,* 14.

Sengmany, K., Hellyer, S. D., Albold, S., Wang, T., Conn, P. J., May, L. T., Christopoulos, A., Leach, K. and Gregory, K. J. (2019) 'Kinetic and system bias as drivers of metabotropic glutamate receptor 5 allosteric modulator pharmacology', *Neuropharmacology,* 149, pp. 83-96.

Sharir, H. and Abood, M. E. (2010) 'Pharmacological characterization of GPR55, a putative cannabinoid receptor', *Pharmacology & Therapeutics,* 126(3), pp. 301-313.

Shenoy, S. K. and Lefkowitz, R. J. (2003) 'Trafficking Patterns of β-Arrestin and G Protein-coupled Receptors Determined by the Kinetics of β-Arrestin Deubiquitination*', *Journal of Biological Chemistry,* 278(16), pp. 14498-14506.

Shore, D. M. and Reggio, P. H. (2015) 'The therapeutic potential of orphan GPCRs, GPR35 and GPR55', *Frontiers in Pharmacology,* Volume 6 - 2015.

Simons, K. T., Bonneau, R., Ruczinski, I. and Baker, D. (1999) 'Ab initio protein structure prediction of CASP III targets using ROSETTA', *Proteins: Structure, Function, and Genetics,* 37(S3), pp. 171-176.

Sliwoski, G., Kothiwale, S., Meiler, J. and Lowe, E. W. (2013) 'Computational Methods in Drug Discovery', *Pharmacological Reviews,* 66(1), pp. 334-395.

Song, Y., DiMaio, F., Wang, Ray Y.-R., Kim, D., Miles, C., Brunette, T. J., Thompson, J. and Baker, D. (2013) 'High-Resolution Comparative Modeling with RosettaCM', *Structure,* 21(10), pp. 1735-1742.

Sun, D., Ostermaier, M. K., Heydenreich, F. M., Mayer, D., Jaussi, R., Joerg, S. and Veprintsev, D. B. (2013) 'AAscan, PCRdesign and MutantChecker: A Suite of Programs for Primer Design and Sequence Analysis for High-Throughput Scanning Mutagenesis', *PLoS ONE,* 8(10), pp. e78878-e78878.

Sykes, D. A., Bradley, M. E., Riddy, D. M., Willard, E., Reilly, J., Miah, A., Bauer, C., Watson, S. J., Sandham, D. A., Dubois, G. and Charlton, S. J. (2016) 'Fevipiprant (QAW039), a Slowly Dissociating CRTh2 Antagonist with the Potential for Improved Clinical Efficacy', *Mol Pharmacol,* 89(5), pp. 593-605.

Taussig, R., Tang, W. J., Hepler, J. R. and Gilman, A. G. (1994) 'Distinct patterns of bidirectional regulation of mammalian adenylyl cyclases', *Journal of Biological Chemistry,* 269(8), pp. 6093-6100.

Tesmer, J. J. G., Sunahara, R. K., Gilman, A. G. and Sprang, S. R. (1997) 'Crystal Structure of the Catalytic Domains of Adenylyl Cyclase in a Complex with Gsα·GTPγS', *Science,* 278(5345), pp. 1907-1916.

Trott, O. and Olson, A. J. (2010) 'AutoDock Vina: improving the speed and accuracy of docking with a new scoring function, efficient optimization, and multithreading', *J Comput Chem,* 31(2), pp. 455-61.

Wang, X.-F., Galaj, E., Bi, G.-H., Zhang, C., He, Y., Zhan, J., Bauman, M. H., Gardner, E. L. and Xi, Z.-X. (2020) 'Different receptor mechanisms underlying phytocannabinoid- versus synthetic cannabinoid-induced tetrad effects: Opposite roles of CB1/CB2 versus GPR55 receptors', *British Journal of Pharmacology,* 177(8), pp. 1865-1880.

Xia, R., Yuan, Q., Wang, N., Hou, L., Abe, J., Song, J., Ito, Y., Xu, H. E. and He, Y. (2024) 'Structural insight into GPR55 ligand recognition and G-protein coupling', *Cell Research,* 35(1), pp. 76-79.

Yang, H., Zhou, J. and Lehmann, C. (2016) 'GPR55 – a putative "type 3" cannabinoid receptor in inflammation', *Journal of Basic and Clinical Physiology and Pharmacology,* 27(3).

Yang, Y. M., Kuen, D.-S., Chung, Y., Kurose, H. and Kim, S. G. (2020) 'Gα12/13 signaling in metabolic diseases', *Experimental & Molecular Medicine,* 52(6), pp. 896-910.

Zamponi, G. W., Bourinet, E., Nelson, D., Nargeot, J. and Snutch, T. P. (1997) 'Crosstalk between G proteins and protein kinase C mediated by the calcium channel α1 subunit', *Nature,* 385(6615), pp. 442-446.

Zhang, M., Chen, T., Lu, X., Lan, X., Chen, Z. and Lu, S. (2024) 'G protein-coupled receptors (GPCRs): advances in structures, mechanisms and drug discovery', *Signal Transduction and Targeted Therapy,* 9(1), pp. 88.

Zhang, S., Coso, O. A., Collins, R., Gutkind, J. S. and Simonds, W. F. (1996) 'A C-terminal Mutant of the G Protein β Subunit Deficient in the Activation of Phospholipase C-β', *Journal of Biological Chemistry,* 271(33), pp. 20208-20212.

Zhao, X., Jones, A., Olson, K. R., Peng, K., Wehrman, T., Park, A., Mallari, R., Nebalasca, D., Young, S. W. and Xiao, S.-H. (2008) 'A Homogeneous Enzyme Fragment Complementation-Based β-Arrestin Translocation Assay for High-Throughput Screening of G-Protein-Coupled Receptors', *SLAS Discovery,* 13(8), pp. 737-747.